Perturbation Solution of Air-Water Mixture for Jet Noise Reduction.

By:

Author: Juan Felipe Uribe Cifuentes

Advisor: Reda R. Mankbadi Ph.D.
Co-Advisor: Guillermo Andrés Jaramillo Pizarro Ph.D.

A thesis submitted to the Faculty of Embry-Riddle Aeronautical University and Universidad del Valle in partial fulfillment of the requirements for the degree of

Master of Science in Aerospace Engineering

within the framework of a dual-degree agreement between the universities.





November 2025
Embry-Riddle Aeronautical University
Daytona Beach, Florida

Perturbation Solution of Air-Water Mixture for Jet Noise Reduction

By

Juan Felipe Uribe Cifuentes

A Thesis Submitted to the Faculty of Embry-Riddle Aeronautical University

In Partial Fulfillment of the Requirements for the Degree of

Master of Science in Aerospace Engineering

December, 2026

Embry-Riddle Aeronautical University

Daytona Beach, Florida

ACKNOWLEDGMENTS

To my research advisor at Embry-Riddle Aeronautical University, Dr. Reda R. Mankbadi, for trusting me with the responsibility of being one of his students and for always being attentive to my needs, not only academic but also personal. To my advisor at Universidad del Valle, Dr. Guillermo Andrés Jaramillo Pizarro, who has been a fundamental pillar in my life since the moment I met him, for all his support and motivation in every aspect of my life. To Dr. Vladimir V. Golubev, Dr. William A. Engblom, and Dr. Sam Salehian for serving as members of my thesis committee.

To my mother and her husband, Paola Andrea Cifuentes and Julián Correa Morales, whose support and understanding have been essential for reaching this stage of my life. To my friends Juan Camilo Hernández, Jefferson Duque, Vadim Voropayev, Karol Cordoba, and Marcela Florez whose help and encouragement, especially since I arrived in the United States, made it much easier to reach this point in my career.

To my grandmother, Blanca Elena Guelga, who has cared for me all my life and taught me strong values, and who remains one of the main reasons I continue to pursue my dreams in the United States. Finally, to my father, Juan Carlos Uribe, who is no longer with us, but I know that this was also his dream and that he would be very proud to see where I am today.

To all of you, my deepest thanks.

ABSTRACT

The attenuation of jet-generated noise through multiphase flows offers a promising passive mitigation strategy. Traditional jet-noise suppression studies have primarily focused on modifying jet plume structure through direct water/Air injection. In contrast, this work quantify the interaction of acoustic waves with an externally placed air–water curtain surrounding the jet, thereby assessing its ability to attenuate radiated noise without disturbing the jet itself.

Two distinct curtain configurations are analyzed: (i) a gaseous medium (air) containing liquid water droplets, and (ii) a liquid medium (water) containing air bubbles. For each configuration, two flow regimes are examined: (a) a suspended case, where both phases exhibit negligible mean velocity, and (b) a dispersed case, where the ambient velocity induces motion in the phases.

The present study extends previous studies by incorporating finite particle volume fractions and interphase velocity slip through a generalized perturbation framework derived directly from the volume-averaged multiphase equations. All cases are solved numerically, while an analytical solution is derived for the suspended particle case. Results show that attenuation increases with particulate volume fraction and that an optimal droplet-to-nozzle diameter ratio exists for maximum reduction. Comparisons with prior experimental data and Computational Fluid Dynamics simulations confirm that the perturbation approach accurately captures the frequency-dependent absorption trends. For the dispersed regime, the analysis reveals that phase slip modifies the attenuation characteristics depending on the configuration.

These findings demonstrate the potential of externally placed multiphase curtains as an effective passive method for jet-noise mitigation. The developed framework provides a foundation for optimizing curtain parameters and guides future experimental and computational studies aimed at practical implementation in aeroacoustic applications.

TABLE OF CONTENTS

ACKNOWLEDGMENTS i

ABSTRACT ii

LIST OF FIGURES ix

LIST OF TABLES x

NOMENCLATURE xi

1 Introduction 1

1.1 Origin of Noise in Aircraft 2

1.2 The Physics of Free Jet and Its Radiated Noise 4

1.3 Jet Noise Control 6

1.3.1 Passive Control 6

1.3.2 Active Control 9

1.4 Noise Reduction Using Multiphase Flows 11

1.5 Overview of the Present Study 14

1.6 Objectives 16

1.6.1 General Objectives 16

1.6.2 Specific Objectives 16

2 Methodology, Particle Case 17

2.1 The Governing Equations 17

2.2 Particle Perturbed Equations 21

2.2.1 The Perturbed Equations in Spherical Coordinates 22

2.2.2 One-Dimensional Spherical Flow Simplifications 24

2.3 Suspended Droplet Case 25

2.3.1 Analytical Asymptotic Solution 26

2.3.2 Effect of Volume of fraction 31
2.3.3 Numerical Solution of the Suspended Particle Case 32
2.3.4 Acoustic Scattering by Spherical Droplets 33
2.3.5 Application of Suspended Case to Jet Noise Reduction 38
2.3.6 Estimation Effect of Droplet Size for Noise Reduction 39
2.3.7 Estimation of Sound Level Reduction for a Jet 41
2.3.8 Dependency on the Strouhal Number 43
2.4 Comparison of Numerical Result of the Suspended Equations With Experimental Results 44
2.5 Computational Fluid Dynamics Simulations for the Suspended Case 48
2.5.1 Numerical Scheme 51
2.5.2 Spatial and Temporal Discretization 52
2.5.3 Computational Domain and Boundary Conditions 53
2.5.4 Verification for the Base Case without Particles in the Domain 54
2.5.5 Particle Cloud and Dispersed Phase Characterization 56
2.5.6 Wave Attenuation Results With Water Particles in the Domain 58
2.5.7 Reduction Factor k_i^+ from CFD Simulations 63
2.6 Dispersed Particle Case 65
2.6.1 Mean Flow Equations 65
2.6.2 Effect of Interphase Relative Motion on Acoustic Wave Attenuation 67
2.6.3 Solution of the Perturbation Equations as a Function of the Mean Flow Results 68
2.6.4 Attenuation factor k_i^+ and Normalized Noise Reduction as a Function of ξ^+ 68

3 Methodology, Bubbly Case 70
3.1 The Governing Equations 70
3.2 Bubbly Perturbed Equations 73

3.2.1 The Perturbed Equations in Spherical Coordinates 76
3.2.2 One-Dimensional Spherical Flow Simplifications 78
3.3 Suspended bubbly case 79
3.3.1 Effect of Volume of Fraction 80
3.3.2 Application of Suspended Bubbly Case to Jet Noise Reduction 81
3.3.3 Estimation of Sound Level Reduction for a Jet using Bubble Flow 82
3.3.4 Dependency on the Strouhal Number for the Suspended Bubbly Case 82
3.4 Comparison of Suspended Equations for Bubbly Flow with Experimental Results 83
3.5 Dispersed Bubbly Case 84
3.5.1 Mean Flow Equations for Bubbly Flow 85
3.5.2 Effect of Interphase Relative Motion on Acoustic Wave Attenuation for Bubbly Flow 87
3.5.3 Solution of the Perturbation Equations for Bubbly Flow as a Function of the Mean Flow Results 89

4 Conclusion and future work 92
4.1 Particle Suspended Case 92
4.2 Particle Dispersed case 93
4.3 Bubbly Suspended Case 94
4.4 Bubbly Dispersed Case 94
4.5 Future Work 95

REFERENCES 97

LIST OF FIGURES

Figure **Page**

1.1 Effective perceived noise level for military and commercial aircraft, 1000 ft (305 m) flyover operation [1]. 2

1.2 Noise-sources breakdown in a conventional airplane [1]. 3

1.3 Typical modern aircraft noise levels [2]. 3

1.4 Evolution of a Kelvin–Helmholtz instability wave into a nonlinear wave then to large turbulence structures and fine-scale turbulence [3]. 5

1.5 Two self-similar regions in a high-speed jet. [4] 5

1.6 Water injection hardware with 6 injectors positioned for injection at nozzle exit [5]. 8

1.7 Instantaneous contours of dilatation, vorticity, and phase fraction [6]. 9

1.8 Schematic showing the use of a water–air curtain to reduce supersonic jet noise. Adapted from the U.S. Navy public-domain image (Defense Media Activity Center, photo by PH3 D. Dostie, ID DN-ST-84-11502) via NavSource Online: Aircraft Carrier Photo Archive (https://www.navsource.net/archives/02/0270ai.jpg). 15

2.1 Air-water mixture surrounding the jet. 17

2.2 Spherical approximation to the flow outside of the jet. 22

2.3 Effect of the dimensionless frequency Ω on the reduction factor, k_i^+ for various water volume of fraction δ. 32

2.4 Comparison of asymptotic and numerical solutions for the reduction factor k_i^+ for various δ. 34

2.5 Schematic representation of acoustic scattering by a spherical particle. Here, P_i and ω represents the amplitude and the angular frequency of the incident wave, respectively. 35

2.6 Schematic representation of acoustic intensity attenuation in a suspension of scattering particles. 36
2.7 Reduction factor k_i^+ from particle scattering as a function of non dimensional frequency Ω for various droplet volume fractions ϕ_p. here $d_p = 5 \cdot 10^{-4}$m. 39
2.8 Schematic representation of the background jet flow field into a quiescent ambient fluid. 40
2.9 Effect of the droplet size on the reduction factor, St=0.5, $R_j = 10^5$. 41
2.10 Estimated Decibels Reduction for a Jet with Mach number M_j =1, Reynolds number $R_j = 10^5$ with peak noise at St=0.5. 43
2.11 Dependency of the noise reduction on the Strouhal number for various water volume of fraction. 44
2.12 Comparison of Asymptotic, Numerical, and Experimental Attenuation Results. Here $\alpha = \frac{k_i^+}{\delta}\eta$. 45
2.13 Experimental measurements of normalized noise reduction as a function of frequency for different mass fractions. Adapted from Mahanta and Vajpayee [7]. 46
2.14 Numerical predictions of normalized noise reduction as a function of Strouhal number for equivalent particle volume fractions. $d_p = 3 \times 10^{-4}$ m. 47
2.15 Close-up view of the structured computational mesh near the inlet boundary. 54
2.16 comparison between the analytical pressure variation and the CFD results. (a) At inlet boundary, (b) At 1 meter from the inlet boundary, and (c) Close-up view at 1 meter from the inlet boundary. 55
2.17 Sketch of distribution of the phases in the domain. Here, it is assumed D_j=1 m. 57
2.18 Cloud parcels for $d_p = 5 \cdot 10^{-4}$. 58
2.19 Volume of fraction in the compatuational domain. a) $\phi_p = 0.001$, and b) $\phi_p = 0.005$. 58

2.20 Pressure perturbation amplitude for the case with $\phi_p = 0.001$, $d_p = 2.5 \times 10^{-5}$ m, and $f = 500Hz$ comparing the single-phase air and mixture cases. 61

2.21 Pressure perturbation amplitude for the case with $\phi_p = 0.001$,$d_p = 4\times10^{-5}$ m, and $f = 500Hz$ comparing the single-phase air and mixture cases. 61

2.22 Pressure perturbation amplitude for the case with $\phi_p = 0.001$, $d_p = 7\times10^{-5}$ m, and $f = 500Hz$ comparing the single-phase air and mixture cases. 62

2.23 Pressure perturbation amplitude for the case with $\phi_p = 0.005$, $d_p = 4\times10^{-5}$ m, and $f = 500Hz$ comparing the single-phase air and mixture cases. 62

2.24 Pressure perturbation amplitude for the case with $\phi_p = 0.005$, $d_p = 7\times10^{-5}$ m, and $f = 500Hz$ comparing the single-phase air and mixture cases. 63

2.25 Pressure perturbation amplitude for the case with $\phi_p = 0.005$, $d_p = 1.5 \times 10^{-4}$ m, and $f = 500Hz$ comparing the single-phase air and mixture cases. 63

2.26 Reduction factor k_i^+ as a function of the dimensionless frequncy Ω comparing numerical results obtained from the perturbation approach and CFD for different volume of fraction ratios δ. 64

2.27 Reduction factor k_i^+ as a function of the particle diameter d_p comparing numerical results obtained from the perturbation approach and CFD for different volume of fraction ratios δ. 64

2.28 Numerical solution of the mean flow equations: (a) Mean flow velocities and (b) Mean volume fraction. 66

2.29 Effect of Ω on k_i^+ with phase motion. a)with phase slip and b)without phase slip. 67

2.30 Dependency of the noise reduction on the Strouhal number with relative motion between the phases. 68

2.31 Effect of droplet diameter on the normalized noise reduction DB/ξ^+. a) Suspended case. b) Dispersed case. 69

2.32 Normalized noise reduction dB/ξ^+ as functions of the normalized radial coordinate ξ^+. 69

3.1 Air-water mixture surrounding the jet.. 70

3.2 Spherical approximation to the flow outside of the jet for bubbly flow. 76

3.3 Reduction factor k_i^+ as a function of the dimensionless frequency for various gas volume of fraction ϕ_g. Here $d_b = 0.001m$. 81

3.4 Normalized noise reduction as a function of the gas volume of fraction ϕ_g, where M_j =1, Reynolds number $R_j = 10^5$, and St=0.5 for the suspended bubbly case. 83

3.5 Dependency of the noise reduction on the Strouhal number for various ϕ_g, where M_j =1, Reynolds number $R_j = 10^5$, and $d_p = 0.038$m. 84

3.6 Comparison for the attenuation per centimeter between the numerical results and Silberman's Figure 5. Here, ϕ_g =0.01, d_b=0.528 cm. 85

3.7 Numerical solution of the mean flow system: (a) Mean flow velocities and (b) Mean volume fraction. 87

3.8 Effect of Ω on k_i^+ with phase motion for bubbly flow. a)with phase slip and b)without phase slip. Here, $d_b = 0.005m$. 88

3.9 Dependency of the noise reduction on the Strouhal number with relative motion between the phases. 89

3.10 Effect of droplet diameter on the normalized noise reduction. DB/ξ^+ as a function of the mean floe solution. a) complete domain b) Close-up view of the region near the boundary. 90

LIST OF TABLES

Table **Page**

2.1 Summary of dispersed phase relaxation parameters selected. 56

2.2 Summary of cloud parameters. 57

NOMENCLATURE

$\rho_g,\ \rho_p, \rho_f$	Densities of gas, particle, and liquid phases
Φ_g, Φ_p, Φ_f	Volume fractions of gas, particle, and liquid phases
$\mathbf{u}_g,\ \mathbf{u}_p, \mathbf{u}_f$	Velocity vectors of gas, particle, and liquid phases
$p_g,\ p_p, p_f$	Pressures of gas, particle, and liquid phases
$E_g,\ E_p$	Total specific energies of gas and particle phases
$H_g,\ H_p$	Specific enthalpies of gas and particle phases
C_{pg}, C_{pp}, C_{pf}	Gas, Particle, and liquid specific heat at constant pressure
C_{vg}	Gas specific heat at constant volume
$\mathbf{F}_{QS},\ \mathbf{F}_{AM}$	Quasi–steady and added–mass interphase forces
Q_{gp}	Interphase heat transfer
$f_{QS},\ f_{AM}$	Specific quasi–steady and added–mass forces
q_{gp}	Specific interphase heat transfer
$\Psi(\mathrm{Re})$	Drag correction factor
Re	Relative Reynolds number
Nu	Nusselt number
Pr	Prandtl number
d_p, d_b	Particle and bubble diameter
ν_g, ν_f	Gas and liquid kinematic viscosity
μ_g, μ_f	Gas and liquid dynamic viscosity

α_g	Gas thermal diffusivity
κ_g, κ_f	Thermal conductivities of gas and liquid phases
c_{Tf}, c_{Tg}	Isothermal sound speeds in liquid and gas phases
C_M	Added–mass coefficient of a sphere (0.5)
τ_p	Particle momentum relaxation time
τ_θ	Particle thermal relaxation time
U_g, U_p, U_f	Mean velocities of gas, particle, and liquid phases
ϕ_g, ϕ_p, ϕ_f	Mean volume fractions of gas, particle, and liquid phases
ρ_g, ρ_p, ρ_f	Mean densities of gas, particle, and liquid phases
P_g, P_p, P_f	Mean pressure of gas, particle, and liquid phases
T_g, T_p, T_f	Mean temperatures of gas, particle, and liquid phases
R_b	instantaneous bubble radius
T'_g, T'_p, T'_f	Temperature perturbations
p'_g, p'_f	Pressure perturbations
$\rho'_f, \rho'_p, \rho'_g$	Density perturbations
u'_g, u'_p, u'_f	Velocity perturbations
ϕ'_g, ϕ'_p, ϕ'_f	Volume–fraction perturbations
Q'_{gp}	Perturbed interphase heat transfer
F'_{QS}, F'_{AM}	Perturbed quasi–steady and added–mass forces
ε	Perturbed bubble radius

$k = k_r + ik_i$	Complex wavenumber
ω	Angular frequency of acoustic perturbation
$D = \omega/k$	Phase velocity of acoustic perturbation
a	Speed of sound in gas
γ	Ratio of specific heats
R	Specific gas constant for air
$\eta = \rho_g/\rho_p$	Density ratio
$\delta = \phi_p/\phi_g$	Volume fraction ratio
$B = (\rho_p\phi_p)/(\rho_g\phi_g)$	Momentum coupling parameter
$B_2 = \gamma(C_{pp}/C_p)B$	Thermal coupling parameter
ϵ, ϵ_2	Added mass parameters
$\alpha = C_M(\phi_p/\phi_g)$	Added mass volume–fraction ratio
$z = a^2/(\gamma D^2)$	Non-dimensional pressure parameter
$\Omega = \omega\tau_p$	Dimensionless frequency
$k^+ = k_r^+ + ik_i^+$	Non-dimensional complex wavenumber
k_i^+	reduction factor
ξ	Distance traveled across the mixture
$\xi^+ = \xi/D_j$	Non-dimensional distance traveled across the mixture
D_j	Jet nozzle diameter
M_j	Jet Mach number

R_j	Jet Reynolds number
f	Frequency of the acoustic perturbation [Hz]
U_j	Jet mean velocity
St	Strouhal number fD_j/U_j
A_0, $A(\xi)$	Reference and attenuated acoustic amplitudes
I	Acoustic intensity
N	Particle number density [$1/\mathrm{m}^3$]
σ_{scat}	Scattering cross-section of a single particle
$g = \rho_p/\rho_f$	particle to host fluid density ratio
$h = c_p/c_f$	Sound-speed ratio (particle to host fluid)
a_l	Complex scattering coefficient for spherical particle
L	Thickness of the particle mixture region
R_{phys}	Normalized physical attenuation ratio
DB/ξ^+	Normalized noise reduction
β_f, β_g	Coefficients of thermal expansion for liquid and gas phases
β_T	Total damping coefficient of bubble oscillation
β_μ	Viscous damping coefficient $= 2\mu_f/(\rho_f r_b)$
β_{ac}	Acoustic–radiation damping coefficient $\omega^2/(4c_{Tf})$
σ	Surface tension at bubble interface
ω_0	Natural (resonance) frequency of bubble oscillation

1 Introduction

Noise pollution is just one of many environmental issues that face the aviation industry; it is part of the larger context of local air quality, combustion emissions, environmental compatibility, policies and regulations and public health. Jet noise, especially from military aircraft, represents a significant and growing concern due to its impacts on both the environment and public health. Chronic exposure to high noise levels has been consistently linked to a range of negative health outcomes. Studies show that individuals living near military airbases experience heightened stress levels, increased blood pressure, and other symptoms of cardiovascular distress as a result of ongoing exposure to jet noise [8]. Furthermore, The physiological stress induced by jet noise has a particularly detrimental effect on sleep, leading to disturbances that can contribute to a variety of health issues, such as hypertension and heart disease. Furthermore, the noise produced by military aircraft, especially during night-time operations, significantly impacts the sleep quality of those living in proximity to military bases. Disrupted sleep has been associated with increased daytime sleepiness, impaired cognitive performance, and long-term health risks [1].

There are a variety of well-established procedures and metrics for relating sound measurements to human annoyance, these take account of the non-uniform response of the human ear both in frequency and amplitude, sensitivity to tonal versus broadband noise, and levels of background noise. For a single aircraft operation these effects are usually represented by EPNL measured in decibels (EPNdB) [1]. The Federal Aviation Administration (FAA) in the U.S. has implemented detailed noise certification requirements in Federal Aviation Regulation (FAR, 2005). For instance, the maximum noise levels should not exceed the limit of 108 EPNdB during approach and flyover stages.

However, localized effects, particularly in training ranges, remain a concern. An example of the practical implications are the Navy pilot training for aircraft carrier landings, because as noise levels from commercial aviation have seen a considerable decline over the past few decades, largely due to technological advancements in engine design and regulatory efforts,

military aviation has faced more complex challenges in reducing noise. This discrepancy arises because military aircraft are primarily designed for performance, with a focus on speed, maneuverability, and combat readiness. As a result, military jets tend to generate higher levels of noise compared to their commercial counterparts, particularly when high-thrust engines and afterburners are in use. The EPNdB for military aircraft, especially fighter jets, remains substantially higher than for commercial planes, as can be seen in Figure 1.1.

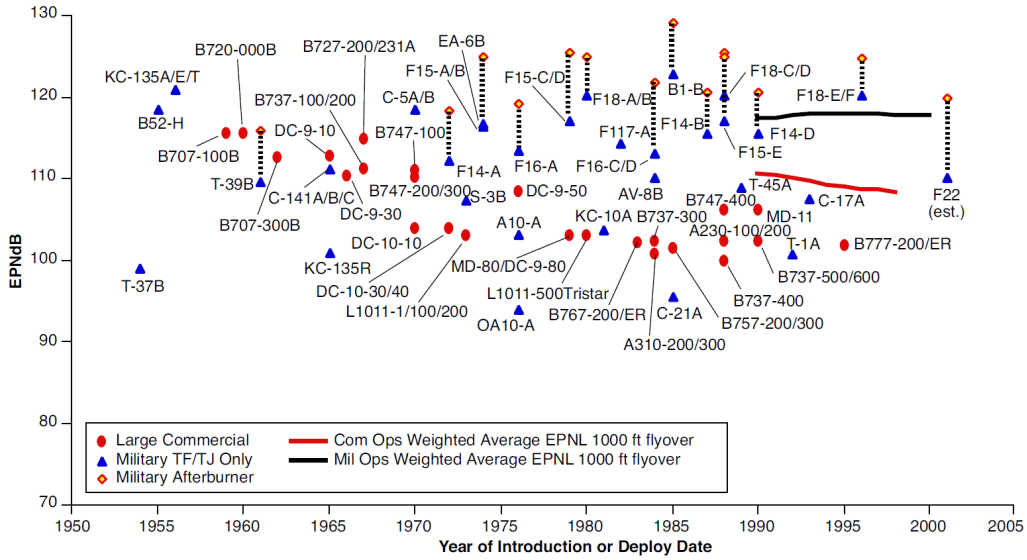

Figure 1.1 Effective perceived noise level for military and commercial aircraft, 1000 ft (305 m) flyover operation [1].

1.1 Origin of Noise in Aircraft

Generally, for conventional aircraft configurations the overall noise signature can be grouped into three primary categories: airframe, propulsion, and interference noise as shown in Figure 1.2. As illustrated in Figure 1.3, airframe noise becomes the dominant contributor during approach, when the engines operate at low thrust and aerodynamic interactions around high-lift devices and landing gear intensify. In contrast, during takeoff the propulsion system is the principal source of noise, where the major contributors include the fan and compressor, the turbine, and the exhaust jet. Among these mechanisms, jet noise is typically the most significant under high-thrust operating conditions, being especially true

during takeoff, when the exhaust plume remains close to ground-based observers and measurement systems, leading to elevated sound-pressure levels and increased community noise exposure.

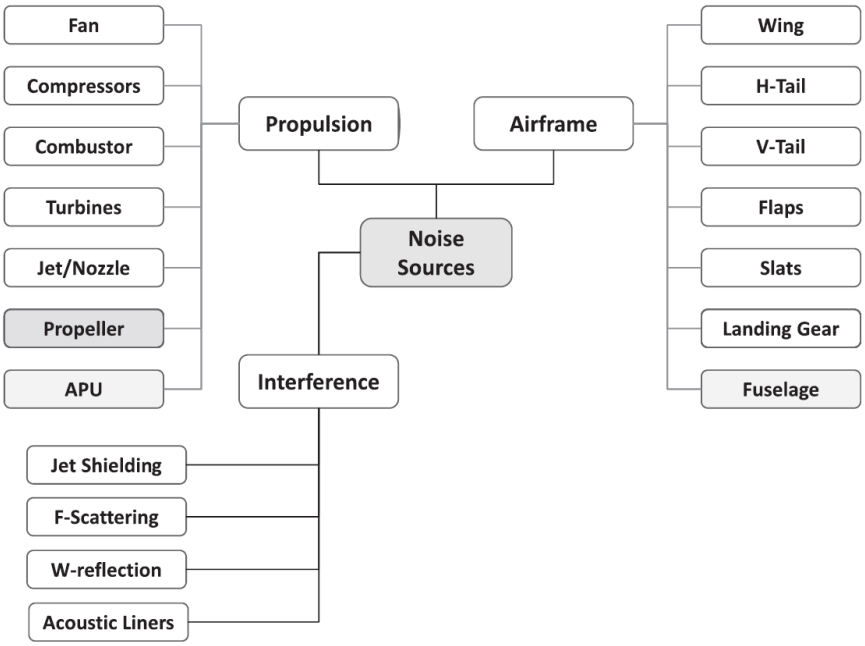

Figure 1.2 Noise-sources breakdown in a conventional airplane[1].

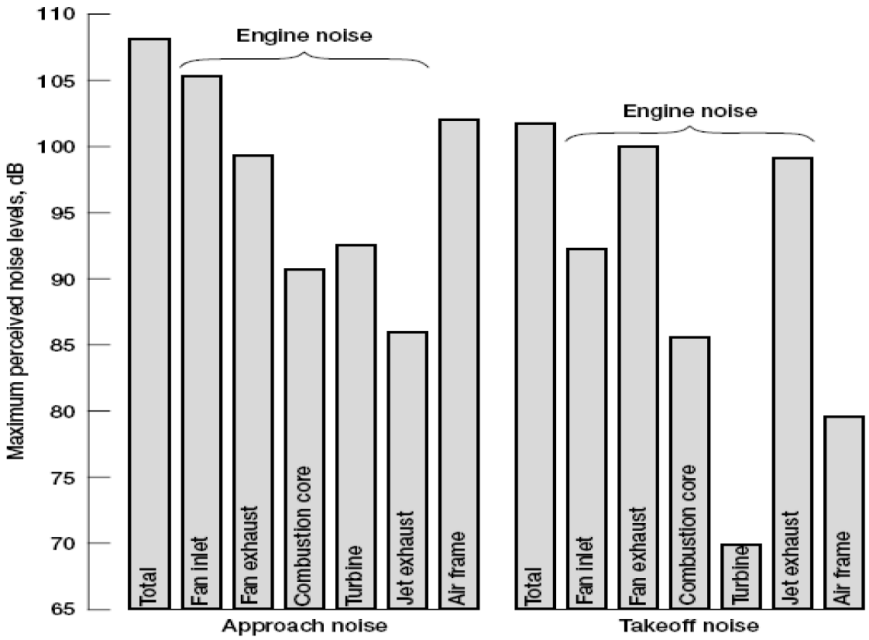

Figure 1.3 Typical modern aircraft noise levels[2].

1.2 The Physics of Free Jet and Its Radiated Noise

Jet exhaust noise arises from unsteady flow fluctuations in the jet shear layer, driven by the turbulent mixing of exhaust gases with the ambient atmosphere. Near the exhaust duct, small-scale turbulent structures with high energy generate high-frequency noise, while further downstream, larger turbulent structures are responsible for low-frequency noise. In supersonic jets, the shock-cell pattern formed within the jet core introduces an additional source of noise.

A general theory for sound generated aerodynamically from a source was developed by Lighthill [9] and has been the main theory towards understanding jet mixing noise. Lighthill chose to formulate the problem by comparing the full equations of motion with the equations that governs density fluctuations in a uniform acoustic medium at rest. The differences were considered to be the effect of a fluctuating force field, acting on the uniform acoustic medium. Ffowcs Williams [10] provided a more complete analysis of the effects of convection as well as the effect of the relative motion of the jet exhaust and the observer.

During the 1970s, it became evident that large-scale turbulent structures within the jet mixing layer act as highly efficient radiators of noise in high-speed jets. Seminal studies by Crow and Champagne[11] and by Brown and Roshko [3] documented the existence of large coherent structures in turbulent jets and free shear layers, extending the classical understanding of turbulence, which had previously emphasized only small-scale eddies. There are many researches on large turbulence structures in high-speed shear flows, a short list of them are Refs. [12],[13],[14],[15],[16],[17].

Large-scale turbulent structures in high Reynolds number jets exhibit a key characteristic: although their occurrence is non-deterministic in both space and time, each event appears as a sequence of structures whose scale progressively increases along the axial direction. These structures originate from Kelvin–Helmholtz instabilities near the nozzle exit, which develop into nonlinear waves and subsequently evolve into large turbulent formations accompanied by fine-scale turbulence [4] as can be seen in Figure 1.4.

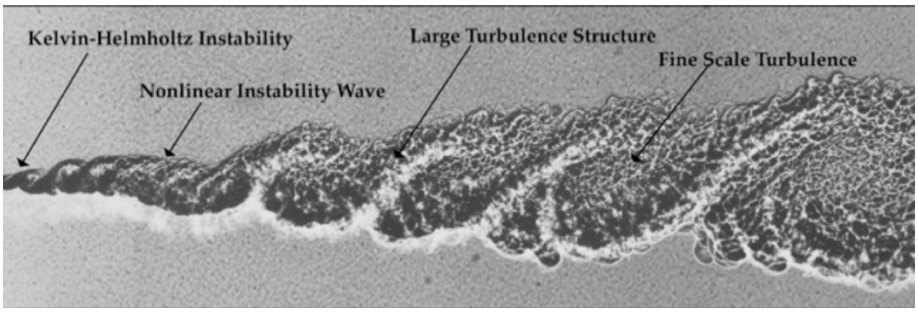

Figure 1.4 Evolution of a Kelvin–Helmholtz instability wave into a nonlinear wave then to large turbulence structures and fine-scale turbulence[3].

Experiments show that jet flows contain two self-similar regions where both the mean velocity profile and the root-mean-square turbulence fluctuations exhibit self-similarity. This duality implies that jet noise may also possess two similarity spectra. Region 1 is associated with fine-scale turbulence fluctuations, which emit short sound pulses in all directions and produce high-frequency noise. Region 2 corresponds to large-scale turbulent structures, which act like a moving wavy wall and generate low-frequency noise [18].

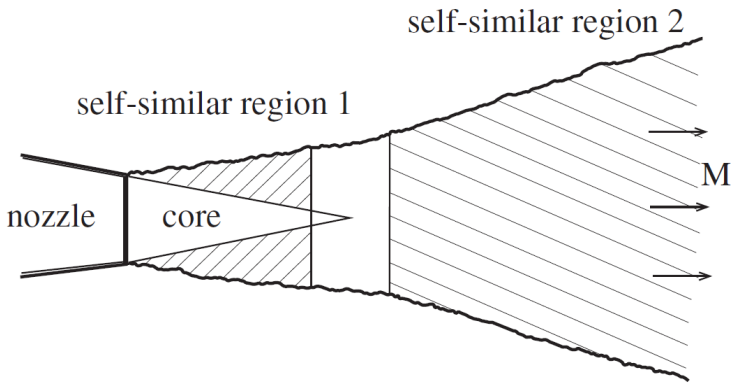

Figure 1.5 Two self-similar regions in a high-speed jet.[4]

This confirms the earlier hypothesis of Mankbadi and Liu [19] in calculating the noise as based on two sources, the large-scale structure, and the fine-scale turbulence.

In addition to turbulent mixing noise, imperfectly expanded jets produce an additional noise source due to the formation of a shock-cell structure within the flow. The interaction between turbulence in the jet mixing layer and the shock-cell system generates the so-called

shock-associated noise. This component consists of two distinct parts: (1) tonal screech noise and (2) broadband noise.

Tonal screech noise was first reported by Powell [20] and later examined in detail by several researchers. The widely accepted explanation is based on an acoustic feedback mechanism linking the nozzle and the jet's shock-cell structure. In this process, vorticity disturbances generated at the nozzle lip are convected downstream, where they interact with the quasi-periodic shock-cell pattern of the jet plume. This interaction produces acoustic waves that propagate upstream toward the nozzle, triggering new disturbances and thereby closing the feedback loop. The resonance of this loop gives rise to discrete, high-intensity tonal emissions like a whistle, rather than a random noise.

Broadband shock-associated noise (BBSAN), while related to screech, differs in its generation mechanism because it does not involve a resonant feedback loop. Initial investigations were carried out by Martlew [21], followed by Harper-Bourne and Fisher [22], who extended Powell's model to describe this phenomenon. BBSAN originates from the random interactions between turbulent eddies in the mixing layer and the shock-cell system, producing a broadband acoustic signature. Further studies, established clear links between turbulence-driven pressure fluctuations and measured acoustic fields.

1.3 Jet Noise Control

Jet noise suppression has been a persistent challenge in aeronautical engineering since the advent of the first-generation turbojet engines nearly eight decades ago. Significant theoretical and experimental research has been conducted worldwide to address this issue. Noise reduction strategies are generally categorized into passive and active control methods.

1.3.1 Passive Control

The classical passive control approach relies on fixed configurations features that permanently modify the flow field, such as geometric modifications. Because turbulence is the dominant source of broadband noise, controlling the mixing process between the jet and the surrounding medium is central to reducing noise from large-scale structures. Common

examples include chevrons and serrated nozzles. These devices operate without external energy input, relying instead on geometry to promote earlier mixing, weaken large turbulent structures, and enhance fine-scale turbulence. The resulting increase in small-scale turbulence near the nozzle tip produces greater momentum thickness, which further contributes to noise suppression. Experimental studies have shown that specific chevron nozzle designs can achieve up to approximately 3 dB of noise reduction during takeoff while incurring less than a 0.5% loss in thrust during cruise [23].

Bypass engines also generate less noise than equivalent turbojets. For a given thrust, the bypass air acts as a co-flowing jet that reduces noise through two mechanisms: First, it decreases the velocity gradient in the initial jet region, thereby limiting the growth of large-scale turbulent structures responsible for strong noise generation. Second, as the inner jet noise propagates through the outer co-flowing stream, part of its energy is attenuated through absorption and reflection, reducing the overall acoustic output.

Another form of passive control relevant to the present study is jet-noise reduction through fluidic injection, which can be implemented using either gaseous or aqueous media. In this work, the focus is placed exclusively on aqueous injection. This method reduces jet noise by lowering the main jet temperature through droplet evaporation and decreasing the jet velocity via momentum exchange between the injected water droplets and the primary jet flow.

The first experimental investigation of this technique was conducted by Kurbjun [24] in 1958, who measured the sound attenuation produced by injecting high-pressure water into the exhaust of an afterburning jet engine, reporting a maximum reduction of approximately 6 dB in overall sound pressure level. Zoppellari and Juve [25] studied the ability of water injection to reduce noise from high velocity jets, obtaining that the maximum reduction was obtain when the water was injected close to the nozzle exit with a maximum noise reduction of 2 dB in overall level. Norum [5] conducted experiments using convergent and convergent–divergent nozzles representative of full-scale aircraft. Acoustic data were obtained with a microphone

array while water was injected through a pressurized ring manifold with multiple injector configurations leading to substantial reductions in radiated shock noise. In contrast, its effect on jet mixing noise is more limited and because the greatest noise reduction occurs in the upstream direction—where baseline noise levels are already lower—while reductions in the louder downstream direction are smaller, the overall improvement in perceived noise remains limited.

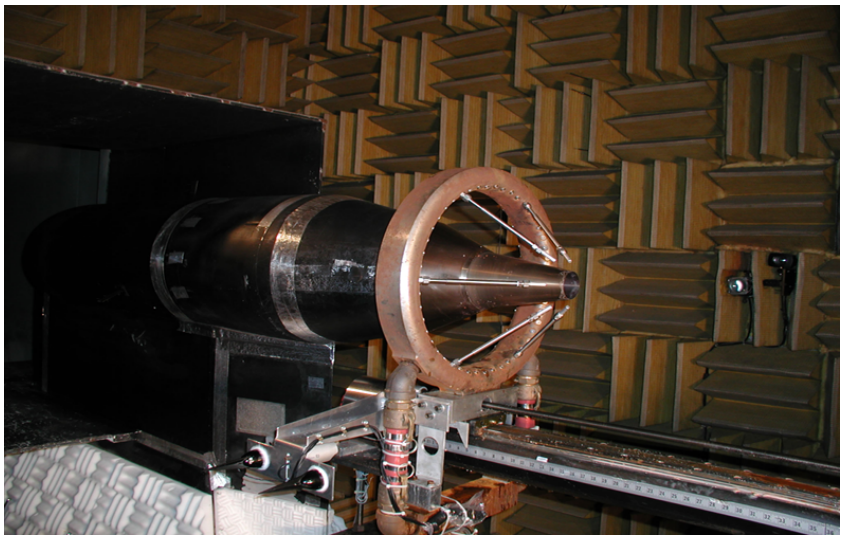

Figure 1.6 Water injection hardware with 6 injectors positioned for injection at nozzle exit [5].

Henderson [26] has reviewed the aspects of fluid injection for jet noise reduction and present that the most efficient water-injection systems for jet noise reduction yields to reductions of about 6 dB in overall sound pressure level.

Moreover, Salehian and Mankbadi [6] investigated noise suppression using pad-injected water as an analog for rocket launch noise control. Large-eddy simulations coupled with a volume-of-fluid model reproduced the baseline impingement dynamics and matched experimental near-field pressure levels.The main result was a broadband noise reduction of about 2–3 dB at low frequencies (below 4 kHz), consistent with measurements, while higher-frequency suppression was overpredicted. The authors concluded that water injection mitigates noise primarily by reducing large-scale shear-layer and wall-jet fluctuations, thereby

weakening the dominant low-frequency acoustic sources. Additional mechanisms include disruption of coherent vortices and partial scattering of acoustic waves by droplets. Overall, the study established pad water injection as an effective strategy for attenuating the most critical low-frequency components of rocket launch noise, while emphasizing the need for accurate droplet modeling to capture high-frequency effects.

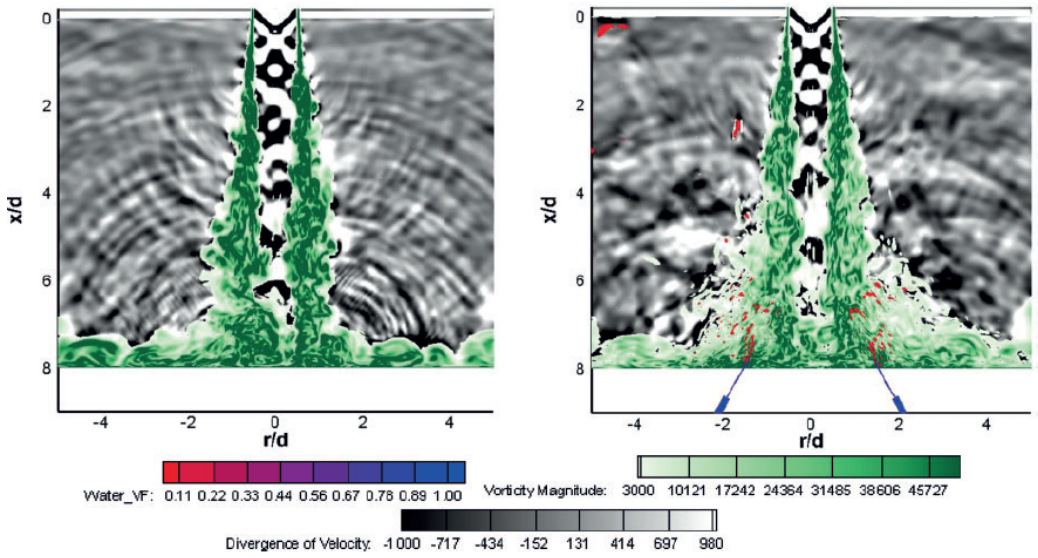

Figure 1.7 Instantaneous contours of dilatation, vorticity, and phase fraction [6].

1.3.2 Active Control

While the present work focuses on passive control methods for jet noise suppression, it is important to contrast these with active control approaches that have been extensively investigated in the literature. Active control is distinguished by its use of actuators that can be selectively operated to introduce external perturbations into the jet, thereby modifying the flow and acoustic field in real time. Unlike passive methods, which rely on fixed geometric or flow modifications, active strategies offer on-demand flexibility and can be tuned to different operating conditions. The following studies illustrate key developments in active control of jet noise.

Within this context, one of the most extensively studied mechanisms is excitation of instability waves in the jet shear layer, where external forcing is used to manipulate coherent

structures that dominate mixing and noise generation. Mankbadi [27] reviewed the dynamics of large-scale coherent structures in turbulent jets and their role in active noise control. Using nonlinear stability theory and integral energy methods, the study showed how fundamental, subharmonic, and harmonic wave interactions govern jet mixing, turbulence transfer, and acoustic radiation. Particular emphasis was placed on the resonance between fundamental and subharmonic modes, which leads to vortex pairing and substantial modification of jet spreading and noise generation. The review highlighted that controlled excitation at specific Strouhal numbers can either enhance or suppress mixing and turbulence, thereby providing an effective mechanism to reduce jet noise. These results established the theoretical foundation for active control strategies based on externally imposed perturbations.

Building on this theoretical groundwork, more recent high-fidelity simulations have directly tested these ideas. For example, Malczewski et al.[28] applied large-eddy simulations to examine whether harmonic interactions could reduce dominant noise sources in a supersonic rectangular jet. A baseline analysis of a Mach 1.5 heated rectangular jet showed that the most amplified coherent structure occurred at excitation with Strouhal numberequal to 0.15, which appeared in the near field and as a prominent contribution to the far-field noise. Excitation strategies were then applied through actuation strips at the nozzle lips, with both single mode forcing at the harmonic frequency (St = 0.30) and bi modal forcing at St = 0.15 and 0.30 under different phase lags. The single-mode case reduced the fundamental structure, leading to peak-to-peak reductions of up to 9 dB in the near field and about 1 dB reductions in overall sound pressure level in the major plane. The bi-modal cases further demonstrated the importance of phase lag: while all cases reduced, the phase lags of $\pi/2$ and $3\pi/2$ produced the largest reductions, with the latter achieving up to 13 dB attenuation. Far-field results showed reductions concentrated in the major plane, with overall decreases of up to 1.8 dB across a broad range of directivity angles.

1.4 Noise Reduction Using Multhiphase Flows

The author of this work is interested in studying jet noise reduction through fluidic injection. However, the approach considered here does not involve direct injection into the jet to alter the turbulence of the flow. Instead, the focus is on a multiphase layer placed outside the jet's core region, where attenuation occurs due to acoustic propagation through a multiphase medium.

Noise suppression using multiphase layers has been investigated by several researchers, providing a foundation for the present study. Early theoretical work by Dobbin and Temkin [29] developed a theoretical model for sound propagation in a gas–particle mixture in which the governing equations for the one-dimensional flow of a gas-particle mixture with interphase transfer of momentum and energy, were linearized to obtain expressions for attenuation and dispersion of acoustic waves due to particle relaxation (both dynamic and thermal). Predictions were compared against laboratory experiments using aerosols and they obtain that particulate flow are inefficient in attenuating low-frequencies perturbation, however, particulate damping remains an important mechanism to attenuate transverse-mode instabilities, which occur at high frequencies. Furthermore, they found that particle concentration and size are key factors in controlling acoustic combustion instabilities.

Building on this theoretical foundation, Cole and Dobbins[30] examined how suspended liquid droplets within a warm fog influence the propagation of sound, with particular focus on attenuation mechanisms. The experimental configuration consisted of a controlled fog chamber in which droplet concentration and temperature could be regulated. Acoustic signals of varying frequencies were transmitted through the chamber, and attenuation was quantified as a function of both fog characteristics and acoustic parameters. The results showed that at low frequencies, attenuation was negligible, but as frequency increased, sound energy loss became progressively more significant.Furthermore, attenuation was most pronounced when the characteristic particle relaxation time matched the acoustic period, i.e., when the acoustic frequency multiply by the momentum response time is close to the

unity, In this regime, momentum exchange between the oscillating gas and droplets was most efficient, leading to maximum acoustic energy dissipation. Additionally, because the experiments were conducted in a warm fog environment, droplet evaporation and heat transfer processes introduced an additional channel for energy exchange, supplementing viscous drag. This dual mechanism of momentum and thermal relaxation provided a more comprehensive explanation of the discrepancy of experimental data with previous analytical models. Agreement was generally strong, particularly within the frequency ranges of practical relevance. Deviations at the highest frequencies were attributed to non-idealities in droplet distribution and chamber conditions.

Subsequent work shifted toward droplet curtains with higher concentrations and controlled spray parameters. Mahanta et al.[7] designed an experiment to quantify acoustic attenuation in air laden with atomized liquid droplets. A loudspeaker generated plane progressive waves at one end of a rigid tube while three twin-fluid nozzles produced a droplet curtain. Attenuation per unit length was computed from pressure amplitudes at two axial locations via a logarithmic relation, enabling consistent comparison across test conditions. The study systematically varied four levers that determine droplet dynamics and gas–particle coupling: (i) air-to-liquid mass flow ratio, droplet mass fraction, atomization pressure (primary setter of particles mean diameter), and droplet material (water or paraffin). Ancillary tests characterized tube structural modes and estimated wall losses, ensuring observed attenuation was dominated by droplet–gas interactions rather than rig artifacts. Results showed that attenuation increased with frequency, reaching a maximum in the range of 6–7 kHz before decreasing slightly at higher frequencies. Also, increasing air-to-liquid mass flow ratios, were found to be most effective in the noise reduction, yielding peak reductions of about 6 dB/m. Increasing droplet concentration enhanced attenuation, though with diminishing returns beyond a mass fraction of about 0.4, due to condensation, coagulation, and settling effects. Comparisons between water and paraffin oil droplets indicated similar attenuation at low frequencies, while paraffin produced slightly greater reductions at higher frequencies,

likely owing to its lower surface tension and finer atomization. Spatial measurements showed that sound levels decayed rapidly close to the source but leveled off further downstream. The study concluded that droplet size is the dominant factor in acoustic absorption and the most effective attenuation occurs in the mid-frequency band of 4–8 kHz, with limited performance at lower frequencies.

While these earlier studies largely employed linear relaxation theory, Kandula [31] extended the framework by incorporating nonlinear drag and heat transfer, which become important at higher particle Reynolds numbers and larger droplet sizes. The analysis predicted that, unlike the monotonic behavior expected under linear Stokesian relaxation, the absorption coefficient exhibits a spectral peak at finite values of the dimensionless parameter $\omega\tau_d$, where $\omega\tau_d$ is the droplet relaxation time. Below $\omega\tau_d \approx 0.7$, nonlinear effects are negligible and the results align with classical Temkin and Dobbins [29] theory, but at higher values the nonlinear formulation predicts a decrease in attenuation with increasing frequency. The comparison with experimental measurements by Norum [5] on water injection into a perfectly expanded supersonic jet showed that the nonlinear model reproduced the spectral shape of attenuation. The findings established that nonlinear particle relaxation processes are primarily responsible for reducing absorption at high frequencies and that linear theories alone are insufficient to capture the observed attenuation spectra in realistic jet flows with injected droplets. Kandula [31] concluded that accounting for nonlinear drag and heat transfer is essential for accurate prediction of noise suppression in droplet-laden jets, and that the mechanism of spectral peaking is a robust feature of multiphase acoustic damping in dilute suspensions. Two years later, Kandula [32] extended the framework to study sound attenuation and dispersion in saturated gas–vapor–droplet mixtures by including droplet evaporation and transpiration effects in the theoretical formulation. The results showed that accounting for transpiration and mass transfer significantly improved the agreement between theory and the experimental data of Cole and Dobbins [30] for sound attenuation in air–water fogs at low droplet mass concentrations.

More recent work has focused on practical implementations of droplet curtains for noise reduction. Herrero et al. [33] carried out an experimental investigation to evaluate the ability of layered water-droplet curtains to attenuate sound across a broad frequency range. The setup employed three successive droplet sheets, with different nozzle types and injection pressures tested to determine their influence on attenuation spectra. The results showed that increasing the injection pressure enhanced attenuation, reflecting the role of finer atomization and smaller droplet sizes in strengthening gas–particle coupling. The system achieved improved broadband performance, particularly in the high-frequency range, when greater heterogeneity in droplet size distribution where obtained. Overall, the work concluded that acoustic attenuation by droplet layers can be optimized by increasing atomization pressure and tailoring droplet size distribution through nozzle selection. The authors highlighted that mid-band attenuation is primarily governed by curtain thickness, while high-frequency performance benefits from droplet heterogeneity.

1.5 Overview of the Present Study

Motivated by these previous studies, the present work investigates a droplet curtain positioned outside the jet influence region, such that the observed attenuation results from the propagation of sound through a multiphase mixture of air and water rather than from modifications to the jet turbulence. A representative example of this concept is shown in Figure 1.8, which illustrates the use of an air–water mixture shield for the reduction of supersonic jet noise during aircraft operations.

In this framework, the mean flow field of the air surrounding the jet and the radiated jet noise are assumed to be known. The analysis focuses on the perturbations associated with the sound waves as they travel through the surrounding air–water mixture. The governing perturbation equations, treated as acoustic wave equations, are solved to determine the resulting reduction in sound level (in decibels) as the waves propagate across the mixture. This approach offers two key advantages:

1. Because the acoustic perturbation equations are solved directly, the prediction of sound

propagation and attenuation is more accurate than that obtained from conventional LES-based methods.

2. The computational cost is significantly lower than that of full LES simulations, enabling extensive parametric studies of the governing physical parameters for noise reduction.

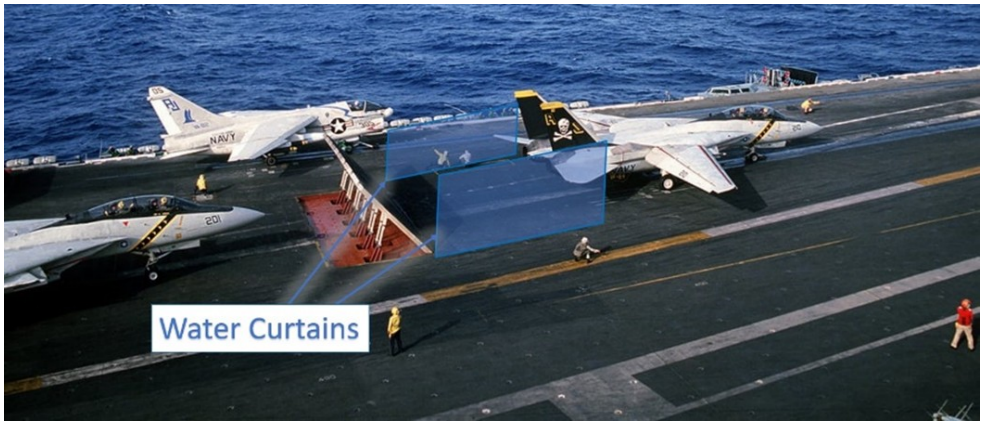

Figure 1.8 Schematic showing the use of a water–air curtain to reduce supersonic jet noise. Adapted from the U.S. Navy public-domain image (Defense Media Activity Center, photo by PH3 D. Dostie, ID DN-ST-84-11502) via NavSource Online: Aircraft Carrier Photo Archive (https://www.navsource.net/archives/02/0270ai.jpg).

The remainder of this document is organized as follows: Chapter 2 presents the theoretical framework for the particle flow, beginning with the governing equations for multiphase systems. These equations are subsequently linearized and analyzed under small perturbations to describe the acoustic behavior of the mixture. The suspended droplet case is first examined, where no mean flow is assumed within the mixture. Both, analytical and numerical solutions are developed to evaluate the influence of volume fraction, droplet size, and flow parameters such as the Strouhal number on acoustic attenuation. In addition, numerical simulations based on Computational Fluid Dynamics (CFD) are performed to validate the theoretical predictions, and the results are compared with available experimental data from the literature to ensure model accuracy. Subsequently, The analysis is then extended to the dispersed droplet case, where the effect of interphase slip on sound attenuation is investigated. Chapter 3 applies the same methodology to the bubbly flow configuration, detailing

the derivation of the perturbed equations, parametric analyses, and comparison with experimental measurements. Finally, Chapter 4 summarizes the main findings for both particle and bubbly cases, highlights the key mechanisms governing multiphase noise attenuation, and outlines potential directions for future research.

1.6 Objectives

As discussed in this chapter, the challenge of jet noise mitigation has motivated the search for alternative passive control strategies. Among these, multiphase media offer a promising approach by attenuating acoustic energy through interphase momentum and thermal relaxation. Building on the theoretical background and experimental evidence reviewed above, this work aims to model, quantify, and validate jet noise attenuation using air–water mixtures positioned outside the jet's region of influence. Accordingly, the following objectives are defined.

1.6.1 General Objectives

To investigate the attenuation of acoustic waves in air–water mixtures through a perturbation-based modeling framework.

1.6.2 Specific Objectives

1. To derive and linearize the governing equations of multiphase flow by separating flow varibales into mean and perturbation components, thereby formulating the corresponding multiphase flow perturbation equations.

2. To solve the linearized perturbation equations and quantify the influence of key parameters such as dispersed-phase size, volume fraction, and convective slip on acoustic wave attenuation.

3. To validate the analytical and numerical predictions through CFD simulations and comparison with experimental data available in the literature.

2 Methodology, Particle Case

In the present work, the focus is on the region outside the jet flow, as illustrated in Figure 3.1. Immediately beyond the jet boundary, the surrounding medium consists of ambient air. At a certain radial distance, an air–water curtain is introduced, forming a localized multiphase domain. The multiphase flow equations are applied within this domain and then the flow is decomposed into mean and perturbation components to obtain the linearized perturbation equations that are used to describe the propagation and attenuation of acoustic waves in the multiphase domain.

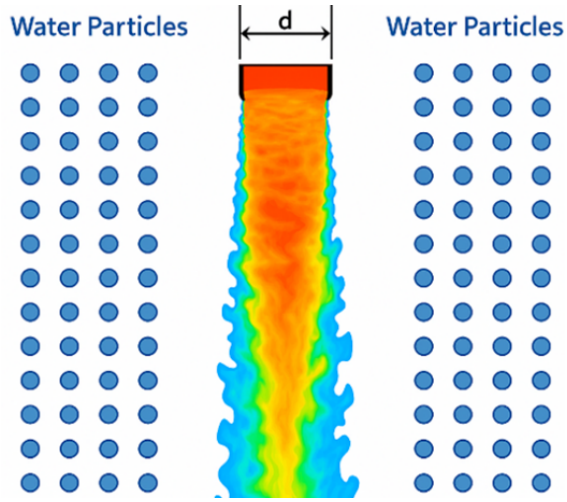

Figure 2.1 Air-water mixture surrounding the jet.

2.1 The Governing Equations

The sound passing through a mixture of air and water droplets is considered here. We start with an Eulerian approach for the gas and water droplets. The following assumptions were made: (1) the air is a perfect gas; (2) the air motion may be regarded as inviscid, so its viscosity and conductivity are neglected except in the interaction with the water particles; (3) the water particles are spherical and not evaporating and their density ρ_p is constant; (4) The averaging volume is assumed to be sufficiently large compared to the particle size and spacing, such that the volume-averaged quantities are well-defined and represent smooth continuum fields; (5) volume-averaged Reynolds stresses are neglected; (6) the particles do

not collide with each other; (7) all the phases share the same pressure field $P_g = P_p$; (8) Thermal and acoustic effects dominate over mechanical work; (9) Mean temperature for the fluid T_g and particles T_p are equal, and (10) body forces are neglected. Following Crowe [34], and Mankbadi and Balachandar[28], the continuity, momentum, and energy equations for the gas in the three-dimensional Eulerian system are represented as:

$$\frac{\partial(\rho_g \Phi_g)}{\partial t} + \nabla \cdot (\Phi_g \rho_g \mathbf{u}_g) = 0, \tag{2.1}$$

$$\frac{\partial(\rho_g \Phi_g \mathbf{u}_g)}{\partial t} + \nabla \cdot (\Phi_g \mathbf{u}_g \mathbf{u}_g) = -\Phi_g \nabla p_g - \mathbf{F}_{QS} - \mathbf{F}_{AM}, \tag{2.2}$$

$$\frac{\partial(\rho_g \Phi_g E_g)}{\partial t} + \nabla \cdot (\rho_g \Phi_g H_g \mathbf{u}_g) = -\Phi_p \mathbf{u}_p \cdot \nabla p_g - \mathbf{u}_p \cdot \mathbf{F}_{QS} - \mathbf{u}_g \cdot \mathbf{F}_{AM} - Q_{gp}. \tag{2.3}$$

Likewise, for the water particles phase, the continuity, momentum, and energy equations are given by:

$$\frac{\partial \Phi_p}{\partial t} + \nabla \cdot (\Phi_p \mathbf{u}_p) = 0, \tag{2.4}$$

$$\rho_p \left[\frac{\partial (\mathbf{u}_p \Phi_p)}{\partial t} + \nabla \cdot (\Phi_p \mathbf{u}_p \mathbf{u}_p) \right] = -_p \nabla p_p + \mathbf{F}_{QS} + \mathbf{F}_{AM}, \tag{2.5}$$

$$\rho_g \left[\frac{\partial (\Phi_p E_p)}{\partial t} + \nabla (\mathbf{u}_p \Phi_p E_p) \right] = -\Phi_p \mathbf{u}_p \cdot \nabla p_p + \mathbf{u}_p \cdot \mathbf{F}_{QS} + \mathbf{u}_p \cdot \mathbf{F}_{AM} + Q_{gp}. \tag{2.6}$$

The quantities $\mathbf{u}$, p, E, ρ, and Φ denote the velocity vector, pressure, total energy, density, and volume fraction, respectively. Subscripts p and g are used to distinguish variables associated with the water droplet phase and the carrier gas phase, respectively.

The quasi-steady force F_{QS}, and the added mass force F_{AM} are given by:

$$\mathbf{F}_{QS} = \frac{18\mu_g}{d_p^2} (\mathbf{u}_g - \mathbf{u}_p) \Psi(\mathrm{Re}) \phi_p, \tag{2.7}$$

$$\mathbf{F}_{AM} = -C_M \phi_p \nabla p_g - C_M \left[\frac{\partial \left(\phi_p \rho_g \mathbf{u}_p \right)}{\partial t} + \nabla \cdot \left(\phi_p \rho_g \mathbf{u}_p \mathbf{u}_p \right) \right] \tag{2.8}$$

The total energy and enthalpy per unit volume are given by:

$$E_g = C_v T_g + \frac{|\mathbf{u}_g|^2}{2}, \tag{2.9}$$

$$H_g = C_p T_g + \frac{|\mathbf{u}_g|^2}{2} = E_g + \frac{p_g}{\rho_g}, \tag{2.10}$$

$$E_p = C_{pp} T_p + \frac{|\mathbf{u}_p|^2}{2}, \tag{2.11}$$

Here C_v and C_p are the specific heat of the gas at constant volume and constant pressure, respectively. The heat transfer between the gas and particles Q_{gp} is the normalized by ρ_p ϕ_p to give the specific heat transfer q_{gp}, together with the specific quasi-steady force f_{qs} and the specific added mass force f_{AM} are defined as:

$$q_{gp} = \frac{Q_{gp}}{\rho_p \phi_p} = C_{p,p} \frac{T_g - T_p}{2\tau_\theta} \, \mathrm{Nu}, \tag{2.12}$$

$$f_{QS} = \frac{F_{QS}}{\rho_p \phi_p} = \frac{\mathbf{u}_g - \mathbf{u}_p}{\tau_p} \, \Psi(\mathrm{Re}), \tag{2.13}$$

$$f_{AM} = \frac{F_{AM}}{\rho_p \phi_p} = -C_M \frac{\nabla p_g}{\rho_p} - \frac{C_M}{\rho_p \phi_p} \left[\frac{\partial \left(\phi_p \rho_g \mathbf{u}_p \right)}{\partial t} + \nabla \cdot \left(\phi_p \rho_g \mathbf{u}_p \mathbf{u}_p \right) \right]. \tag{2.14}$$

The function $\Psi(Re)$ is the drag factor which is the ratio of the drag coefficient to the Stokes drag. The correlation by Schiller and Naumann[35] is applied, where:

$$\Psi(\mathrm{Re}) = 1 + 0.15 \, \mathrm{Re}^{0.687}, \tag{2.15}$$

$$\mathrm{Re} = \frac{d_p}{\nu_g} \left| \mathbf{u}_g - \mathbf{u}_p \right|, \tag{2.16}$$

$$\mathrm{Nu} = 2 + \left(0.4\,\mathrm{Re}^{0.5} + 0.06\,\mathrm{Re}^{\frac{2}{3}} \right) \mathrm{Pr}^{0.4}. \tag{2.17}$$

where d_p is the droplet diameter, ν_g is the gas kinematic viscosity, the Reynolds number is Re; Nu and Pr are the Nusselt and Prandtl numbers, respectively. The added mass coefficient is $C_M = 0.5$ for a sphere. The response time scales for the particles quasi-steady force and heat transfer are given by:

$$\tau_p = \frac{\rho_p}{\rho_g} \frac{d_p^2}{18\,\nu_g}, \tag{2.18}$$

$$\tau_\theta = \frac{\rho_p}{\rho_g} \frac{d_p^2}{12\,\alpha_g} \frac{C_{p,p}}{C_{p,g}} = \frac{3}{2} \frac{C_{p,p}}{C_p} \mathrm{Pr}\,\tau_p. \tag{2.19}$$

It is to note that the full form of the governing equations presented in this section is derived using volume averaging in a multiphase mixture, it does not assume any specific value of the gas volume fraction ϕ_g, and remains formally valid as long as $0 < \phi_g < 1$; that is, both the gas and particle phases must be present within the control volume. According to Crowe et al.[34], these equations are not strictly invalid at small values of ϕ_g; however, their physical applicability becomes questionable in dense flow regimes where the particle phase occupies most of the volume and the contact forces dominate the momentum exchange between particles. As presented by Crowe et al.[34] and Sommerfeld[36], such contact-dominated conditions occur when the particle volume fraction exceeds approximately $\phi_p \approx 0.1$. Since the present analysis assumes non interacting droplets and neglects contact forces, the analysis is restricted to cases where $\phi_p \leq 0.1$.

2.2 Particle Perturbed Equations

The flow variables are split into a base flow and perturbation components as:

$$\Phi_p = \phi_p + \phi'_p; \quad \mathbf{u}_p = U_p + u'_p; \quad \mathrm{E}_p = E_p + E'_p \tag{2.20}$$

$$\rho_g = \rho_g + \rho'_g; \quad \mathbf{u}_g = U_g + u'_g; \quad p_g = P_g + p'_g \tag{2.21}$$

The base flow is assumed to be known, and our focus is on the perturbation equations. By combining the derived base relations with the governing equations for the gas, where the energy equation is first replaced by the thermal energy equation and assuming that perturbations in the gas volume fraction are negligible with respect to the gas volume fraction, the perturbed continuity, momentum, and energy equations in generalized curvilinear coordinates for the gas are obtained as follows:

$$\phi_g \frac{\partial}{\partial t}\left(\rho_g + \rho'_g\right) + \phi_g \frac{\partial}{\partial x_i}\left[(\rho_g + \rho'_g)(U_g + u'_g)_i\right] = 0, \tag{2.22}$$

$$\begin{aligned} \phi_g \frac{\partial}{\partial t}\left[(\rho_g + \rho'_g)(U_g + u'_g)_i\right] + \phi_g \frac{\partial}{\partial x_j}\left[(\rho_g + \rho'_g)(U_g + u'_g)_j (U_g + u'_g)_i\right] \\ = -\phi_g \frac{\partial}{\partial x_i}(P_g + p'_g) - \left(\overline{F}_{QS} + F'_{QS}\right) - \left(\overline{F}_{AM} + F'_{AM}\right), \end{aligned} \tag{2.23}$$

$$\begin{aligned} \phi_g \frac{\partial}{\partial t}\left[(\rho_g + \rho'_g)(E_g + E'_g)\right] + \phi_g \frac{\partial}{\partial x_i}\left[(\rho_g + \rho'_g)(U_g + u'_g)_i (H_g + H'_g)\right] \\ = -\left(\overline{Q}_{gp} + Q'_{gp}\right). \end{aligned} \tag{2.24}$$

The same methodology is applied to the water particle phase and the perturbed equations for continuity, momentum, and energy equation are obtained as:

$$\frac{\partial}{\partial t}\left[(\phi_p+\phi_p')\right]+\frac{\partial}{\partial x_j}\left[(\phi_p+\phi_p')(U_p+u_p')_i\right]=0, \tag{2.25}$$

$$\begin{aligned}\rho_p\left(\frac{\partial}{\partial t}\left[(\phi_p+\phi_p')(U_p+u_p')_i\right]+\frac{\partial}{\partial x_j}\left[(\phi_p+\phi_p')(U_p+u_p')_j(U_p+u_p')_i\right]\right)\\ =-(\phi_p+\phi_p')\frac{\partial}{\partial x_i}(P_g+p_g')+(\overline{F}_{QS}+F_{QS}')+(\overline{F}_{AM}+F_{AM}'),\end{aligned} \tag{2.26}$$

$$\rho_p\left(\frac{\partial}{\partial t}\left[(\phi_p+\phi_p')(E_p+E_p')\right]+\frac{\partial}{\partial x_i}\left[(\phi_p+\phi_p')(U_p+u_p')_i(H_p+H_p')\right]\right)=(\overline{Q}_{gp}+Q_{gp}'). \tag{2.27}$$

2.2.1 The Perturbed Equations in Spherical Coordinates

The above system of equations is valid in Cartesian, cylindrical and spherical coordinates. To demonstrate the physics, the air mean-flow and acoustics are taken to be purely radial.

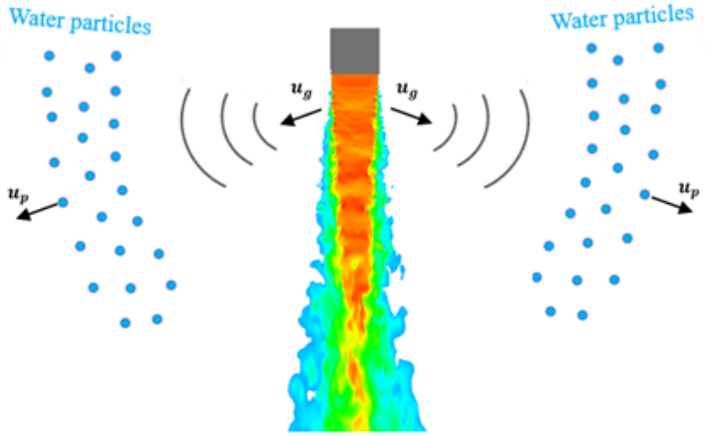

Figure 2.2 Spherical approximation to the flow outside of the jet.

Considering the spherical symmetrical case, Figure 2.2, it is appropriate to rewrite Equations 3.21-2.27 in spherical coordinates. Furthermore, it is assumed that perturbations are

primarily radial; therefore, we neglected all non-radial terms. The space and time changes of the mean flow are assumed to be small with respect to that of the perturbations and the total energy and enthalpy relations from Equations 2.9-2.11 are used to express the energy equation in terms of temperature. Under these assumptions, the perturbation equations for the gas and particles in the radial direction are obtained as follows:

$$\frac{\partial \rho_g'}{\partial t} + \left(\rho_g \frac{\partial u_g'}{\partial r} + U_g \frac{\partial \rho_g'}{\partial r} \right) + \frac{2}{r} \left(\rho_g' U_g + \rho_g u_g' \right) = 0, \tag{2.28}$$

$$\begin{aligned} \phi_g \Bigg[\left(\rho_g \frac{\partial u_g'}{\partial t} + U_g \frac{\partial \rho_g'}{\partial t} \right) + \left(2\rho_g U_g \frac{\partial u_g'}{\partial r} + U_g^2 \frac{\partial \rho_g'}{\partial r} + \frac{\partial p_g'}{\partial r} \right) \\ + \frac{2}{r} \left(\rho_g' U_g^2 + 2\rho_g U_g u_g' \right) \Bigg] + F_{QS}' + F_{AM}' = 0, \end{aligned} \tag{2.29}$$

$$\begin{aligned} \phi_g \Bigg[\left(\rho_g \frac{\partial T_g'}{\partial t} + T_g \frac{\partial \rho_g'}{\partial t} \right) + \gamma \left(\rho_g U_g \frac{\partial T_g'}{\partial r} + \rho_g T_g \frac{\partial u_g'}{\partial r} + \rho_g T_g \frac{\partial \rho_g'}{\partial r} \right) \\ + \frac{2}{r} \left(\rho_g U_g T_g' + \rho_g T_g u_g' + U_g T_g \rho_g' \right) \Bigg] + \frac{1}{C_{vg}} Q_{gp}' = 0. \end{aligned} \tag{2.30}$$

$$\frac{\partial \phi_p'}{\partial t} + \left(\phi_p \frac{\partial u_p'}{\partial r} + U_p \frac{\partial \phi_p'}{\partial r} \right) + \frac{2}{r} \left(\phi_p u_p' + U_p \phi_p' \right) = 0, \tag{2.31}$$

$$\begin{aligned} \rho_p \Bigg[\left(\phi_p \frac{\partial u_p'}{\partial t} + \frac{\partial \phi_p'}{\partial t} U_p \right) + \left(2\phi_p U_p \frac{\partial u_p'}{\partial r} + U_p^2 \frac{\partial \phi_p'}{\partial r} \right) + \frac{2}{r} \left(2\phi_p U_p u_p' + U_p^2 \phi_p' \right) \Bigg] \\ + \phi_p \frac{\partial p_g'}{\partial r} - F_{QS}' - F_{AM}' = 0, \end{aligned} \tag{2.32}$$

$$\rho_p\Bigg[\left(\phi_p\frac{\partial T'_p}{\partial t}+\frac{\partial \phi'_p}{\partial t}T_p\right)+\left(\phi_p U_p\frac{\partial T'_p}{\partial r}+\phi_p T_p\frac{\partial u'_p}{\partial r}+U_pT_p\frac{\partial \phi'_p}{\partial r}\right)+ \\ \frac{2}{r}\left(\phi_pU_pT'_p+\phi_pT_pu'_p+U_pT_p\phi'_p\right)\Bigg]-\frac{1}{C_{pp}}Q'_{gp}=0. \tag{2.33}$$

Where the perturbation components of heat rate transfer from the particles to the fluid; force coupling and added mass force, respectively, are defined below.

$$Q'_{gp}=\frac{\rho_pC_{pp}\,\mathrm{Nu}}{2\,\tau_\theta}\left[\phi'_p(T_g-T_p)+\phi_p(T'_g-T'_p)\right], \tag{2.34}$$

$$F'_{QS}=\frac{\rho_p\,\Psi}{\tau_p}\left[(U_g-U_p)\phi'_p+(u'_g-u'_p)\phi_p\right], \tag{2.35}$$

$$F'_{AM}=-\phi_p\,ikp'_g-C_M\Big[\frac{\partial}{\partial t}\big(\phi'_p\rho_gU_p+\phi_p\rho'_gU_p+\phi_p\rho_gu'_p\big) \\ +\frac{\partial}{\partial r}\big(\phi'_p\rho_gU_p^2+\phi_p\rho'_gU_p^2+2\phi_p\rho_gu'_pU_p\big)\Big]. \tag{2.36}$$

2.2.2 One-Dimensional Spherical Flow Simplifications

For the acoustic, the perturbation follows that of the acoustic radial propagation waves in the form:

$$(\tilde{u},\tilde{\rho},\tilde{p},\tilde{T})=(u',\rho',p',T')\,\frac{e^{ikr-i\omega t}}{r}. \tag{2.37}$$

Here, k is the complex wavenumber, ω is the angular frequency and r is the radial distance from the source. We assume $ikr\gg 1$, that implies that the wave propagates in the far-field regime where the radius r is large compared to the acoustic wavelength. In this region, the wave fronts are approximately planar, the amplitude decays smoothly and the oscillatory behavior becomes well defined. As the perturbations are assumed to be harmonic in time and space, the time and spatial derivatives $\frac{\partial}{\partial t}$ and $\frac{\partial}{\partial x}$ are replaced by —$i\omega$ and ik, respectively. Therefore, the perturbation continuity, momentum, and energy equations for the gas and particles becomes into a system of linear algebraic equations.

$$-i\omega\rho'_g + ik\left(\rho_g u'_g + \rho'_g U_g\right) = 0, \tag{2.38}$$

$$\begin{aligned}\phi_g\Big[-i\omega(\rho_g u_g)' + \phi_g ik\big(U_g(2\rho_g u'_g + U_g\rho'_g) + p'_g\big)\Big] \\ +\rho_p\big[(\phi_p f_{qs})' + (\phi_p f_{AM})'\big] = 0,\end{aligned} \tag{2.39}$$

$$\phi_g\Big[-i\omega(\rho_g T_g)'\Big] + \phi_g ik(\rho_g U_g T_g)' + \frac{\rho_p}{C_v}(\phi_p q_{gp})' = 0, \tag{2.40}$$

$$-i\omega\phi'_p + ik\left(\phi_p u'_p + \phi'_p U_p\right) = 0, \tag{2.41}$$

$$\begin{aligned}\rho_p\Big[-i\omega\phi_p u'_p + ikU_p(2\phi_p u'_p + U_p\phi'_p) - i\omega U_p\phi'_p\Big] + ik\phi_p p'_g \\ -\rho_p\big[(\phi_p f_{qs})' + (\phi_p f_{AM})'\big] = 0,\end{aligned} \tag{2.42}$$

$$-i\omega(\phi_p T_p)' + ik\Big[U_p(\phi_p T_p)' + u'_p(\phi_p T_p)\Big] - \frac{1}{C_{pp}}(\phi_p q_{gp})' = 0. \tag{2.43}$$

2.3 Suspended Droplet Case

For the suspended case, it is assumed that the mean flow velocity is zero and that the mean temperatures of both phases are equal (U_g=U_p= 0 and $T_p = T_g$), under these assumptions, the perturbations equations reduces to:

$$-i\omega\rho' + ik\rho u'_g = 0, \tag{2.44}$$

$$\phi_g\left[-i\omega(\rho u'_g) + ikp'_g\right] + \rho_p\left[(\phi_p f_{qs})' + (\phi_p f_{AM})'\right] = 0, \tag{2.45}$$

$$\phi_g\left[-i\omega(qT'_g)\right] + ik\gamma\phi_g qT_g u'_g + \frac{\rho_p}{C_v}(\phi_p q_{gp})' = 0, \tag{2.46}$$

$$-i\omega\phi'_p + ik\phi_p u'_p = 0, \tag{2.47}$$

$$\rho_p \phi_p (-i\omega u_p') + ik\phi_p p_g' - \rho_p \left[(\phi_p f_{qs})' + (\phi_p f_{AM})' \right] = 0, \tag{2.48}$$

$$-i\omega(\phi_p T_p)' + ik\phi_p T_p u_p' - \frac{1}{C_{pp}}(\phi_p q_{gp})' = 0. \tag{2.49}$$

Both an analytical (asymptotic) solution as well as a direct numerical solution are presented here for the suspended case.

2.3.1 Analytical Asymptotic Solution

To demonstrate the physics involved and the ability of this approach, an analytical solution is derived for the suspended case at small volume of fraction ratios $\delta = \frac{\phi_p}{\phi_g}$.

Starting from the perturbed form of the perfect gas equation:

$$p_g' = R(\rho_g' T_g + \rho_g T_g') \tag{2.50}$$

The perturbation of the gas pressure can be obtained as:

$$p_g' = p_g\left(\frac{\rho_g'}{\rho_g} + \frac{T_g'}{T_g}\right) \tag{2.51}$$

Using the Equation 2.51, the added mass force Equation2.8 can be written as:

$$f_{AM}' = i\omega\epsilon D\left[\frac{u_p'}{D} - z\left(\frac{T_g'}{T_g} + \frac{\rho'}{\rho_g}\right)\right] \tag{2.52}$$

Where,

$$\epsilon = C_M \frac{\rho_g}{\rho_p} \tag{2.53}$$

$$\alpha = C_M \frac{\phi_p}{\phi_g} \tag{2.54}$$

$$z = \frac{RT_g}{D^2} = \frac{a^2}{\gamma D^2} \tag{2.55}$$

$$D = \frac{\omega}{k} \tag{2.56}$$

Here, a is the speed of sound in the gas. Taking into account that $Re = 0$ for the

suspended case, the drag factor and Nusselt number are given by 1 and 2, respectively. Therefore, Gas continuity, momentum, and energy equations for the gas reduce to:

$$\frac{\rho_g'}{\rho_g} = \frac{u_g'}{D} - \frac{\phi_g'}{\phi_g} \tag{2.57}$$

$$\frac{u_g'}{D}\left(1 - \frac{B}{i\omega\tau_p}\right) - z(1-\alpha)\left(\frac{T_g'}{T_g} + \frac{\rho_g'}{\rho_g}\right) + \left(\frac{B}{i\omega\tau_p} - \alpha\right)\frac{u_p'}{D} = 0 \tag{2.58}$$

$$\frac{u_g'}{D}(\gamma - 1) - \frac{T_g'}{T_g}\left(1 - \frac{B_2}{i\omega\tau_\theta}\right) - \frac{B_2}{i\omega\tau_\theta}\frac{T_p'}{T_g} = 0 \tag{2.59}$$

Here,

$$\eta = \frac{\rho_g}{\rho_p}, \tag{2.60}$$

$$\delta = \frac{\phi_p}{\phi_g}, \tag{2.61}$$

$$B = \frac{\rho_p\phi_p}{\rho_g\phi_g} = \delta\frac{\rho_p}{\rho_g}. \tag{2.62}$$

$$B_2 = \gamma\left(\frac{C_{pp}}{C_p}\right)B \tag{2.63}$$

Likewise, the water droplets continuity, momentum, and energy equations reduce to:

$$\frac{\phi_p'}{\phi_p} = \frac{u_p'}{D} \tag{2.64}$$

$$\frac{u_p'}{D}\left(1 - \frac{1}{i\omega\tau_p} + \epsilon\right) - (\eta + \epsilon z)\left(\frac{T_g'}{T_g} + \frac{\rho_g'}{\rho_g}\right) + \frac{1}{i\omega\tau_p}\frac{u_g'}{D} = 0 \tag{2.65}$$

$$T_p' = \frac{T_g'}{1 - i\omega\tau_\theta} \tag{2.66}$$

To obtain a relation between the perturbation variables of the gas and particles, we first eliminate the gas volume of fraction perturbation in Equation 2.57 noting that $\phi'_g = -\phi'_p$

$$\frac{\rho'_g}{\rho_g} = \frac{u'_g}{D} + \delta\frac{u'_p}{D} \tag{2.67}$$

Substituting Equation 2.67 in the added mass force and neglecting higher order terms, the gas and particles momentum equations become:

$$\left(\frac{u'_g}{D}\right)\left[1-(1-\alpha)z-\frac{B}{i\omega\tau_p}\right]-(1-\alpha)z\frac{T'_g}{T_g}+\left[\frac{B}{i\omega\tau_p}-\alpha-\delta z\right]\frac{u'_p}{D}=0 \tag{2.68}$$

$$\frac{u'_g}{D}\left(1-\frac{1}{i\omega\tau_p}+\epsilon\right)=\epsilon_2 z\frac{T'_g}{T_g}+\left(\frac{1}{i\omega\tau_p}-\epsilon z\right)\frac{u'_p}{D}=0 \tag{2.69}$$

Here,

$$\epsilon_2 = \epsilon + \frac{\rho_g}{\rho_p} = \epsilon + \eta \tag{2.70}$$

Note that the δ appearing in the gas momentum equations results from keeping the second term in the gas continuity equation. The η appearing in ϵ_2 results from keeping the gas partial pressure term in the particle momentum equation. Due to an order of magnitude analysis the following terms were neglected: $\alpha\delta,\ \epsilon_2\delta,\ \alpha\epsilon,\ \delta\eta$.

Equation 2.69 is used to obtain the perturbation velocity for particles as:

$$\frac{u'_p}{D} = \frac{1-\epsilon_2 zt}{1-t-\epsilon t}\frac{u'_g}{D} - \frac{\epsilon_2 zt}{1-t-\epsilon t}\frac{T'_g}{T_g} \tag{2.71}$$

$$t = i\omega\tau_p \tag{2.72}$$

The last term in Equation 2.68 involving the particles velocity can now be written as:

$$\left[\frac{B}{t}-\alpha-\delta z\right]\frac{u'_p}{D} = \frac{[B-t(\alpha+\delta z+B\epsilon_2)]}{t(1-t-\epsilon t)}\frac{u'_g}{D} - \frac{\epsilon_2 zB}{(1-t-\epsilon t)}\frac{T'_g}{T_g} \tag{2.73}$$

Therefore, Equation 2.68 can now be rewritten as:

$$\left(\frac{u_g'}{D}\right)\left[1-z(1-\alpha)+\frac{(B\epsilon+B-\alpha-z\delta-z\epsilon_2 B)}{(1-t-\epsilon t)}\right]-z\left[1+\frac{B\epsilon_2-\alpha+\alpha t}{1-t-\epsilon t}\right]\frac{T_g'}{T_g}=0 \quad (2.74)$$

simplyfing,

$$\left(\frac{u_g'}{D}\right)\left[1-z\left\{1+\frac{\delta+\epsilon_2 B-\alpha+\alpha t}{1-t-\epsilon t}\right\}+\frac{B+B\epsilon-\alpha}{1-t-\epsilon t}\right] - z\left[\frac{1+B\epsilon_2-\alpha+\alpha t}{1-t-\epsilon t}\frac{T_g'}{T_g}\right]=0 \quad (2.75)$$

If we neglect the added mass for term $C_M=\epsilon=\alpha=0$, and above equation becomes

$$\left(\frac{u_g'}{D}\right)\left[1-zx_1+\frac{Bx_2}{(1-t)}\right]-zx_3\frac{T_g'}{T_g}=0 \quad (2.76)$$

Where,

$$x_1=1+\frac{2\delta}{1-t-\epsilon t}, \quad (2.77)$$

$$x_3=1+\frac{\delta}{1-t}. \quad (2.78)$$

Then, the particles thermal energy Equation 2.66 is used to replace T_p' in the gas energy Equation 2.59 to obtain:

$$\frac{u_g'}{D}(\gamma-1)-\frac{T_g'}{T_g}\left(1+\frac{B_2}{1-i\tau_\theta\omega}\right)=0 \quad (2.79)$$

The gas equations are now reduced to

$$\left(\frac{u_g'}{D}\right)\left[1-zx_1+\frac{B}{(1-t)}\right]-zx_3\frac{T_g'}{T_g}=0 \quad (2.80)$$

$$\frac{u_g'}{D}(\gamma-1)-\frac{T_g'}{T_g}\left(1+\frac{B_2}{1-i\tau_\theta\omega}\right)=0 \tag{2.81}$$

Equations 2.80 and 2.81 forms a system of two coupled equations, in the form $Ax=0$

$$\underbrace{\begin{pmatrix} 1-z\,x_1+\dfrac{B\,x_2}{1-t} & -z\,x_3 \\ \gamma-1 & -\left(1+\dfrac{B_2}{1-i\,\tau_\theta\omega}\right)\end{pmatrix}}_{\mathbf{A}}\underbrace{\begin{pmatrix}\frac{u_g'}{D}\\ \frac{T_g'}{T_g}\end{pmatrix}}_{\mathbf{x}}=\mathbf{0}$$

These equations will produce non-zero solution only if the determinant is zero, thus the condition is given as:

$$\left(\frac{ak}{\omega}\right)^2\left(x_3+\frac{x_1-x_3}{\gamma}+x_1\frac{C_{pp}}{C_p}\frac{B}{1-i\tau_\theta\omega}\right)=\left(1+\frac{B}{1-t}\right)\left(1+\frac{\gamma C_{pp}}{C_p}\frac{B}{1-i\tau_\theta\omega}\right) \tag{2.82}$$

The final equation for the non-Dimensional complex wave number k_i^+ is given by

$$\begin{aligned}(k^+)^2\left(1+\frac{\delta}{1-i\Omega}+\frac{\delta}{\gamma(1-i\Omega)}+\left(1+\frac{2\delta}{1-i\Omega}\right)\frac{C_{pp}}{C_p}\frac{B}{1-i\tau_\theta\omega}\right)\\ =\left(1+\frac{B}{1-i\Omega}\right)\left(1+\frac{\gamma C_{pp}}{C_p}\frac{B}{1-i\tau_\theta\omega}\right)\end{aligned} \tag{2.83}$$

Where,

$$\Omega=\omega\tau_p=\omega\frac{\rho_p}{\rho_g}\frac{d_p^2}{18\,\nu_g} \tag{2.84}$$

$$k^+=k_r^+ + k_i^+=\frac{a}{\omega}(k_r+ik_i), \tag{2.85}$$

Since the acoustic perturbation amplitude varies as $e^{-k_i^+ r}$, k^+ represent the non dimensional complex wave number and the imaginary component k_i^+ represents the attenuation rate of the wave. The dimensionless frequency Ω quantifies the degree of coupling between the acoustic field and the particle inertia.

This formulation can be regarded as an extension of the classical analysis for dilute suspensions. Dobbin and Temkin[29] studied the sound transmission in air-aluminum mixture

and they neglected the first order terms in δ. If δ is neglected in Equation 2.83, the present formulation reduces to that of Dobbins and Temkin[29] Equation 12. Notice that Dobbins and Temkin did not account for the finite volume occupied by the particles. In contrast, the present model explicitly included the volume fractions of both the gas phase and the particle phase, thereby capturing the effects of finite spatial particle occupancy, making it more suitable for moderately loaded suspensions where the volume occupied by the phase is not negligible.

For air and water droplets:

$$\frac{C_{pp}}{C_p} = 4.185;\ \gamma = 1.4;\ \frac{\rho_p}{\rho_g} = 816;\quad Pr = 0.7, \tag{2.86}$$

$$\tau_\theta = \frac{3}{2}\frac{C_{pp}}{C_p} Pr\, \tau_p = 4.4\, \tau_p;\ \omega\tau_\theta = 4.4\, \Omega. \tag{2.87}$$

Substituting these values into Equation 2.83 yields the following expression for an air–water mixture:

$$\begin{aligned}(k^+)^2\left(1 + \frac{\delta}{1 - i\Omega} + \frac{\delta}{1.4\,(1 - i\Omega)} + \left(1 + \frac{2\delta}{1 - i\Omega}\right)\frac{3957\,\delta}{1 - 4.4\,i\Omega}\right) \\ = \left(1 + \frac{816\,\delta}{1 - i\Omega}\right)\left(1 + \frac{5540\,\delta}{1 - 4.4\,i\Omega}\right).\end{aligned} \tag{2.88}$$

2.3.2 Effect of Volume of fraction

Considered here is the influence of δ on acoustic attenuation. Figure 2.3 shows that attenuation, represented by k_i^+, increases with increasing water volume fraction. This indicates that a higher concentration of droplets enhances momentum and thermal coupling between phases, leading to greater acoustic energy dissipation. Physically, as δ increases, the effective inertia of the two-phase medium rises, amplifying viscous and thermal damping effects.

It should be noted that the present analysis is valid only for dispersed or moderately loaded mixtures, where the droplet phase does not form a continuous layer.

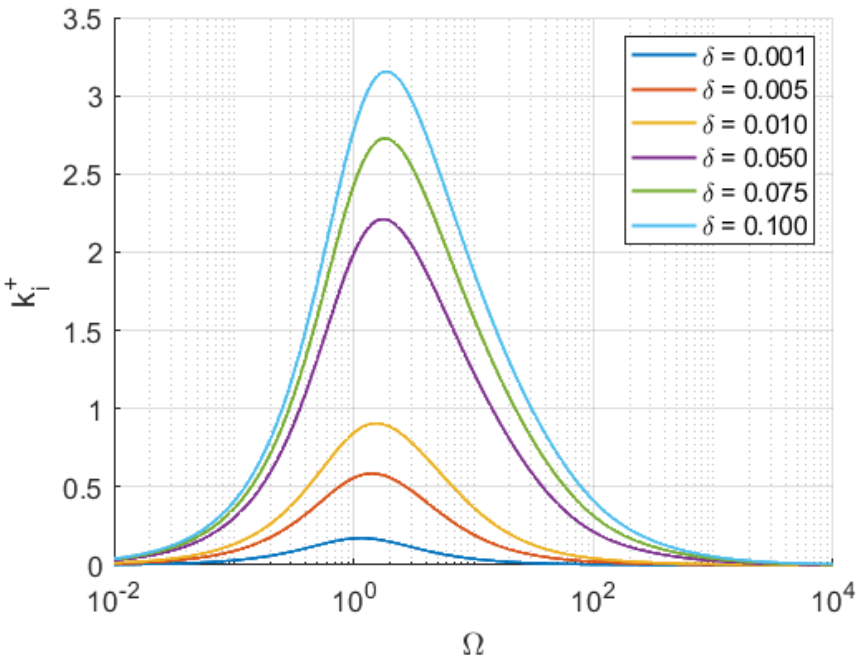

Figure 2.3 Effect of the dimensionless frequency Ω on the reduction factor, k_i^+ for various water volume of fraction δ.

2.3.3 Numerical Solution of the Suspended Particle Case

In addition to the asymptotic solution above, the numerical solution for the perturbation equations given in Equations 2.38-2.43 is obtained as follows: The equations are written as an algebraic homogeneous system of equations of the form:

$$A(k) \cdot X = 0 \tag{2.89}$$

In this formulation, X is the vector that collects the perturbation variables for both phases and the entries for matrix A depend linearly on the complex wavenumber k. Since the matrix A depends linearly on k, it can be decomposed as:

$$A(k) = A_1 + kA_2 \tag{2.90}$$

This decomposition allows the homogeneous system to be rewritten in the form:

$$A_1 \cdot X = -k \cdot A_2 \tag{2.91}$$

This formulation defines a generalized eigenvalue problem for the complex wavenumber k, whose real part determines the phase propagation and whose imaginary part governs attenuation. The eigenvalues are obtained using MATLAB's generalized eigenvalue solver, which employs the QZ (generalized Schur) algorithm from the LAPACK library.

The comparison between the asymptotic and the numerical solutions is presented in Figure 2.4 in which it can be seen that the analytical solution fits better with the numerical results for volume fraction values near to 0.1. The discrepancies observed between the asymptotic and numerical solutions can be attributed to the simplifying assumptions adopted in the derivation of the analytical model in which several higher-order terms were neglected. While this approximation significantly simplifies the mathematical treatment and yields closed-form expressions that capture the dominant physical behavior, it introduces a systematic deviation from the full solution of the linearized system, in which all terms are retained, specially for small values of δ.

2.3.4 Acoustic Scattering by Spherical Droplets

Acoustic scattering refers to the redirection and redistribution of an incident sound wave when it encounters an obstacle or inhomogeneity whose acoustic impedance differs from that of the surrounding medium. When a propagating wave interacts with particles in a host fluid, part of the incident energy is re-emitted in different directions, part is absorbed within the inclusion, and part continues to propagate as a modified transmitted wave. This process alters both the amplitude and phase of the acoustic field and, when many scatterers are present, leads to an overall attenuation and diffusion of sound energy throughout the medium. In the context of the present study, scattering is of particular interest because an air–water droplet curtain acts as a multiphase region where many droplets serve as individual

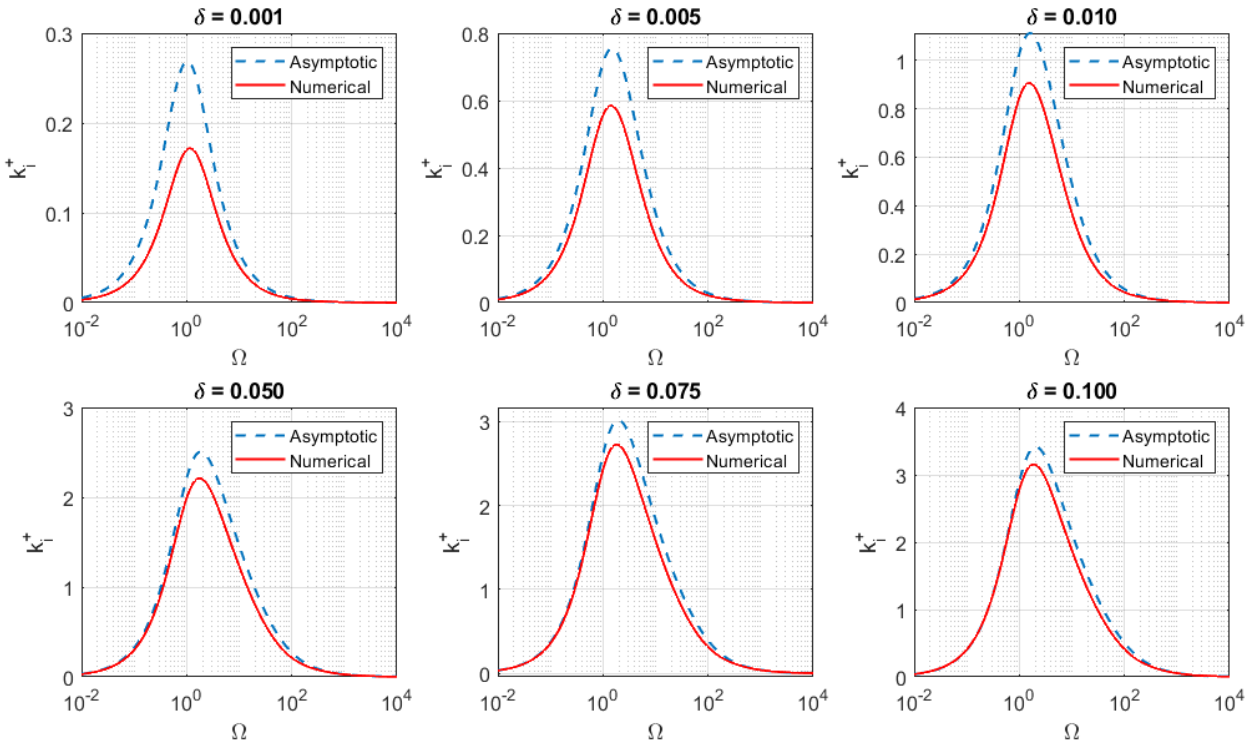

Figure 2.4 Comparison of asymptotic and numerical solutions for the reduction factor k_i^+ for various δ.

scatterers and the resulting attenuation depends on the size, material density and spatial concentration of the droplets.

For analytical convenience and to capture the most general behavior, the scattering generated by a dispersed droplet field is represented through the interaction between an incident acoustic wave and a single, isolated spherical particle. This spherical approximation reduces the complexity of the scattered-field formulation while retaining the fundamental physics of wave–particle interaction, thereby yielding "idealized" theoretical predictions [37].

To quantify the scattering produced by an individual sphere, the key parameter of interest is the total scattering cross section σ_{scat}, defined as the equivalent area of a particle that would intercept the same amount of incident acoustic power as that redistributed by scattering [37]. Its magnitude depends on the contrast of acoustic impedance between the droplet and the surrounding medium, and therefore it can exceed or fall below the geometric area πr_p^2, where r_p represent the particle ratio. The scattering behavior is governed primarily by three

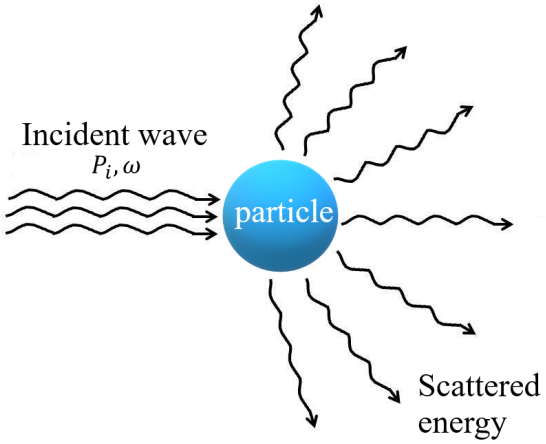

Figure 2.5 Schematic representation of acoustic scattering by a spherical particle. Here, P_i and ω represents the amplitude and the angular frequency of the incident wave, respectively.

nondimensional parameters: the acoustic radius $kr_p = k_0 r_p$, the density ratio $g = \rho_p/\rho_f$, and the sound-speed ratio $h = c_p/c_f$, where subscripts p and f refer to the particle and the host fluid, respectively.

As shown schematically in Figure 2.5, acoustic energy travels through the medium as a pressure wave of amplitude P_i and angular frequency ω. Following Sullivan [37], When this wave encounters a spherical inclusion, it induces both an internal oscillation within the droplet and a scattered pressure field radiating outward. For a plane incident wave, the total acoustic pressure field can be expressed as the superposition of incident and scattered components:

$$P(r,\theta) = P_{\text{inc}}(r,\theta) + P_{\text{sc}}(r,\theta), \tag{2.92}$$

with

$$P_{\text{inc}}(r,\theta) = P_i \sum_{l=0}^{\infty} (2l+1) i^l j_l(k_0 r) P_l(\cos\theta) \tag{2.93}$$

$$P_{\text{sc}}(r,\theta) = P_i \sum_{l=0}^{\infty} (2l+1) i^l a_l \, h_l^{(1)}(k_0 r) P_l(\cos\theta), \tag{2.94}$$

where j_l and $h_l^{(1)}$ are the spherical Bessel and Hankel functions, and P_l are the Legendre polynomials. The complex coefficients a_l are obtained by enforcing continuity of pressure

and radial velocity at the sphere surface $r = a$:

$$a_l = -\frac{j_l'(k_p a) j_l(k_0 a) - gh\, j_l(k_p a) j_l'(k_0 a)}{j_l'(k_p a) h_l^{(1)}(k_0 a) - gh\, j_l(k_p a) h_l^{(1)'}(k_0 a)}, \qquad g = \frac{\rho_p}{\rho_f}, \quad h = \frac{c_p}{c_f}. \tag{2.95}$$

The total scattering cross section σ_{scat} quantifies the total scattered power per unit incident intensity and is defined as:

$$\sigma_{\text{scat}} = \frac{4\pi}{k_0^2} \sum_{l=0}^{\infty} (2l+1)|a_l|^2. \tag{2.96}$$

In a suspension containing a droplet volume fraction ϕ_p, it becomes necessary to relate the acoustic energy scattered by a single sphere to the cumulative attenuation produced by all particles in the mixture. To establish this connection, we apply here the Beer–Lambert law, which describes the exponential decay of acoustic intensity I as a wave propagates through a medium containing N scattering particles per unit volume.

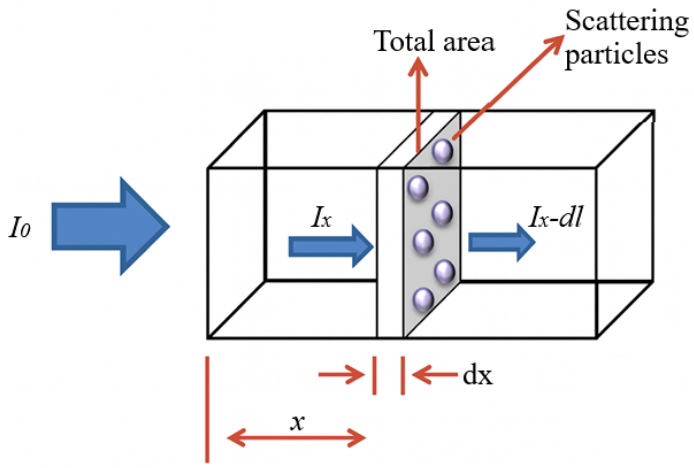

Figure 2.6 Schematic representation of acoustic intensity attenuation in a suspension of scattering particles.

The differential form of the Beer–Lambert law is expressed as:

$$\frac{dI}{dx} = -I\, N \sigma_{\text{scat}}, \tag{2.97}$$

where σ_{scat} is the total scattering cross section of a single droplet. Integrating Equation

2.97 along the propagation distance x yields the intensity decay law for the mixture, as shown below.

$$I(x) = I_0 e^{(-N\sigma_{\text{scat}}x)}. \tag{2.98}$$

Here, I_0 is the incident intensity. Now, For a plane acoustic wave, the instantaneous acoustic intensity in a fluid is related to the pressure amplitude by:

$$I = \frac{|p|^2}{2\rho c}. \tag{2.99}$$

where ρ and c denote the density and sound speed of the medium, respectively. Assuming that the acoustic pressure perturbation propagates according to:

$$p'(z) \sim e^{i(k_r + ik_i)x} \tag{2.100}$$

Comparing Equations 2.99 and 2.100, we could state that the intensity is proportional to the square of the amplitude of the acoustic pressure.

$$I \sim |p|^2 \sim e^{-2k_i x}, \tag{2.101}$$

Showing that the intensity decays exponentially with a rate determined by the imaginary part of the complex wavenumber, k_i. By comparing the exponential decay laws obtained from the Beer–Lambert formulation and the acoustic wave representation, we identify the equivalence between both attenuation mechanisms, leading to:

$$2k_i = N\sigma_{scat}. \tag{2.102}$$

This relation links the macroscopic attenuation coefficient k_i of the suspension to the microscopic scattering properties of individual droplets, providing the theoretical bridge between single-particle scattering and the collective noise-reduction behavior of the multiphase

medium. Following Crowe et al. [34], the number density for spherical particles can be expressed in terms of the droplet volume fraction ϕ_p as:

$$N = \frac{\phi_p}{\frac{4}{3}\pi r_p^3}. \tag{2.103}$$

Substituting this expression into Equation 2.102, yields the following expression for the imaginary part of the complex wavenumber as a function of ϕ_p and σ_{scat} as:

$$k_i = \frac{3\phi}{8\pi r_p^3}\,\sigma_{scat} \tag{2.104}$$

Finally, the reduction factork_i^+ is obtained as presented in the previous section.

$$k_i^+ = \frac{c_f k_i}{\omega} \tag{2.105}$$

Figure 2.7 shows the variation of the reduction factor k_i^+ with nondimensional frequency Ω for several values of the droplet volume fraction ϕ_p. As expected, increasing ϕ_p results in a proportional increase in the magnitude of k_i^+, since the number density of scatterers is directly proportional to ϕ_p.

It is noteworthy that the magnitudes of k_i^+ predicted by the scattering formulation are approximately one order of magnitude smaller than those obtained from the solution of the perturbation multiphase equations. This comparison indicates that the attenuation due solely to scattering by droplets is relatively small compared to that produced by interphase momentum and energy exchange mechanisms. Therefore, in the analysis presented in the following sections, the contribution of scattering to the overall noise reduction is neglected.

2.3.5 Application of Suspended Case to Jet Noise Reduction

In the present work, the background flow is assumed to originate from a turbulent jet emerging into a quiescent ambient fluid. Here, the only source of momentum is the jet itself,

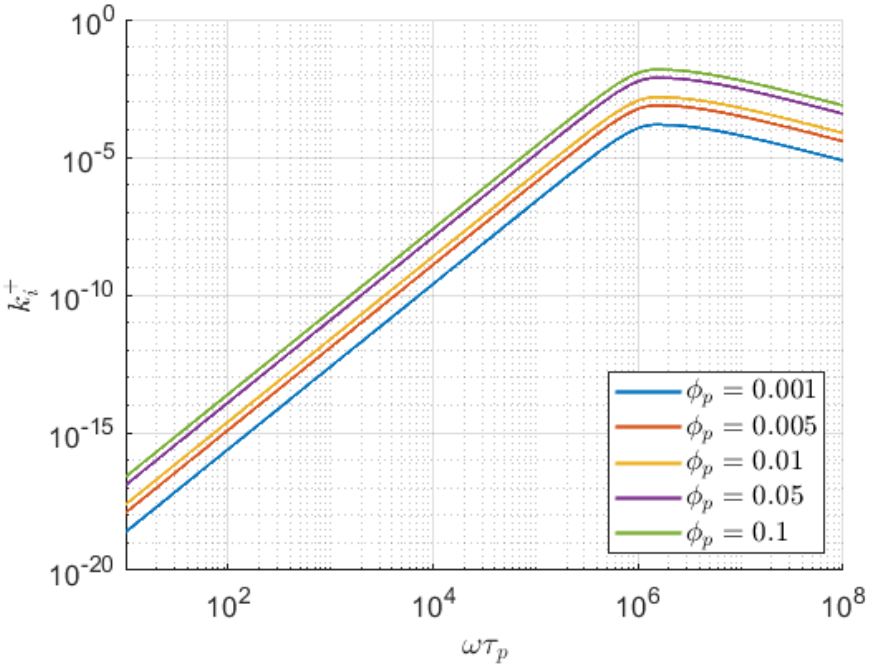

Figure 2.7 Reduction factor k_i^+ from particle scattering as a function of non dimensional frequency Ω for various droplet volume fractions ϕ_p. here $d_p = 5 \cdot 10^{-4}$m.

and in the absence of external forces, the momentum flux within the jet cross-section remains conserved downstream of the jet source. In the suspended particle case here, we assume that the curtain is far enough from the jet such that it is not affected by the ambient wind flow created by the jet.

2.3.6 Estimation Effect of Droplet Size for Noise Reduction

Following the numerical solution of the perturbation equations, the nondimensional frequency Ω can be expressed in terms of the Reynolds number R_j, the Strouhal number St, and the jet-nozzle diameter D_j. We begin by introducing the definition of the Strouhal number,

$$St = \frac{f D_j}{U_j}, \tag{2.106}$$

where U_j denotes the jet mean velocity. The corresponding angular frequency of the imposed perturbation is given by:

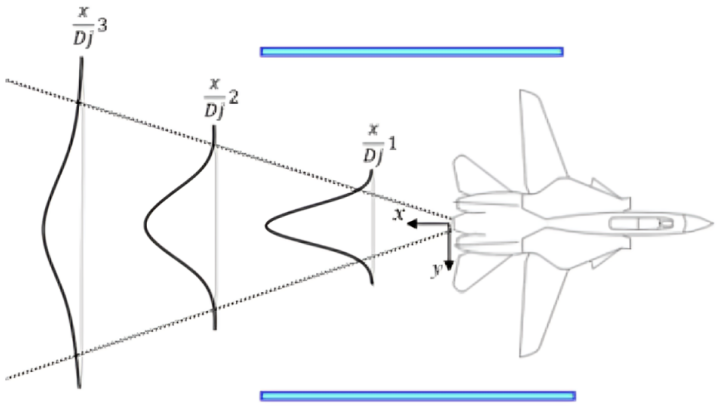

Figure 2.8 Schematic representation of the background jet flow field into a quiescent ambient fluid.

$$\omega = 2\pi f = (2\pi St)\,\frac{U_j}{D_j}. \tag{2.107}$$

To incorporate the particle size into the nondimensionalization, we rewrite the particle diameter as:

$$d_p^2 = \left(\frac{d_p}{D_j}\right)^2 D_j^2. \tag{2.108}$$

Substituting these relations into the definition of the nondimensional frequency $\Omega = \omega\tau_p$, where the particle relaxation time is given by:

$$\tau_p = \frac{\rho_p d_p^2}{18\,\rho_g \nu_g}, \tag{2.109}$$

yields

$$\Omega = \frac{1}{18\nu_g}\left(\frac{d_p}{D_j}\right)^2 D_j^2 \frac{\rho_p}{\rho_g}\left(2\pi St\,\frac{U_j}{D_j}\right). \tag{2.110}$$

Simplifying the expression above gives the following:

$$\Omega = \frac{1}{18\nu_g \eta}\left(\frac{d_p}{D_j}\right)^2 (2\pi St)\,U_j D_j, \tag{2.111}$$

where $\eta = \rho_g/\rho_p$ is the density ratio. Recognizing that $R_j = U_j D_j/\nu_g$, the final expression

becomes

$$\Omega = \frac{1}{18\eta}\left(\frac{d_p}{D_j}\right)^2 (2\pi St)\, R_j. \tag{2.112}$$

In Figure 2.9, the reduction coefficient is plotted versus the dimensionless particle size, where $St = 0.5$ and $Re_j = 10^5$ are assumed. These results shows that, for the values of δ studied there is an optimum droplet size for maximizing the reduction effect that varies between 0.0002 and 0.0003 of the jet diameter.These results suggest that if the droplets are too small, they tend to behave like tracers with negligible attenuation. Conversely, if the droplets are too large, they exhibit substantial inertia, rendering them unable to effectively respond to acoustic oscillations, which also results in diminished attenuation.

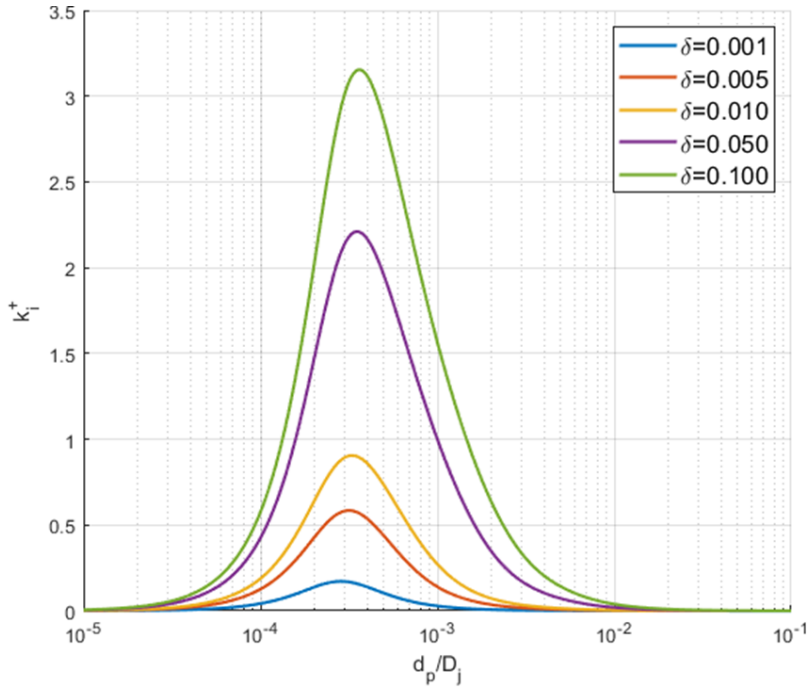

Figure 2.9 Effect of the droplet size on the reduction factor, St=0.5, $R_j = 10^5$.

2.3.7 Estimation of Sound Level Reduction for a Jet

Assuming that the location of the mixture front is far from the jet, the decay of the acoustic amplitude along the propagation direction can be expressed as a function of the

distance travel across the mixture by the perturbation ξ as follows

$$A(\xi) = A_0 e^{-k_i \xi}, \tag{2.113}$$

where k_i is the imaginary part of the wavenumber, associated with the spatial attenuation of the perturbation (wave) and A_0 denotes the reference (or initial) amplitude at $\xi = 0$. The corresponding reduction in sound pressure level is obtained from the standard definition.

$$dB = 20 \log_{10}\left(\frac{A_0}{A(\xi)}\right) = 20 \log_{10}\left(e^{k_i \xi}\right) = 8.686\, k_i\, \xi, \tag{2.114}$$

Now, we introduce the non-dimensional distance travelled across the mixture as:

$$\xi^+ = \frac{\xi}{D_j}, \tag{2.115}$$

According to Equation 2.85 the imaginary part of the complex wave number is define as $k_i = \frac{w}{a} k_i^+$, therefore, the reduction per unit non-dimensional distance becomes:

$$\frac{dB}{\xi^+} = 8.686\, D_j\, \frac{\omega}{a} k_i^+. \tag{2.116}$$

To express the result in terms of flow parameters, the Strouhal number is introduced following Equation 2.106 and the final expression for the normalized noise reduction is given by:

$$\frac{dB}{\xi^+} = 8.686\, (2\pi)\, St\, M_j\, k_i^+, \tag{2.117}$$

Which provides a direct estimate of the sound level reduction in terms of frequency, jet operating conditions, and the normalized attenuation coefficient. If we assume the Mach number of the jet $M_j = 1$ and the peak noise at $St = 0.5$, then:

$$\frac{DB}{\xi^+} = 27.3\, k_i^+ \tag{2.118}$$

Figure 2.10 shows that for a fixed particle size, the decibel reduction consistently increases with increasing δ. This behavior indicates the existence of an optimal particle size range that maximizes acoustic attenuation, as was indicated previously in Figure 2.9.

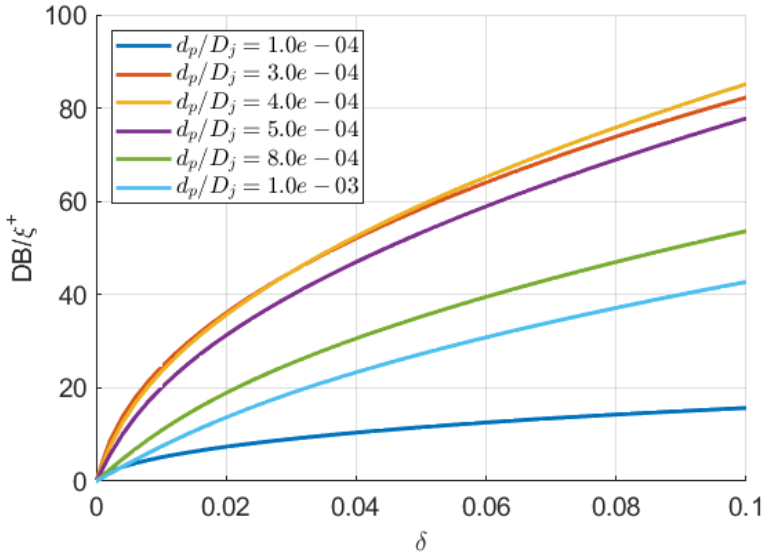

Figure 2.10 Estimated Decibels Reduction for a Jet with Mach number M_j =1, Reynolds number $R_j = 10^5$ with peak noise at St=0.5.

We note that if the mixture thickness is $\xi^+ = 0.01$ or 0.1, and the normalized decibel reduction is 60, then the decibel reduction is 0.6 or 6, respectively.

2.3.8 Dependency on the Strouhal Number

With

$$\frac{d_p}{D_j} = 4 \cdot 10^{-4}, \quad R_j = 10^5, \quad M_j = 1, \tag{2.119}$$

$$\frac{DB}{\xi^+} = 8.686\,(2\pi) St\, M_j\, k_i^+ = 54.58\, St\, k_i^+. \tag{2.120}$$

Figure 2.11 illustrates that the noise reduction increases with St following a nonlinear

trend and tends to saturate toward an asymptotic value at sufficiently high St for each given δ. However, note that the actual jet Strouhal number for peak noise is of order one. Similar trends of noise reduction with respect to the frequency can be appreciated in Bohne *et al.*[38], Mahanta and Vajpayee[7], and Herrero *et al.*[33].

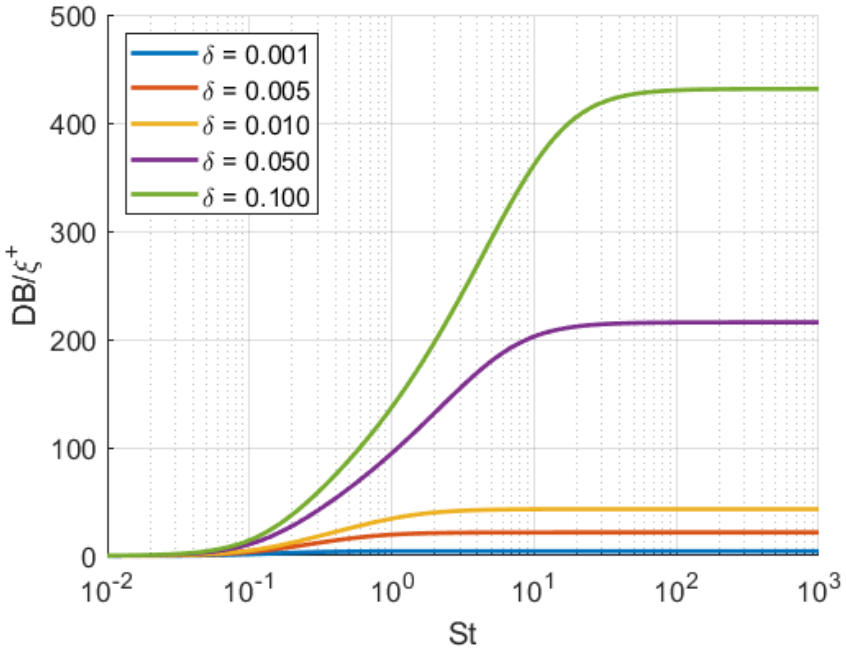

Figure 2.11 Dependency of the noise reduction on the Strouhal number for various water volume of fraction.

2.4 Comparison of Numerical Result of the Suspended Equations With Experimental Results

The attenuation of sound by warm air fog as a function of dimensionless frequency and liquid fraction was measured by Dobbins and Cole [30]. Following the normalized reduction factor presented in Dobbin and Temkin [29] in Equation(17), Figure 2.12 presents a comparison between the experimental data, the asymptotic model, and the numerical results developed in the current work. The asymptotic solution slightly over predicts the maximum attenuation compared to the measurements, while the numerical approach provides a closer agreement with the experimental values near the peak region.The difference between the

experimental results and those obtained in the present study arises from additional dissipative mechanisms neglected in the current formulation. As demonstrate by Cole and Dobbins [39], and Kandula [32], transpiration and condensation processes has an appreciable effect on sound attenuation and dispersion at low and high droplet concentrations. Atmospheric fog should therefore be modeled as a three-phase mixture consisting of non condensing gas, saturated vapor, and liquid droplets, where interphase mass transfer between phases introduces an additional relaxation process. When such mass transfer is included, the droplet energy equation departs from the classical single-phase relaxation form and becomes coupled to the simultaneous effects of heat and mass exchange, leading to a more complex attenuation behavior[39].

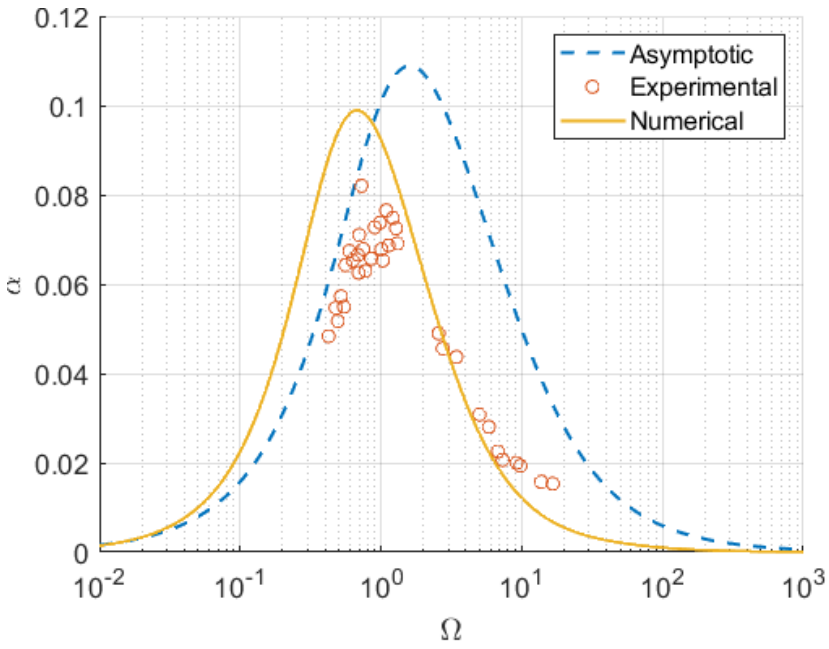

Figure 2.12 Comparison of Asymptotic, Numerical, and Experimental Attenuation Results. Here $\alpha = \frac{k_i^+}{\delta}\eta$.

The propagation of acoustic waves and the associated energy absorption in an air–water droplet medium considering different parameters such as flow ratio, mass fraction, atomization pressure, and droplet material was experimentally investigated by Mahanta and Vajpayee [7]. Figure 2.13 presents their measurements of normalized noise reduction as

a function of perturbation frequency for several values of the mass fraction (MR), defined as the ratio of the liquid mass to the mass of air within a given volume of the medium. Following Temkin [40], the mass fraction can be related to the particle volume of fraction ϕ_g, as expressed in Equation 2.121. Using this relation, the numerical predictions of normalized noise reduction were obtained from Equation 2.120 by employing the experimental values of ϕ_g and assuming a particle diameter of 3×10^{-4} m. These results are presented in Figure 2.14 as a comparison with the experimental data.

$$\phi_g = \frac{MR\left(\frac{\rho_g}{\rho_p}\right)}{1 + MR\left(\frac{\rho_g}{\rho_p}\right)}. \tag{2.121}$$

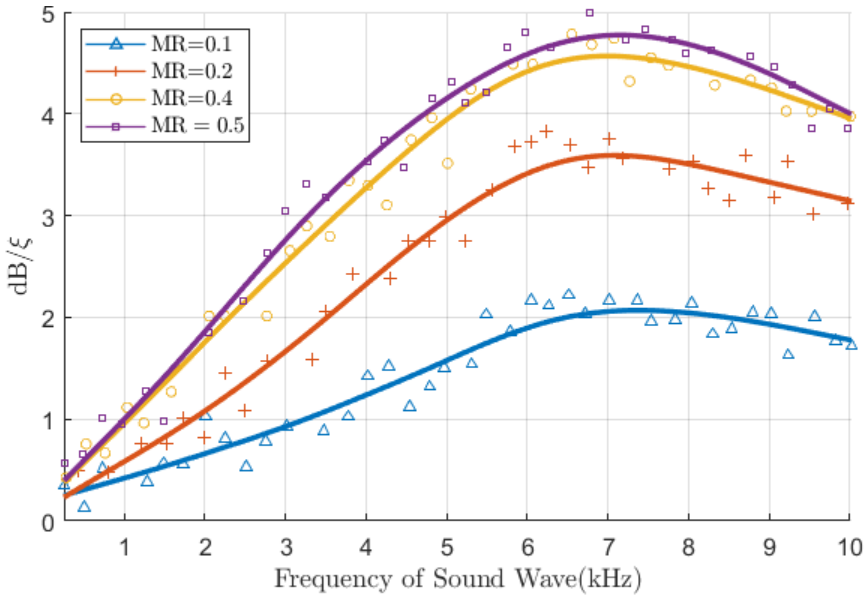

Figure 2.13 Experimental measurements of normalized noise reduction as a function of frequency for different mass fractions. Adapted from Mahanta and Vajpayee [7].

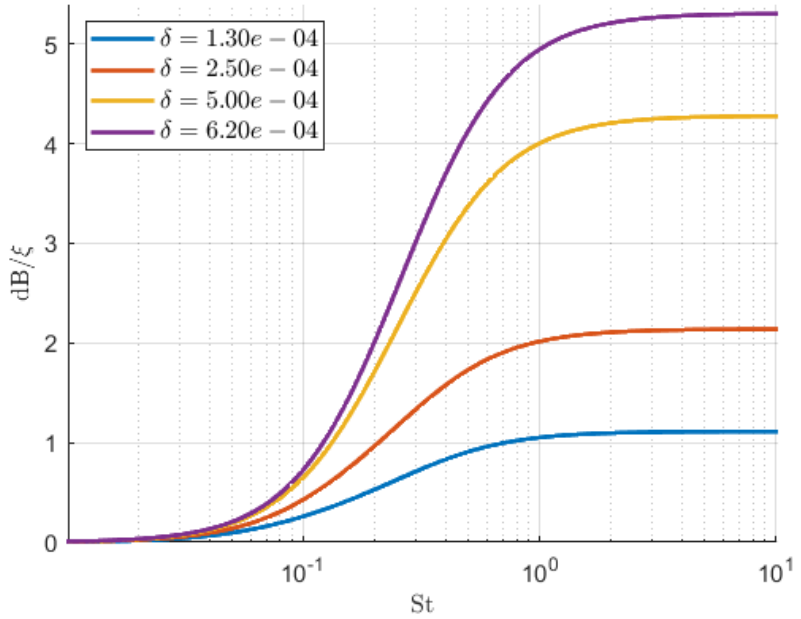

Figure 2.14 Numerical predictions of normalized noise reduction as a function of Strouhal number for equivalent particle volume fractions. $d_p = 3 \times 10^{-4}$ m.

Experimental results, Figure 2.13, and the numerical predictions obtained in the present study, Figure 2.14, reveals consistent qualitative trends in the normalized noise reduction. In both cases, the attenuation increases with increasing frequency (or Strouhal number) up to a certain value, and higher mass fractions (or equivalently, larger particle volume fractions) yield stronger attenuation. This agreement confirms that the analytical model captures the fundamental dependence of acoustic energy absorption on particle concentration. However, key differences arise at high frequencies. In the experimental data, the noise reduction rises to a maximum and then decreases, whereas the numerical predictions show a monotonic saturation toward an asymptotic value. This discrepancy likely stems from the simplifying assumptions in the analytical formulation and from uncontrolled experimental parameters. As reported by Mahanta and Vajpayee [7] "the droplet size is dictated by the air pressure" but no detailed characterization of the resulting flow properties was provided. In practice, real sprays exhibit a polydisperse droplet size distribution, which broadens and lowers the attenuation peak. As shown in Figure 2.10, variations in particle diameter significantly modify the noise reduction even for the same volume fraction. Because the present model assumes

monodisperse droplets, the post-peak decay observed experimentally is not reproduced.

Moreover, Figure 2.13 shows that the decay in noise reduction is more pronounced for higher mass ratios. This behavior may be explained by the findings of Mahanta and Vajpayee[7], who noted that increasing the atomization pressure raises the local droplet concentration but simultaneously promotes condensation of the liquid phase, an effect not accounted for in the present model. Finally, their experimental configuration exhibited a nonuniform droplet concentration along the test section, with higher values near the inlet and lower values toward the outlet. Such spatial gradients introduce geometry-dependent attenuation effects that may further explain the decline observed at high frequencies.

2.5 Computational Fluid Dynamics Simulations for the Suspended Case

The information presented in the following section was adapted from ANSYS Fluent Theory Guide,2025 R1. For the numerical simulation of the suspended particle configuration, the Eulerian + Dense Discrete Phase Model (DDPM) formulation available in the software ANSYS Fluent 2025 R1 is adopted. This hybrid approach combines an Eulerian treatment of the carrier phase (air) with a Lagrangian description of the dispersed phase (droplets). It is particularly suitable for gas–liquid or particle–laden flows where the dispersed volume fraction is not negligible but remains below the packing limit, typically $\alpha_p < 0.1$. In such regimes, the classical Discrete Phase Model (DPM) becomes inaccurate because it neglects the finite particle volume fraction when assembling the continuous-phase equations. The DDPM extends the Lagrangian framework to account for this limitation by coupling the particle volume fraction and momentum exchange directly into the carrier-phase conservation equations.

In the Eulerian description, each phase is treated as an interpenetrating continuum, and the local phase volume fractions ϕ_q satisfy the following equation:

$$\sum_{q=1}^{n_{\text{phases}}} \phi_q = 1. \tag{2.122}$$

The mass and momentum conservation equations for the carrier (continuous) phase p are given by extending the standard single-phase equations to include the effect of the discrete phase, following:

$$\frac{\partial}{\partial t}(\phi_p \rho_p) + \nabla \cdot (\phi_p \rho_p \mathbf{u}_p) = \sum_{q=1}^{n_{\text{phases}}} (\dot{m}_{pq} - \dot{m}_{qp}), \tag{2.123}$$

On the right-hand side, the summation term $\sum_{q=1}^{n_{\text{phases}}}(\dot{m}_{pq} - \dot{m}_{qp})$ represents the net rate of mass exchange between phase p and all other phases q.

$$\begin{aligned} &\frac{\partial}{\partial t}(\phi_p \rho_p \mathbf{u}_p) + \nabla \cdot (\phi_p \rho_p \mathbf{u}_p \mathbf{u}_p) \\ &= -\phi_p \nabla p + \nabla \cdot \left[\phi_p \mu_p \left(\nabla \mathbf{u}_p + (\nabla \mathbf{u}_p)^T\right)\right] \\ &+\phi_p \rho_p \mathbf{g} + \sum_{q=1}^{n_{\text{phases}}} (\mathbf{K}_{pq}(\mathbf{u}_q - \mathbf{u}_p) + \dot{m}_{pq}\mathbf{u}_q - \dot{m}_{qp}\mathbf{u}_p) + \mathbf{S}_{DPM}^{\text{explicit}}. \end{aligned} \tag{2.124}$$

The right-hand side terms represent, respectively, the principal forces acting on the carrier phase. The first term, $-\phi_p \nabla p$, corresponds to the pressure-gradient force acting on phase p, weighted by its volume fraction. The second term, $\nabla \cdot [\phi_p \mu_p (\nabla \mathbf{v}_p + (\nabla \mathbf{v}_p)^T)]$, accounts for viscous stresses due to molecular and turbulent diffusion. The third term, $\phi_p \rho_p \mathbf{g}$, represents the gravitational body force. The summation term introduces interphase coupling: $\mathbf{K}_{pq}(\mathbf{v}_q - \mathbf{v}_p)$ describes the momentum exchange due to velocity slip between phases, where $\mathbf{K}_{pq}$ is the interphase drag coefficient that depends on local flow conditions and particle Reynolds number. The subsequent terms, $\dot{m}_{pq}\mathbf{v}_q - \dot{m}_{qp}\mathbf{v}_p$, account for the momentum carried by any interphase mass transfer, such as that arising from evaporation or condensation. Finally, $\mathbf{S}_{DPM}^{\text{explicit}}$ represents explicit momentum source contributions from the discrete phase, including user-defined or non-implicitly coupled effects.

For energy transport, the DDPM modifies the carrier-phase enthalpy equation to include

heat exchange with the Lagrangian phase as:

$$\frac{\partial}{\partial t}\left[\phi_p \rho_p \left(e_p + \tfrac{1}{2}|\mathbf{u}_p|^2\right)\right] + \nabla \cdot \left[\phi_p \rho_p \mathbf{u}_p \left(h_p + \tfrac{1}{2}|\mathbf{u}_p|^2\right)\right] = H_{\text{conv}} + H_{\text{diff}} + H_{\text{visc}} + H_{\text{user}} + p\frac{\partial \phi_p}{\partial t} + \sum_{q=1}^{n_{\text{phases}}} (Q_{pq} + \dot{m}_{pq} h_{pq} - \dot{m}_{qp} h_{qp}) + Q_{DPM} + S_{DPM}^{\text{explicit}}. \tag{2.125}$$

The terms on the right-hand side describe the various modes of energy transfer. The quantities H_{conv}, H_{diff}, and H_{visc} represent, respectively, the convective transport of enthalpy, diffusive conduction through molecular and turbulent processes, and heat generation due to viscous dissipation. The term H_{user} allows for any user-specified volumetric heat source, while $p(\partial \phi_p/\partial t)$ accounts for the mechanical work performed by pressure during changes in the local phase volume fraction. The summation term, $\sum_{q=1}^{n_{\text{phases}}}(Q_{pq} + \dot{m}_{pq} h_{pq} - \dot{m}_{qp} h_{qp})$, represents interphase thermal coupling: Q_{pq} is the direct conductive or convective heat transfer between phases, and the mass-transfer terms describe the enthalpy flux carried by material exchanged between phases. The additional contributions Q_{DPM} and $S_{DPM}^{\text{explicit}}$ denote, respectively, the total heat exchanged between the continuous phase and the Lagrangian parcels, and any explicit energy sources defined within the discrete-phase model.

In FLUENT, the Lagrangian formulation does not track every individual particle. Instead, the solver groups many identical physical particles into a single computational entity known as a *parcel*. Each parcel therefore represents a statistically large number of real particles that share the same physical attributes (diameter, density, specific heat, and temperature) and are assumed to experience identical local flow conditions. The number of real particles represented by a parcel is defined by its mass flow rate and cloud parameters, and this quantity remains constant throughout the trajectory unless phase change, breakup, or coalescence is activated. This parcel-based statistical representation dramatically reduces computational cost while preserving the essential dynamics of the dispersed phase. The exchange of momentum, heat, and mass between the dispersed and continuous phases is computed based on the local properties and trajectories of the parcels. After each time step, the contributions

of all parcels within a computational cell are accumulated and used to update the interphase source terms in the Eulerian equations. As a result, the parcels act as moving sampling elements that convey the averaged behavior of the real particle population, enabling two-way coupling between phases without explicitly resolving millions of individual particles.

2.5.1 Numerical Scheme

The Phase-Coupled SIMPLE (PC-SIMPLE) algorithm available in ANSYS Fluent 2025 R1 was employed as the pressure–velocity coupling scheme. PC-SIMPLE is an extension of the classical SIMPLE method to multiphase flows, in which the momentum equations are solved for each phase in a segregated manner but are coupled through a single pressure field. Fluxes are reconstructed at the faces of every control volume, and a global pressure-correction equation is then assembled from the mixture-continuity constraint to enforce mass conservation for all phases simultaneously.

The general procedure is as follows. First, the momentum equations of each phase are solved using a guessed pressure field to obtain provisional velocities $\mathbf{v}_q^*$. A pressure-correction equation is then formed from the summed continuity of all phases,

$$\sum_{q=1}^{N_{\mathrm{ph}}} \nabla\cdot(\phi_q \mathbf{u}_q) = 0, \tag{2.126}$$

which yields the algebraic relation

$$a_P\, p'_P = \sum_{nb} a_{nb}\, p'_{nb} + b_P, \tag{2.127}$$

where b_P represents the mixture mass imbalance and the coefficients a_P and a_{nb} are derived from the linearized per-phase momentum equations. After solving for the pressure correction

p', the pressure and velocities of each phase are updated according to:

$$p^{\text{new}} = p^{\text{old}} + \alpha_p \, p', \tag{2.128}$$

$$\mathbf{u}_q^{\text{new}} = \mathbf{u}_q^* - \frac{\nabla p'}{a_P^{(q)}}, \qquad q = 1, \ldots, N_{\text{ph}}. \tag{2.129}$$

The corrected fields automatically satisfy both individual-phase and overall continuity constraints. This iterative procedure is repeated until the residuals of continuity and momentum fall below the specified tolerances. PC-SIMPLE has proven to be numerically robust for Eulerian and Eulerian–Lagrangian two-phase simulations because it preserves a single, consistent pressure field while allowing the velocities of different phases to evolve independently.

2.5.2 Spatial and Temporal Discretization

All numerical simulations were performed using a structured mesh and a finite-volume formulation. Convective terms in the governing equations were discretized using a second-order upwind scheme. This scheme reconstructs variable values at the cell faces from a linear interpolation of the upstream gradient, providing second-order spatial accuracy while maintaining boundedness and monotonicity of the transported quantities. Compared with the first-order upwind formulation, which introduces numerical diffusion and attenuates small-amplitude pressure fluctuations, the second-order approach better preserves the amplitude and phase of the propagating acoustic perturbation wave. The pressure gradient was discretized using a second-order scheme, and gradients were computed with the least-squares cell-based method to maintain accuracy over the structured grid.

The spatial resolution was determined based on the acoustic wavelength corresponding to the highest perturbation frequency considered ($f_{\max} = 500$ Hz). Following the recommendation of Kazarina [41], a minimum of 40 cells per wavelength is required to accurately resolve one-dimensional acoustic perturbations in a quadrilateral structured grid and to minimize numerical dissipation.

However, because the acoustic perturbations analyzed in this work have very small amplitudes (on the order of 1 Pa), a grid sensitivity analysis was performed using a domain containing only air. In this analysis, and for the highest perturbation frequency, the number of cells per wavelength was progressively increased until the total numerical dissipation was reduced to less than 5% of the initial perturbation amplitude, measured at a distance of 1 meter from the boundary where the acoustic wave is generated. This reference location was selected because it corresponds to the end of the region that will later contain the suspended water particles in the multiphase simulations.

The physical time step was set to $\Delta t = 1 \times 10^{-6}$ s. To ensure temporal independence, a sensitivity analysis was performed by varying the time step between 1×10^{-7} s and 1×10^{-6} s in increments of 2×10^{-7} s. No significant variation was observed in the pressure or velocity histories for the single-phase (air-only) case, confirming temporal convergence at the selected value. The corresponding Courant number for the adopted cell size and time step is approximately 0.35, which satisfies stability and accuracy criteria for transient acoustic simulations.

2.5.3 Computational Domain and Boundary Conditions

The computational domain was defined as a two-dimensional rectangular region representing a one-dimensional acoustic propagation channel. Symmetry boundary conditions were imposed on the top and bottom boundaries to suppress any transverse velocity components, thereby enforcing a purely longitudinal acoustic field. The computational grid consists of approximately 15,000 structured rectangular cells, each with a uniform size of 1 mm $\times$ 1 mm. The total dimensions of the domain are 4 milliliters in the transverse direction and 3 meters in the streamwise (wave-propagation) direction. This mesh resolution satisfies that the numerical dissipation remains below 5% of the initial perturbation amplitude at 1 m from the inlet. A close-up view of the computational domain is presented in Figure 2.15.

The acoustic perturbation was modeled as a one-dimensional wave since, according to

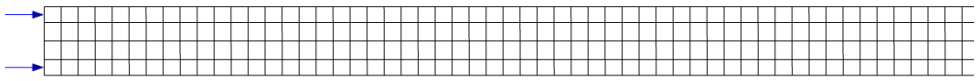

Figure 2.15 Close-up view of the structured computational mesh near the inlet boundary.

the theoretical formulation developed in the perturbation analysis, the problem lies in the far-field regime, where the curvature of spherical waves becomes negligible and the acoustic fronts can be locally approximated as planar. This assumption allows direct comparison between the perturbation approach and the CFD simulations. Accordingly, the left boundary of the domain was defined as a pressure inlet through which the one-dimensional acoustic perturbation wave was introduced. At this boundary, a sinusoidal time-varying pressure corresponding to a plane harmonic wave of prescribed frequency and amplitude was imposed using a user-defined function (UDF) written in C, which defines the temporal pressure variation as:

$$p'(t) = A_{\mathrm{p}} \sin(2\pi f t + \theta)\,, \tag{2.130}$$

where A_{p} is the acoustic amplitude, f is the excitation frequency, and θ is the initial phase. The right boundary was defined as a non-reflecting pressure outlet allowing acoustic waves to leave the computational domain without producing artificial reflections that could contaminate the measured acoustic field. In ANSYS Fluent, the non-reflecting outlet is formulated using a characteristic-wave approach that modifies the local static pressure according to the direction and magnitude of the outgoing acoustic flux, effectively mimicking an anechoic termination. This treatment is essential in the present study to ensure that the observed attenuation results exclusively from the physical interactions between the acoustic wave and the suspended particles, rather than from numerical reflections.

2.5.4 Verification for the Base Case without Particles in the Domain

Before applying the perturbation source model to the multiphase simulations, it was first verified in a single-phase air domain to ensure that the imposed acoustic disturbance propagated correctly without spurious numerical reflections or amplitude distortion. Figure 2.16

presents a comparison between the analytical expression for a pressure disturbance and the CFD-predicted pressure signals at two monitoring locations along the propagation direction. The CFD results reproduce the analytical waveform with excellent agreement in both amplitude and phase over the full time window, indicating that the numerical scheme introduces negligible dissipation and dispersion under the selected spatial and temporal resolutions.

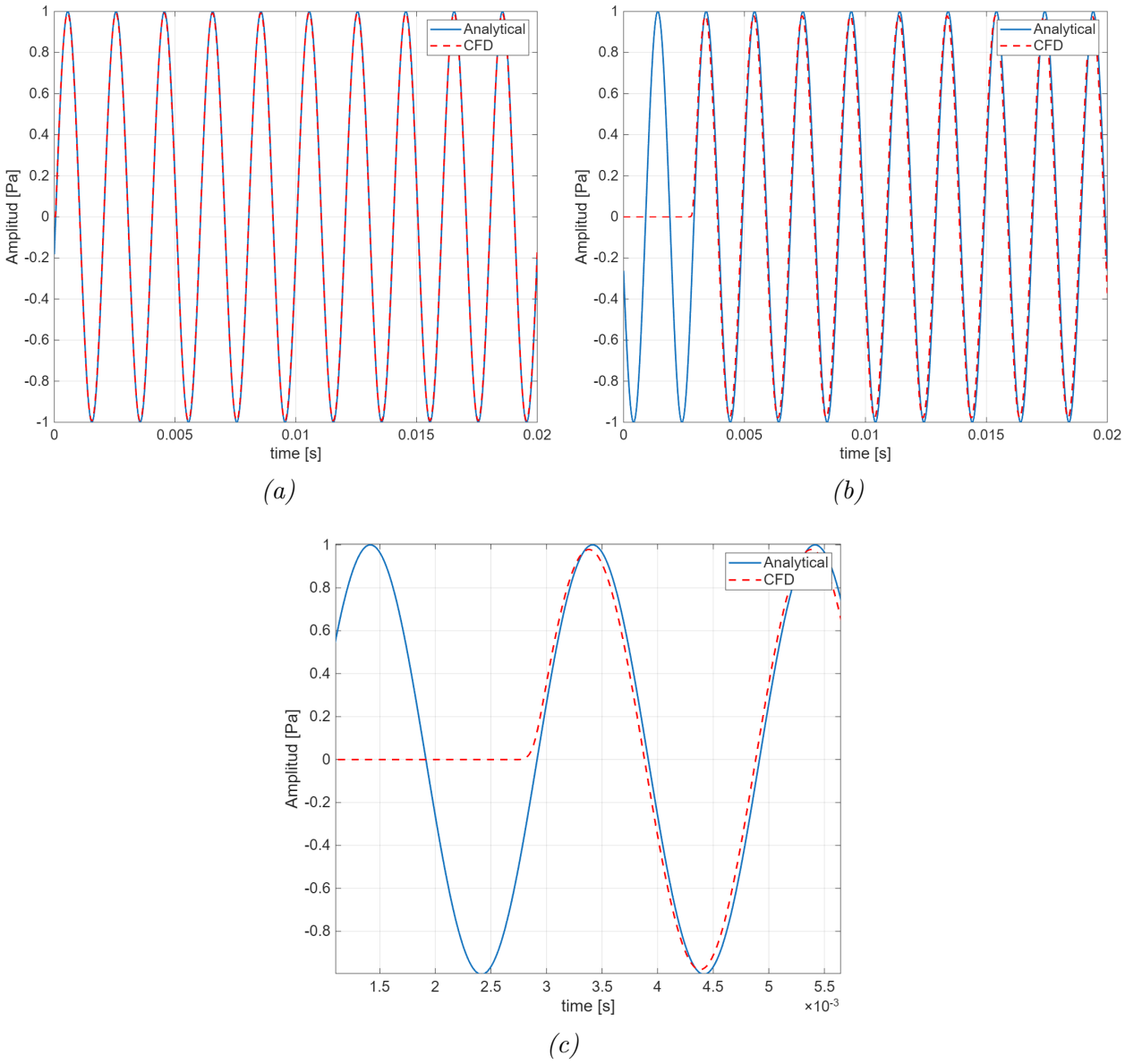

Figure 2.16 comparison between the analytical pressure variation and the CFD results. (a) At inlet boundary, (b) At 1 meter from the inlet boundary, and (c) Close-up view at 1 meter from the inlet boundary.

2.5.5 Particle Cloud and Dispersed Phase Characterization

Two mean particle volume fractions, $\phi_p = 0.001$ and $\phi_p = 0.005$, were selected for the simulations to compare with the perturbation-based results. In the DDPM framework, the water particles were initialized as a pre-existing particle cloud uniformly distributed throughout the domain at $t = 0$. This cloud was generated by specifying a set of parcels, each representing a large number of identical physical particles, so that the prescribed volume fraction and particle size distribution were satisfied from the start of the simulation. The particle diameters and the corresponding nondimensional frequency $\tau_p\omega$ employed in the simulations are summarized in Table 2.1.

Table 2.1 Summary of dispersed phase relaxation parameters selected.

ϕ_p	d_p [$\times 10^{-5}$ m]	$\boldsymbol{\tau_p\omega}$
0.001	1.0	0.980
	1.7	2.739
	2.5	4.907
	4.0	15.720
	7.0	48.150
	15.0	221.080
0.005	1.5	2.210
	2.0	3.857
	2.5	6.140
	4.0	15.410
	7.0	47.170
	15.0	216.602

For all simulations, the water droplets were modeled as spherical, non-evaporating particles, and breakup, collision, and DEM-based interactions were disabled to remain consistent with the assumptions of the suspended-droplet theoretical model. Only the pressure-gradient force was activated in the DDPM force balance, consistent with the low-Reynolds-number oscillatory motion expected for small-amplitude acoustic perturbations. Virtual mass, Saffman lift, thermophoretic, and other secondary forces were omitted, as their contributions become negligible for the suspended, non-convective conditions considered. Momentum exchange between the phases employed the "spherical" drag law available in ANSYS Fluent, which

corresponds to the standard Schiller–Naumann drag. Thermal coupling between droplets and the carrier phase was modeled through a constant Nusselt number of Nu = 2, representing pure conductive heat transfer around a stationary sphere and ensuring consistency with the theoretical assumptions.

The computational domain was divided into three regions as shown in Figure 2.17. For each case, the particles remained uniformly suspended within Region 2, corresponding to the portion of the domain where the acoustic attenuation was evaluated.

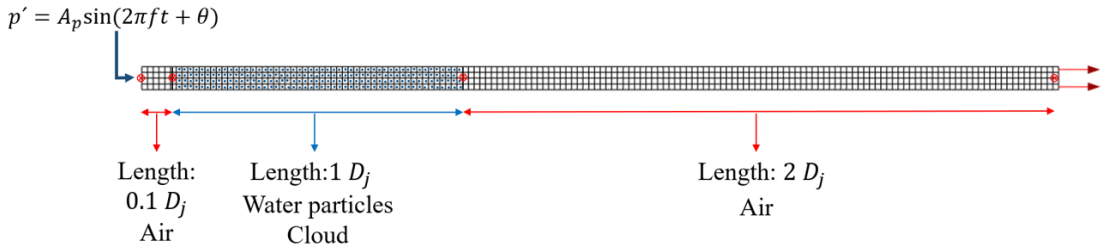

Figure 2.17 Sketch of distribution of the phases in the domain. Here, it is assumed D_j=1 m.

The cloud parameters for a representative particle diameter of $d_p = 1.5 \times 10^{-4}$ m are summarized in Table 2.2. Furthermore, Figure 2.18 presents a close-up view of the particle parcel distribution within the computational domain for the same diameter. Each red dot represents a parcel containing a group of identical particles determined by the injection statistics.

Table 2.2 Summary of cloud parameters.

Parameter	$\phi_p = 0.005$	$\phi_p = 0.001$
Total number of parcels	3904	3904
Total number of particles	1.01807×10^7	2.21396×10^6
Total mass [kg]	1.79584×10^{-2}	3.90400×10^{-3}
Overall diameter d_p [m]	1.50×10^{-4}	1.50×10^{-4}

Figure 2.19 shows a close-up view of the resulting volume fraction distributions in the computational domain for both volume fraction cases.

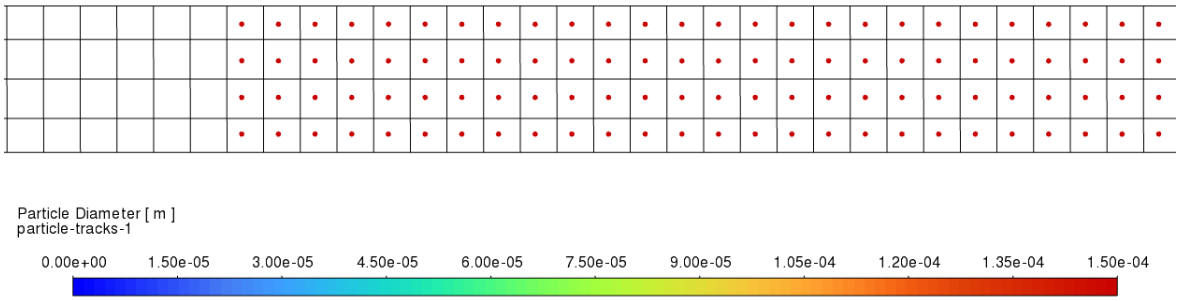

Figure 2.18 Cloud parcels for $d_p = 5 \cdot 10^{-4}$.

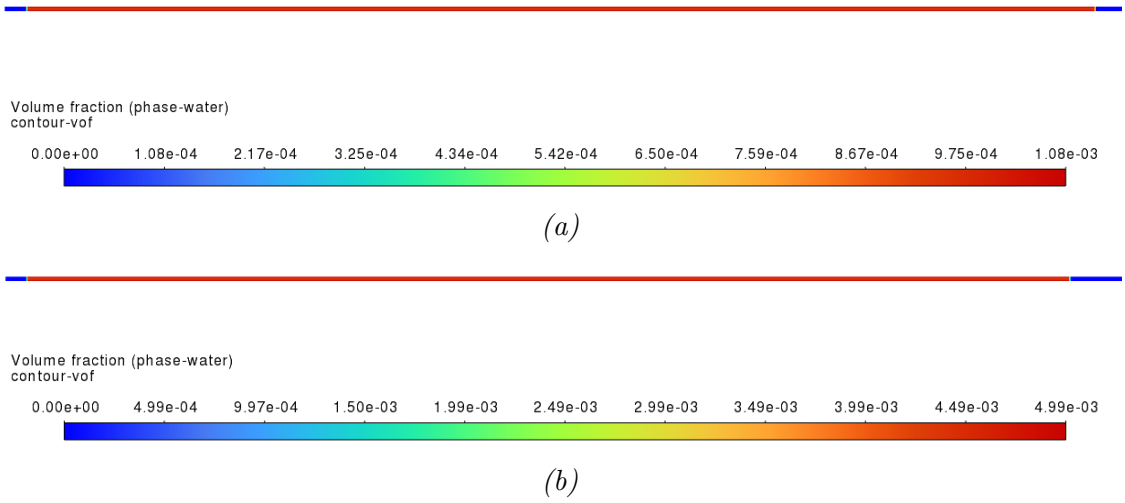

Figure 2.19 Volume of fraction in the compatuational domain. a) $\phi_p = 0.001$, and b) $\phi_p = 0.005$.

2.5.6 Wave Attenuation Results With Water Particles in the Domain

To evaluate the attenuation characteristics induced by the dispersed phase, two sets of simulations were conducted for each configuration: one with air as a single-phase medium and another including water droplets distributed according to the cloud setup described in the previous section. In both cases, the acoustic wave propagation was analyzed by monitoring the pressure perturbation amplitude at two axial locations, positioned upstream and downstream of the water-particle curtain, using virtual microphones. The amplitude ratios for the single-phase and multiphase simulations were defined respectively as

$$R_{\text{air}} = \frac{A_{\text{out}}^{\text{air}}}{A_{\text{in}}^{\text{air}}}, \qquad R_{\text{mix}} = \frac{A_{\text{out}}^{\text{mix}}}{A_{\text{in}}^{\text{mix}}}, \tag{2.131}$$

where A_{in} and A_{out} denote the pressure amplitudes measured before and after the particle-laden region, respectively. To isolate the attenuation effect caused by the interaction with the mixture from the inherent numerical dissipation, a normalization procedure was applied. The normalized physical attenuation ratio is expressed as:

$$R_{\text{phys}} = \frac{R_{\text{mix}}}{R_{\text{air}}}. \tag{2.132}$$

This ratio provides a direct measure of the attenuation induced by the water particles:

$$R_{\text{phys}} = \begin{cases} < 1 & \text{attenuation,} \\ = 1 & \text{no change in amplitude,} \\ > 1 & \text{amplification or reflections.} \end{cases}$$

As discussed earlier in this document, in a damping medium the acoustic pressure amplitude decays exponentially with propagation distance according to $|p'(x,t)| \propto e^{-k_i x}$, where k_i represents the imaginary part of the complex wavenumber, associated with the attenuation coefficient of the medium. Relating the measured amplitude ratio to the mixture thickness L, the exponential decay across the particle-laden region can be written as:

$$\frac{A_{\text{out}}}{A_{\text{in}}} = e^{-k_2 L}. \tag{2.133}$$

By combining Equations 2.132 and 2.133, k_i can be obtained as

$$k_i = -\frac{1}{L} \ln(R_{\text{phys}}). \tag{2.134}$$

This formulation enables a direct estimation of the imaginary part of the complex wavenumber from the numerical simulation results, isolating the physical attenuation due to mixture–wave interactions. The same procedure was applied to all particle diameters and volume fractions considered in the study.

Figures 2.20–2.25 present the temporal evolution of the pressure perturbation amplitude measured immediately after the mixture curtain for different particle diameters and volume fractions at a frequency of $f = 500$ Hz. In all configurations, the waveform corresponding to the mixture exhibits a noticeable reduction in amplitude compared with the single-phase air case, confirming the damping effect introduced by the particle phase.

For the same particle volume fraction ($\phi_p = 0.001$), a clear dependence on particle diameter is observed. The attenuation is stronger for smaller particles, as shown in Figures 2.20 and 2.21, and gradually weakens with increasing diameter (Figure 2.22). This behavior is consistent with the relaxation parameter $\tau_p\omega$, which characterizes the dynamic response of the particles to the acoustic oscillations. When $\tau_p\omega$ is close to unity, as for $d_p = 2.5 \times 10^{-5}$ m, the particle velocity lags the fluid oscillation most effectively, leading to maximum momentum and thermal energy exchange between the phases. Consequently, the acoustic energy is more efficiently dissipated, resulting in greater attenuation of the pressure amplitude. A similar trend is evident when varying the particle volume fraction at a fixed diameter. Comparing Figures 2.21 and 2.23, it is observed that increasing the dispersed-phase concentration from $\phi_p = 0.001$ to $\phi_p = 0.005$ enhances the overall attenuation. This effect arises from the larger number of particles per unit volume, which increases the cumulative interphase momentum and heat transfer, amplifying the damping of acoustic oscillations.

For larger particles ($d_p \geq 7 \times 10^{-5}$ m), the attenuation becomes significantly weaker, as illustrated in Figures 2.24 and 2.25. In these cases, the particle relaxation time exceeds the acoustic period ($\tau_p\omega \gg 1$), resulting in a nearly inertial particle response that follows the fluid motion less effectively. As a consequence, the phase interaction is reduced, and the mixture behaves more like a homogeneous continuum with minimal additional damping relative to air.

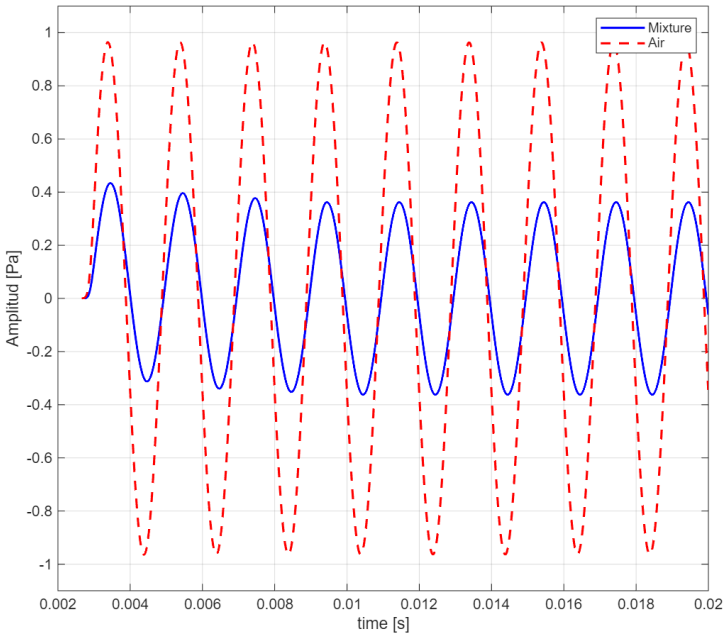

Figure 2.20 Pressure perturbation amplitude for the case with $\phi_p = 0.001$, $d_p = 2.5 \times 10^{-5}$ m, and $f = 500Hz$ comparing the single-phase air and mixture cases.

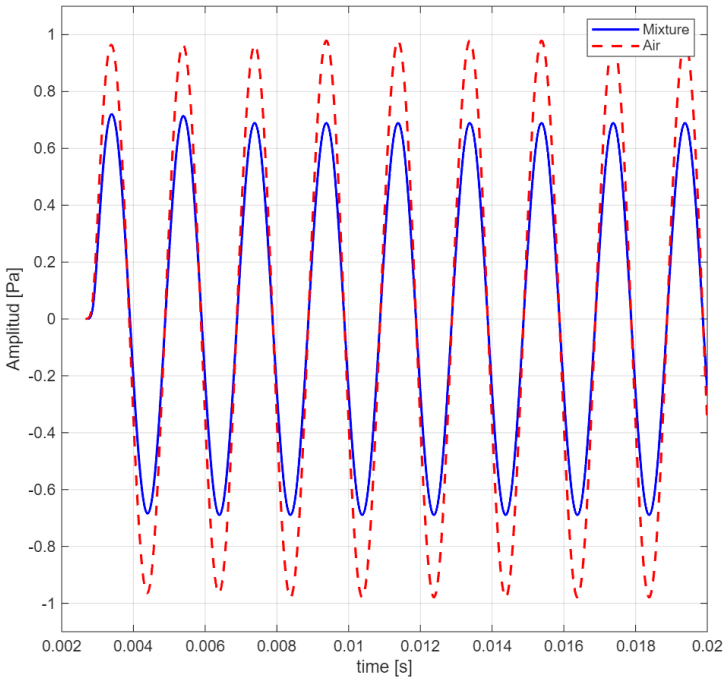

Figure 2.21 Pressure perturbation amplitude for the case with $\phi_p = 0.001$,$d_p = 4 \times 10^{-5}$ m, and $f = 500Hz$ comparing the single-phase air and mixture cases.

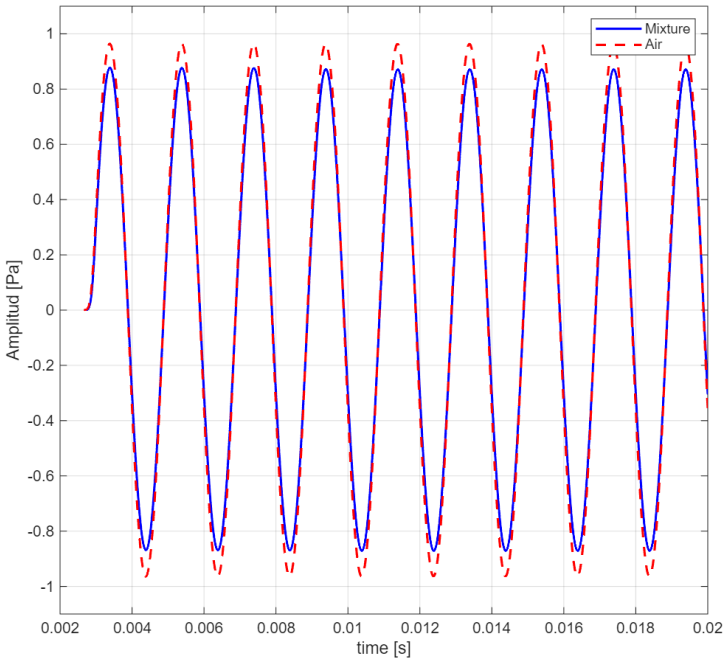

Figure 2.22 Pressure perturbation amplitude for the case with $\phi_p = 0.001$, $d_p = 7 \times 10^{-5}$ m, and $f = 500Hz$ comparing the single-phase air and mixture cases.

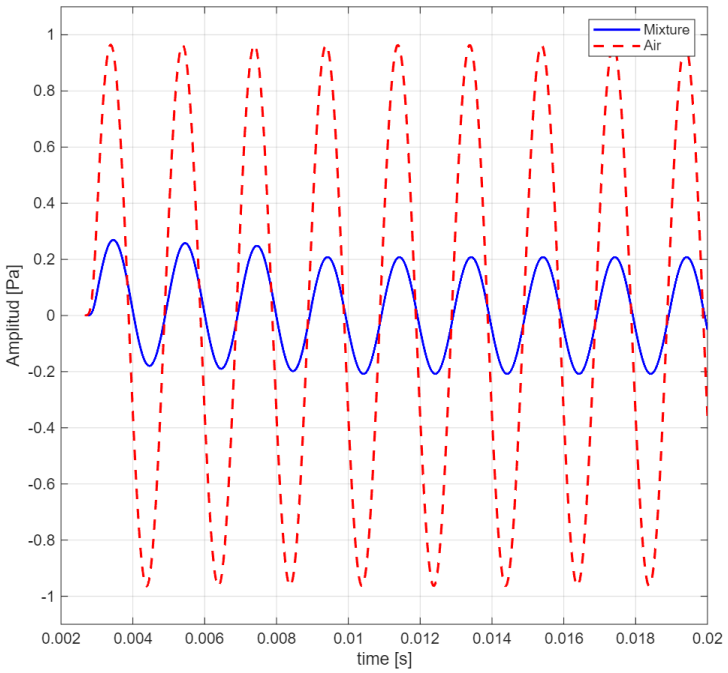

Figure 2.23 Pressure perturbation amplitude for the case with $\phi_p = 0.005$, $d_p = 4 \times 10^{-5}$ m, and $f = 500Hz$ comparing the single-phase air and mixture cases.

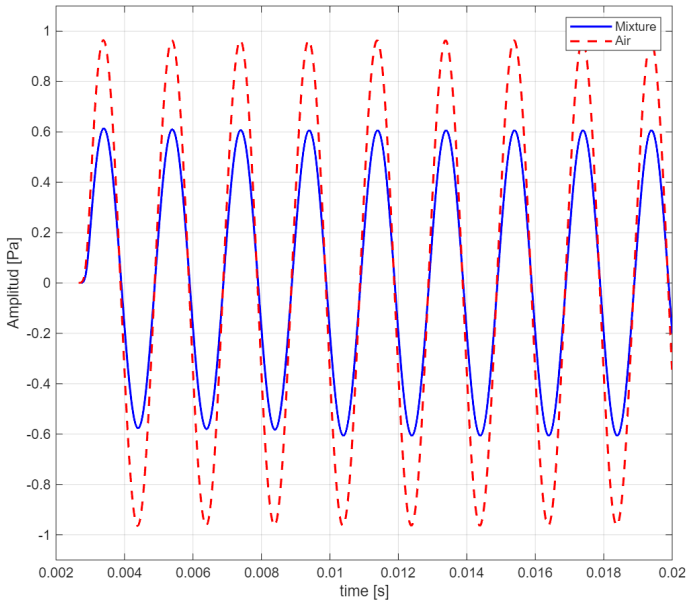

Figure 2.24 Pressure perturbation amplitude for the case with $\phi_p = 0.005$, $d_p = 7 \times 10^{-5}$ m, and $f = 500Hz$ comparing the single-phase air and mixture cases.

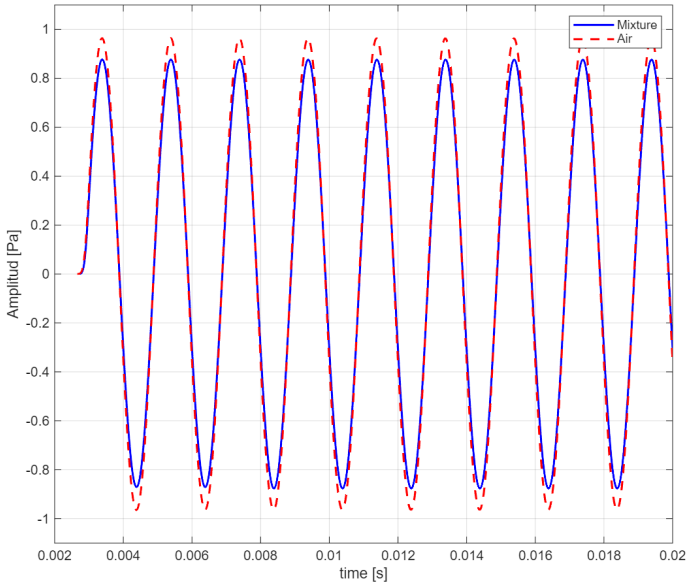

Figure 2.25 Pressure perturbation amplitude for the case with $\phi_p = 0.005$, $d_p = 1.5 \times 10^{-4}$ m, and $f = 500Hz$ comparing the single-phase air and mixture cases.

2.5.7 Reduction Factor k_i^+ from CFD Simulations

Figures 2.26 and 2.27 present the reduction factor k_i^+ as a function of the dimensionless frequency $\Omega = \omega\tau_p$ and the particle diameter d_p, respectively. The CFD results exhibit strong quantitative agreement with the perturbation-based predictions, accurately capturing both

the location and magnitude of the attenuation peak. This consistency validates the reliability of the perturbation approach in predicting the acoustic attenuation behavior of dispersed multiphase mixtures.

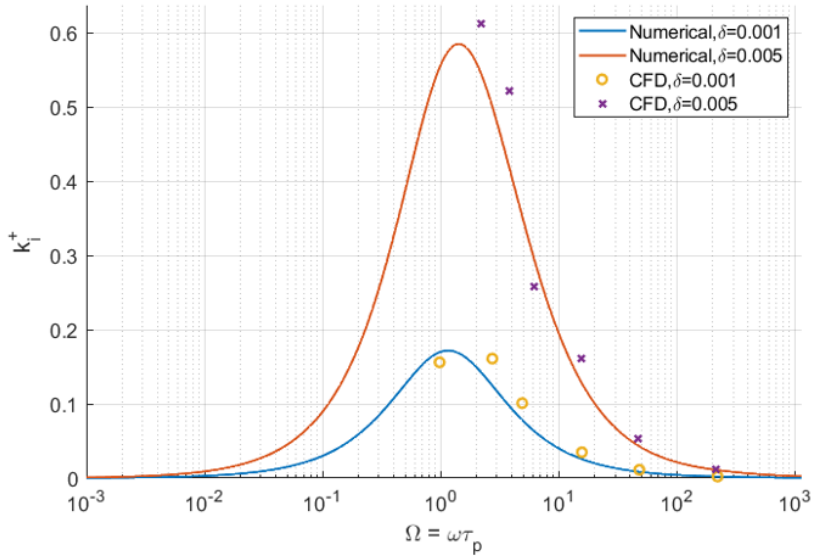

Figure 2.26 Reduction factor k_i^+ as a function of the dimensionless frequncy Ω comparing numerical results obtained from the perturbation approach and CFD for different volume of fraction ratios δ.

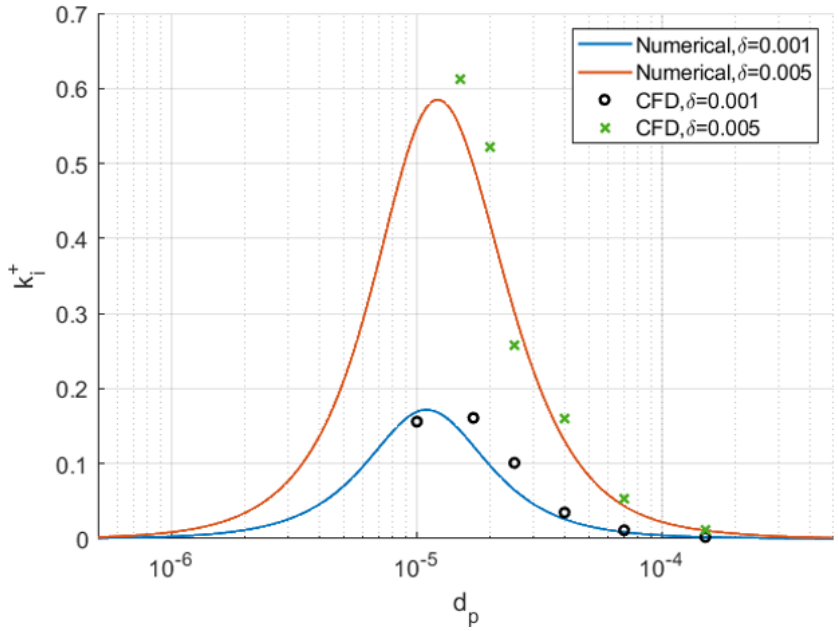

Figure 2.27 Reduction factor k_i^+ as a function of the particle diameter d_p comparing numerical results obtained from the perturbation approach and CFD for different volume of fraction ratios δ.

2.6 Dispersed Particle Case

In this section, the linearized perturbation equations are solved for the case in which the gas phase exhibits a prescribed initial mean velocity. This configuration corresponds to gas background flow interacting with a water particle-laden region initially at rest. The objective is to investigate how the presence of mean flow and interphase slip influences acoustic attenuation, in comparison with the suspended case previously analyzed. The results presented here provide a framework for quantifying the role of convective effects and velocity coupling in determining the attenuation characteristics of multiphase mixtures.

For the present analysis, the water curtain is positioned at a cross-jet distance and axial distance of where the gas velocity is approximately 2 m/s. This value will be adopted as the velocity incident on the water curtain and will serve as an input for solving the perturbation equations in the presence of a given air velocity. However, note that in the context of aircraft carrier operations the water curtain location is a function of the operational environment.

2.6.1 Mean Flow Equations

Now, the focus is on determining the mean flow components of the perturbation equations, as they appear explicitly in the convective and coupling terms. Here, mean-flow components are extracted from the radial, non-perturbed and steady version of the governing equations presented in Equations 3.21-2.27. Furthermore, thermal equilibrium between the phases is assumed, therefore thermal energy equations here are neglected.
The resulting system reduces to a set of coupled ordinary differential equations in the radial coordinate, as shown below:

$$\frac{\partial(\rho_g \phi_g U_g)}{\partial r} + \frac{2\rho_g \phi_g U_g}{r} = 0, \tag{2.135}$$

$$\left[\frac{\partial(\rho_g \phi_g U_g U_g)}{\partial r} + \frac{2(\rho_g \phi_g U_g U_g)}{r}\right] + \phi_g \frac{\partial(\rho_g R T_g)}{\partial r} + \rho_p \Psi \frac{\phi_p}{\tau_p}(U_g - U_p) = 0, \tag{2.136}$$

$$\frac{\partial(\phi_p U_p)}{\partial r} + \frac{2 U_p \phi_p}{r} = 0, \tag{2.137}$$

$$\left[\frac{\partial(U_p U_p \phi_p)}{\partial r} + \frac{2(U_p U_p \phi_p)}{r}\right] + \frac{\phi_p}{\rho_p}\frac{\partial(\rho_g R T_g)}{\partial r} - \Psi\frac{\phi_p}{\tau_p}(U_g - U_p) = 0. \tag{2.138}$$

The boundary conditions at ($\xi = 0$) are: $U_g = 2\,\frac{m}{s}$, $U_p = 0\,\frac{m}{s}$, $\phi_g = 0.9, \phi_p = 0.1$. These conditions are chosen to represent a configuration where the incoming air stream impinges on the mixture with finite radial velocity, while the dispersed phase (water droplets) is initially at rest, modeling sudden release of particles into the gas field.

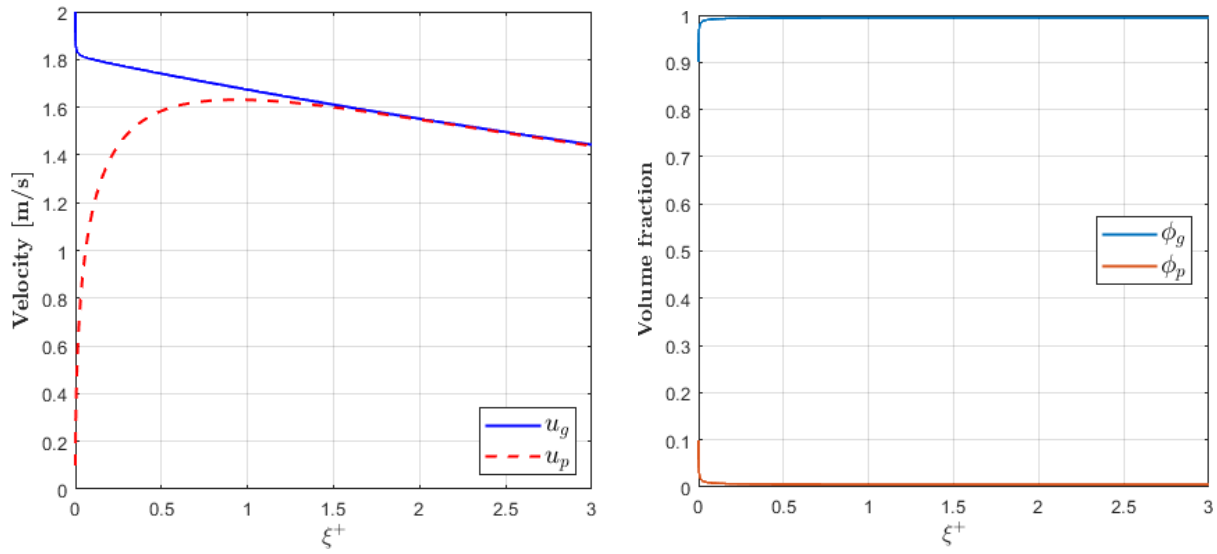

(a) Mean velocity

(b) Mean volume fraction

Figure 2.28 Numerical solution of the mean flow equations: (a) Mean flow velocities and (b) Mean volume fraction.

The numerical solution of the mean flow system is presented in Figure 2.28. Mean velocities indicate that the system initially departs from equilibrium as the flow evolves along the distance ξ, the gas and particle velocities gradually converge, suggesting a relaxation toward dynamic equilibrium between the two phases. The mean volume of fraction shows that if starting volume of fraction for gas and particles of 0.5 the mean volume of fraction of particles decreases as the flow evolves along the distance ξ, this is because it is dispersed into a larger volume, the effective volumetric density decreases.

2.6.2 Effect of Interphase Relative Motion on Acoustic Wave Attenuation

The influence of Ω on k_i^+ is examined at two radial positions, the first location corresponds to the location in which the background flow hits the curtain and the relative velocity between the gas and particle phases is largest,and the second location corresponds to a downstream position where both phases have reached dynamic equilibrium. These two locations are selected to assess how interphase velocity slip influences the attenuation behavior. Figure 2.29 shows that when relative motion is introduced between the phases the attenuation peak shifts toward higher dimensionless frequencies, and its maximum value is reduced. This reduction could be attributed to the convective transport of acoustic perturbation by the mean flow, decreasing the interaction time between the wave and the particles. In contrast, when both phases move at similar velocities and the relative slip between them is negligible, the attenuation behavior remains nearly identical to the suspended case.

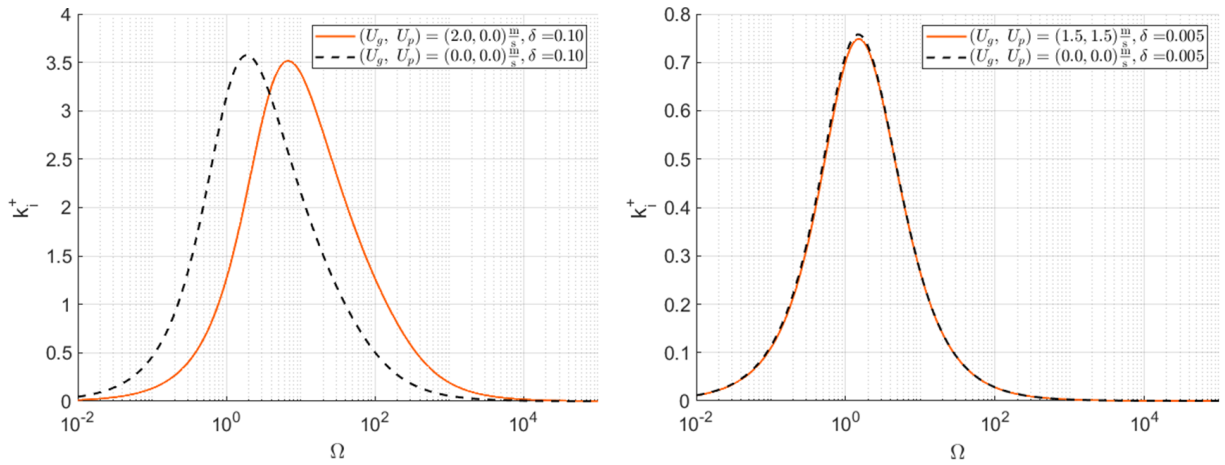

(a) *(b)*

Figure 2.29 Effect of Ω on k_i^+ with phase motion. a)with phase slip and b)without phase slip.

For the dispersed case, the dependency of the noise reduction on the Strouhal Number follows the same trend as the suspended case, however, as can be seen in the Figure 2.30 the presence of relative motion increases the noise reduction with respect to the suspended case for the same value of volume of fraction. In contrast, when both phases move at similar velocities, the trend of dependency on the Strouhal number remains nearly identical to the

suspended case.

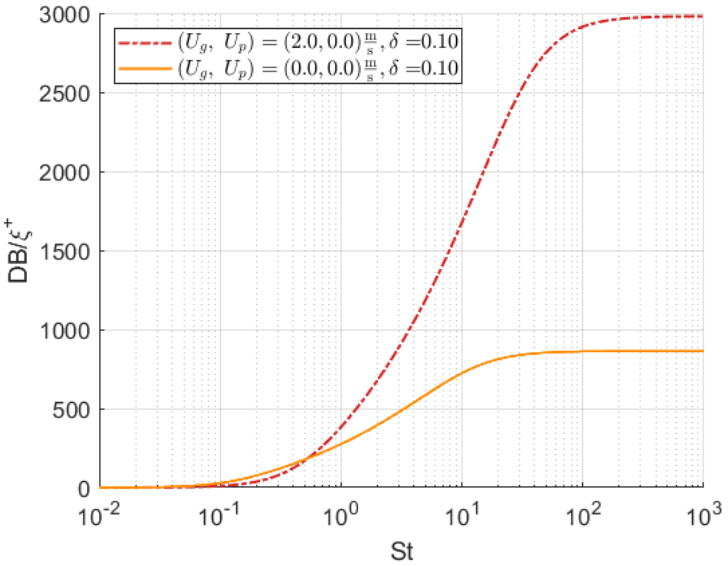

Figure 2.30 Dependency of the noise reduction on the Strouhal number with relative motion between the phases.

2.6.3 Solution of the Perturbation Equations as a Function of the Mean Flow Results

Here the perturbation equations are solved for k_i^+ as a function of ξ using the radial mean flow obtained in Section 2.6.1. Then, following Equation 2.117 with $M_j = 1$ and St $= 0.5$, the effect of droplet diameter on the normalized noise reduction DB/ξ^+ is evaluated. The results presented in Figure 2.31 reveal the existence of an optimal droplet diameter of about 0.0003 of the jet diameter for both suspended and dispersed cases.

2.6.4 Attenuation factor k_i^+ and Normalized Noise Reduction as a Function of ξ^+

Based on the identified optimal diameter ratio, Figure 2.31 presents the normalized noise reduction for both the suspended and dispersed configurations with $d_p/D_j = 0.4$, $R_j = 10^5$, $M_j = 1$, and St $= 0.5$, using the volume fraction determined from the mean flow equations. While earlier results show that the maximum local attenuation is lower in the presence of mean flow, the results in Figure 2.32 reveal that the dispersed case exhibits slightly higher attenuation values. This behavior is attributed to the frequency shift induced by the convective flow, which causes the attenuation to be redistributed spatially.

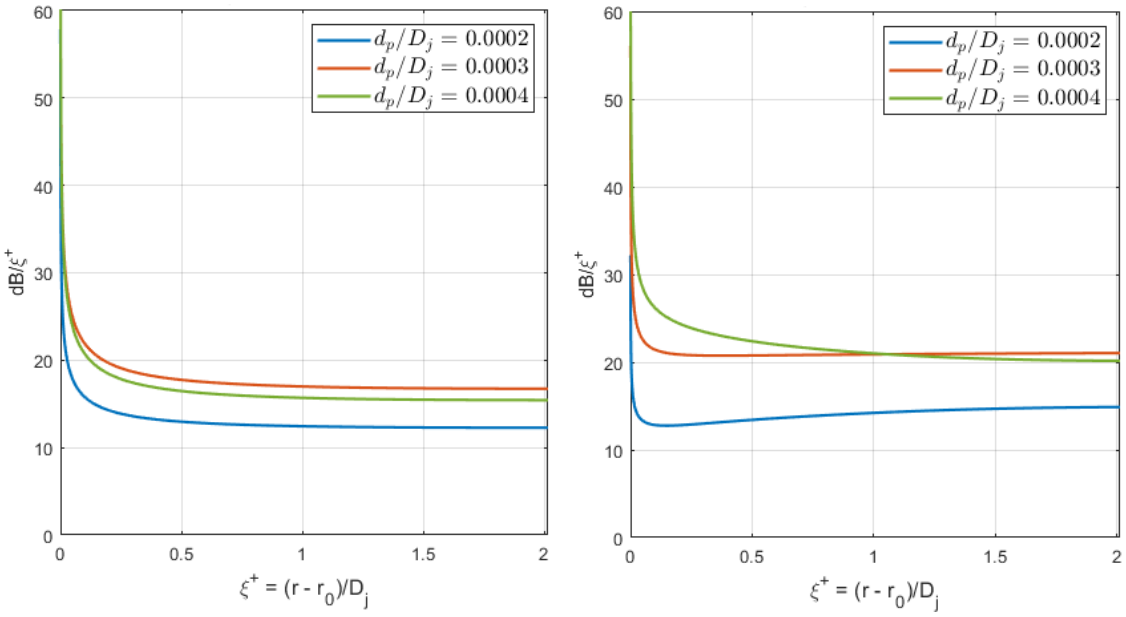

Figure 2.31 Effect of droplet diameter on the normalized noise reduction DB/ξ^+. a) Suspended case. b) Dispersed case.

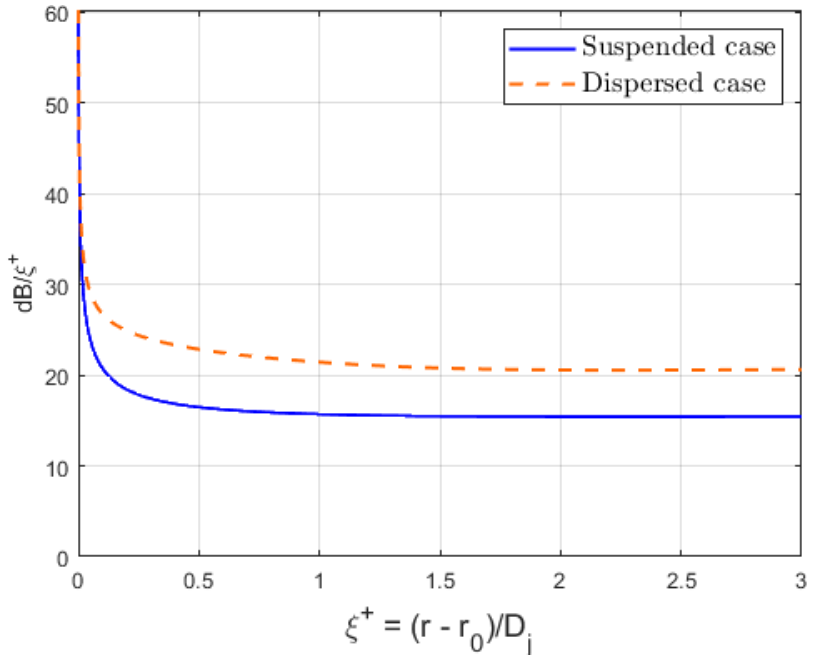

Figure 2.32 Normalized noise reduction dB/ξ^+ as functions of the normalized radial coordinate ξ^+.

3 Methodology, Bubbly Case

In the present work, the focus is on the region outside the jet flow, as illustrated in Figure 3.1. Immediately beyond the jet boundary, the surrounding medium consists of ambient air. At a certain radial distance, an air–water curtain is introduced, forming a localized multiphase domain. The multiphase flow equations are applied within this domain and then the flow is decomposed into mean and perturbation components to obtain the linearized perturbation equations that are used to describe the propagation and attenuation of acoustic waves across the mixture.

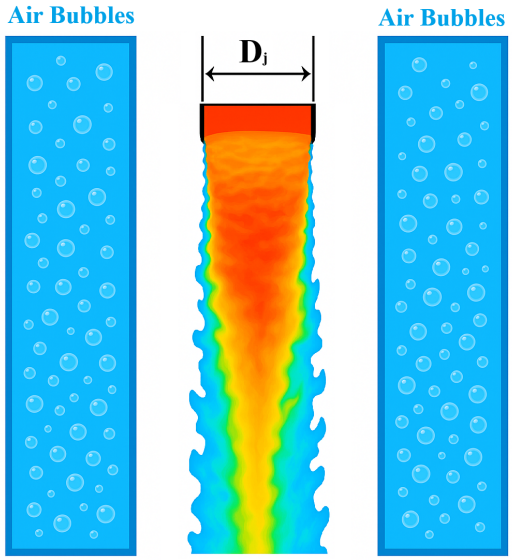

Figure 3.1 Air-water mixture surrounding the jet..

3.1 The Governing Equations

Acoustic waves traveling through a mixture of water and air bubbles is considered here. We start with an Eulerian approach and following assumptions are made: (1)The fluid motion is regard as inviscid (2); Bubbles are spherical and have small changes in its shape; (3) Bubbles do not collide with each other and do not collapse; (4) Surrounding flow is dominated by water, therefore, perturbation takes place in an incompressible liquid; (5) Volume-averaged Reynolds stresses and body forces are neglected; (6) Liquid pressure far from the bubbles is assume as constant; and (7) The density of each phase depends only

on its pressure and temperature. Following Temkin [40], the continuity, momentum and thermal equations for the gas phase are represented as:

$$\frac{\partial(\rho_g \phi_g)}{\partial t} + \nabla \cdot (\phi_g \rho_g \mathbf{u}_g) = 0, \tag{3.1}$$

$$\frac{\partial(\rho_g \phi_g \mathbf{u}_g)}{\partial t} + \nabla \cdot (\phi_g \rho_g \mathbf{u}_g \mathbf{u}_g) = -\phi_g \nabla p_g - \mathbf{F}_{QS}, \tag{3.2}$$

$$C_{pg}\left[\frac{\partial}{\partial t}(\phi_g \rho_g T_g) + \nabla \cdot (\phi_g \rho_g T_g \mathbf{u}_g)\right] - \phi_g \beta_g T_g \left(\frac{\partial p_g}{\partial t} + \mathbf{u}_g \cdot \nabla p_g\right) = Q_{gf} \tag{3.3}$$

For the fluid phase, the continuity and momentum are given by:

$$\frac{\partial(\rho_f \phi_f)}{\partial t} + \nabla \cdot (\phi_f \rho_f \mathbf{u}_f) = 0, \tag{3.4}$$

$$\frac{\partial(\mathbf{u}_f \phi_f \rho_f)}{\partial t} + \nabla \cdot (\phi_f \mathbf{u}_f \mathbf{u}_f \rho_f) = -\phi_p \nabla p_f + \mathbf{F}_{QS}, \tag{3.5}$$

$$C_{pf}\left[\frac{\partial\left(\rho_f \phi_f T_f\right)}{\partial t} + \nabla \cdot (\rho_f \phi_f T_f \mathbf{u}_f)\right] - \phi_f \beta_f T_f \left[\frac{\partial p_f}{\partial t} + \mathbf{u}_f \cdot \nabla p_f\right] = -Q_{gf} \tag{3.6}$$

The variables $u, p, \rho, T, \beta, C_p$ and ϕ refer to the vectorial velocity, pressure, density, temperature, coefficient of thermal expansion, specific heat and volume fraction, respectively, and the subscript "g" refers to air bubbles while "f" refers to liquid (water). Furthermore, it is to noted that the present analysis is limited to cases where the fluid volume fraction satisfies $\phi_f \geq 0.9$, ensuring that the system corresponds to a dispersed flow regime. Under this condition, particle–particle interactions are negligible, and the flow is not dominated by contact effects.

The system of equations above cannot be solved without additional closure relations, specifically equations of state for each phase. Explicit analytical forms of these equations are available only for certain cases, such as perfect gases, while for most materials the required data are provided in tabulated or graphical form. For the present analysis, it is assumed

that suitable equations of state exist for the materials of interest and that both the fluid and particle phases can be treated as simple substances, meaning that their thermodynamic states can be fully defined by two independent variables. Depending on the context, these variables may vary, but here temperature and density are chosen as the primary state variables for each phase, allowing the equations of state to be expressed as follows:

$$p_f = p_f(\rho_f, T_f), \tag{3.7}$$

$$p_g = p_g(\rho_g, T_g), \tag{3.8}$$

The gas pressure term in Equation 3.2 arises from the compressibility of the bubbles. To model this effect, the Rayleigh–Plesset equation is employed, which describes the temporal variation of the bubble radius R_b resulting from the pressure difference between the bubble interior and the surrounding fluid, as shown in Equation 3.9. Although this introduces an additional unknown into the governing equations, it will be demonstrated later in this section that, upon linearization, Equation 3.9 can be expressed in terms of pressure perturbations, thereby closing the system.

$$p_b = p_f + \rho_f R_b \frac{\partial^2 R_b}{\partial t^2} + \rho_f \left(\frac{4\nu_f}{R_b} + \frac{3}{2} \frac{\partial R_b}{\partial t} \right) \frac{\partial R_b}{\partial t}. \tag{3.9}$$

Here ν_f is the kinematic viscosity of the liquid phase. The fluid force acting on the bubbles during translational motions at small Reynolds numbers, is given by a formula that can be considered an extension of Stokes' law. The formula, obtained Hadamard in 1911, is

$$F_D = 4\pi\mu_f \, r_b(u_f - u_p) \, \frac{1 + \frac{3}{2}(\mu_g/\mu_f)}{1 + (\mu_g/\mu_f)} \tag{3.10}$$

Here, μ_f, μ_g and r_b denote the dynamic viscosities of the liquid and gas phases, and the mean bubble radius, respectively. The quasi-steady force F_{QS} and the heat transfer between the bubbles and liquid Q_{gf} are define as:

$$F_{QS} = \frac{12\mu_f}{d_b^2}\phi_g(u_f - u_g)\Psi(Re) \tag{3.11}$$

$$Q_{gf} = \frac{12\kappa_g}{d_b^2}\phi_g(T_f - T_g) \tag{3.12}$$

Where d_b is the bubble diameter and κ_g represent the coefficient of thermal conductivity for the gas phase. Assuming that the bubbles are small and spherical, the correlation by Schiller and Naumann [35] for the drag factor correction is applied as shown next:

$$\Psi(\mathrm{Re}) = 1 + 0.15\,\mathrm{Re}^{0.687}, \tag{3.13}$$

$$\mathrm{Re} = \frac{d_b}{\nu_f}\,|\mathbf{u}_g - \mathbf{u}_p|\,, \tag{3.14}$$

3.2 Bubbly Perturbed Equations

The flow variables and couple terms are split into a base flow and perturbation components as:

$$\begin{gathered}\phi_f = \Phi_f + \phi'_f; \quad \rho_f = \rho_f + \rho'_f; \quad \mathbf{u}_f = U_f + u'_f; \quad p_f = P_f + p'_f; \\ T_f = T_f + T'_f\end{gathered} \tag{3.15}$$

$$\begin{gathered}\phi_g = \Phi_g + \phi'_g; \quad \rho_g = \rho_g + \rho'_g; \quad \mathbf{u}_g = U_g + u'_g; \quad p_g = P_g + p'_g; \\ R_b = r_b + \epsilon; \quad T_g = T_g + T'_g|\end{gathered} \tag{3.16}$$

$$Q_{gf} = \overline{Q}_{gf} + Q'_{gf}; \quad F_{QS} = \overline{F}_{QS} + F'_{QS} \tag{3.17}$$

The base flow is considered known, and the analysis focuses on the perturbation equations. By combining the established base relations with the governing equations the linearized continuity,momentum and thermal equations for the gas bubbles in generalized curvilinear coordinates can be written as follows:

$$\frac{\partial}{\partial t}\left[\left(\rho_g+\rho_g'\right)\left(\phi_g+\phi_g'\right)\right]+\frac{\partial}{\partial x_i}\left[(\phi_g+\phi_g')(\rho_g+\rho_g')(U_g+u_g')_i\right]=0, \tag{3.18}$$

$$\begin{aligned}&\frac{\partial}{\partial t}\left[(\rho_g+\rho_g')(\phi_g+\phi_g')(U_g+u_g')_i\right]+\\&\frac{\partial}{\partial x_j}\left[(\phi_g+\phi_g')(\rho_g+\rho_g')(U_g+u_g')_j(U_g+u_g')_i\right]\\&=-(\phi_g+\phi_g')\frac{\partial}{\partial x_i}(P_g+p_g')+\left(\overline{F}_{QS}+F_{QS}'\right),\end{aligned} \tag{3.19}$$

$$\begin{aligned}&C_{pg}\left[\frac{\partial}{\partial t}\left[(\rho_g+\rho_g')(\phi_g+\phi_g')(T_g+T_g')\right]+\frac{\partial}{\partial x_j}\left[(\rho_g+\rho_g')(\phi_g+\phi_g')(T_g+T_g')(U_g+u_g')_j\right]\right]\\&-\beta_g(\phi_g+\phi_g')(T_g+T_g')\left(\frac{\partial}{\partial t}(P_g+p_g')+(U_g+u_g')_j\cdot\frac{\partial}{\partial x_j}(P_g+p_g')\right)=\overline{Q}_{gf}+Q_{gf}'\end{aligned} \tag{3.20}$$

The same procedure is applied to the liquid phase, yielding the perturbed forms of the continuity and momentum equations as follows:

$$\frac{\partial}{\partial t}\left[\left(\rho_f+\rho_f'\right)\left(\phi_f+\phi_f'\right)\right]+\frac{\partial}{\partial x_i}\left[(\phi_f+\phi_f')(\rho_f+\rho_f')(U_f+u_f')_i\right]=0, \tag{3.21}$$

$$\begin{aligned}&\frac{\partial}{\partial t}\left[(\rho_f+\rho_f')(\phi_f+\phi_f')(U_f+u_f')_i\right]+\\&\frac{\partial}{\partial x_j}\left[(\phi_f+\phi_f')(\rho_f+\rho_f')(U_f+u_f')_j(U_f+u_f')_i\right]\\&=-(\phi_g+\phi_g')\frac{\partial}{\partial x_i}(P_f+p_f')-\left(\overline{F}_{QS}+F_{QS}'\right),\end{aligned} \tag{3.22}$$

$$\begin{aligned}&C_{pf}\left[\frac{\partial}{\partial t}\left[(\rho_f+\rho_f')(\phi_f+\phi_f')(T_f+T_f')\right]+\frac{\partial}{\partial x_j}\left[(\rho_f+\rho_f')(\phi_f+\phi_f')(T_f+T_f')(U_f+u_f')_j\right]\right]\\&-\beta_f(\phi_f+\phi_f')(T_f+T_f')\left(\frac{\partial}{\partial t}(P_f+p_f')+(U_f+u_f')_j\cdot\frac{\partial}{\partial x_j}(P_f+p_f')\right)=-(\overline{Q}_{gf}+Q_{gf}').\end{aligned} \tag{3.23}$$

Following Temkin[40] in Chapter 6, equations of state for each phase, assuming liquid phase as an incompressible fluid, are linearized as follows:

$$p'_f = c^2_{Tf}\rho'_f, \tag{3.24}$$

$$p'_g = c^2_{Tg}\rho'_g + \frac{\rho_g c_{pg}}{\beta_f T_g}\frac{\gamma - 1}{\gamma}T'_g, \tag{3.25}$$

Here, C_{Tf} and C_{Tg} represent the isothermal speed of sound of the liquid and gas phases, respectively. To close the system of equations, Equation 3.9 is linearized following Temkin[40], where second-order terms are neglected, and the bubble's radial displacement,ϵ, is expressed as:

$$\varepsilon = -\frac{r_b}{3c^2_{Tg}\rho_g}p'_p \tag{3.26}$$

Substituting this relation into the linearized Rayleigh–Plesset equation yields to Equation 3.27 for the perturbed pressure relation.

$$p'_p = p'_f - \frac{\rho_f r_b^2}{3\rho_p c^2_{Tg}}\left(\frac{\partial^2 p'_p}{\partial t^2} + 2\beta_T\frac{\partial p'_p}{\partial t}\right) \tag{3.27}$$

It is to note that in the expression above, β_T represents the sum of two damping coefficients: β_μ, due to viscous effects,and β_{ac}, due to acoustic radiation, where:

$$\beta_\mu = \frac{2\mu_f}{\rho_f\ r_b} \tag{3.28}$$

$$\beta_{ac} = \frac{\omega^2}{4\ c_{TF}} \tag{3.29}$$

Viscous damping arises from shear stresses in the surrounding fluid as the bubble oscillates radially. When the particle boundary moves outward and inward, the fluid near the surface experiences velocity gradients producing viscous stresses that dissipate part of the perturbation energy. Acoustic radiation results from the emission of sound generated by the oscillating bubble, where pressure disturbances radiate into the surrounding medium,

carrying energy away from the oscillation.

3.2.1 The Perturbed Equations in Spherical Coordinates

Considering the spherical symmetrical case shown in Figure 3.2, it is appropriate to rewrite the perturbed equations in spherical coordinates. In this formulation, it is assumed that the acoustic wave generated by the jet source propagates from the surrounding air into the water–air mixture region without significant reflection at the interface of the water curtain, allowing the disturbance to be transmitted continuously across the boundary.

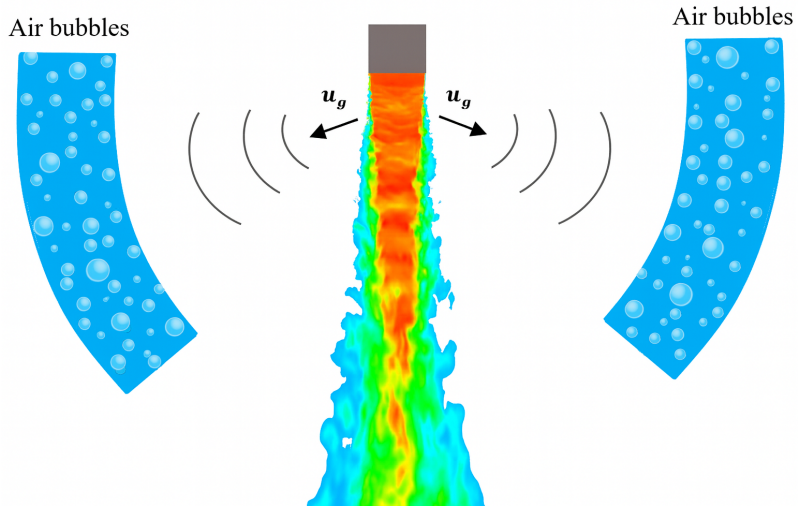

Figure 3.2 Spherical approximation to the flow outside of the jet for bubbly flow.

Within the mixture region, the perturbations are assumed to be predominantly radial, allowing all non-radial components to be neglected. Variations of the mean flow in space and time are considered small compared with those of the perturbations. Under these assumptions, the perturbation equations for the bubbles and liquid phases in the radial direction can be expressed as follows:

$$\begin{aligned}\frac{\partial}{\partial t}(\rho_g\phi_g' + \rho_g'\phi_g) + \frac{\partial}{\partial r}\left(\phi_g'\rho_g U_g + \rho_g' U_g\phi_g + \phi_g\rho_g u_g'\right) \\ + \frac{2}{r}\left(\phi_g'\rho_g U_g + \rho_g' U_g\phi_g + \phi_g\rho_g u_g'\right) = 0,\end{aligned} \tag{3.30}$$

$$\frac{\partial}{\partial t}(\rho_g\phi'_g + \rho'_g\phi_g) + \frac{\partial}{\partial r}\left(\phi'_g\rho_g U_g + \rho'_g U_g\phi_g + \phi_g\rho_g u'_g\right) + \frac{2}{r}\left(\phi'_g\rho_g U_g + \rho'_g U_g\phi_g + \phi_g\rho_g u'_g\right) = 0, \tag{3.31}$$

$$\frac{\partial}{\partial t}\left(\phi'_g\rho_g U_g + \rho'_g U_g\phi_g + \phi_g\rho_g u'_g\right) + \frac{\partial}{\partial r}\left(2U_g\rho_g\phi_g u'_g + U_g^2\rho_g\phi'_g + U_g^2\phi_g\rho'_g + \phi_g p'_g\right) + \frac{2}{r}\left(2U_g\rho_g\phi_g u'_g + U_g^2\rho_g\phi'_g + U_g^2\phi_g\rho'_g\right) - F'_{QS} = 0, \tag{3.32}$$

$$C_{pg}\left[\frac{\partial}{\partial t}\left[\rho'_g\phi_g T_g + \rho_g\phi'_g T_g + \rho_g\phi_g T'_g\right] + \frac{\partial}{\partial r}\left[\rho'_g\phi_g T_g U_g + \rho_g\phi'_g T_g U_g + \rho_g\phi_g T'_g U_g + \rho_g\phi_g T_g u'_g\right]\right] - \beta_g(\phi_g T_g + \phi'_g T_g + \phi_g T'_g)\left(\frac{\partial p'_g}{\partial t} + U_g\frac{\partial p'_g}{\partial r}\right) - Q'_{gf} = 0 \tag{3.33}$$

$$\frac{\partial}{\partial t}(\rho_f\phi'_f + \rho'_f\phi_f) + \frac{\partial}{\partial r}\left(\phi'_f\rho_f U_f + \rho'_f U_f\phi_f + \phi_f\rho_f u'_f\right) + \frac{2}{r}\left(\phi'_f\rho_f U_f + \rho'_f U_f\phi_f + \phi_f\rho_f u'_f\right) = 0, \tag{3.34}$$

$$\frac{\partial}{\partial t}\left(\phi'_f\rho_f U_f + \rho'_f U_f\phi_f + \phi_f\rho_f u'_f\right) + \frac{\partial}{\partial r}\left(2U_f\rho_f\phi_f u'_f + U_f^2\rho_f\phi'_f + U_f^2\phi_f\rho'_f + \phi_f p'_f\right) + \frac{2}{r}\left(2U_f\rho_f\phi_f u'_f + U_g^2\rho_f\phi'_f + U_g^2\phi_f\rho'_f\right) + F'_{QS} = 0, \tag{3.35}$$

$$C_{pf}\left[\frac{\partial}{\partial t}\left(\rho'_f\phi_f T_f + \rho_f\phi'_f T_f + \rho_f\phi_f T'_f\right) + \frac{\partial}{\partial r}\left(\rho'_f\phi_f T_f U_f + \rho_f\phi'_f T_f U_f + \rho_f\phi_f T'_f U_f + \rho_f\phi_f T_f u'_f\right)\right] - \beta_f(\phi_f T_f + \phi'_f T_f + \phi_f T'_f)\left(\frac{\partial p'_f}{\partial t} + U_f\frac{\partial p'_f}{\partial r}\right) + Q'_{gf} = 0 \tag{3.36}$$

Where the perturbation components of the coupling force and heat transfer are defined

below:

$$F'_{QS} = \frac{12\mu_f}{d_b^2}\Psi\left[(U_f - U_g)\phi'_g + (u'_f - u'_g)\phi_g\right] \tag{3.37}$$

$$Q'_{gf} = \frac{12\kappa_f}{d_b^2}\left[(T_f - T_g)\phi'_g + (T'_f - T'_g)\phi_g\right] \tag{3.38}$$

3.2.2 One-Dimensional Spherical Flow Simplifications

For the acoustic, the perturbation follows that of the acoustic radial propagation waves in the form:

$$(\tilde{u}, \tilde{\rho}, \tilde{p}, \tilde{T}) = (u', \rho', p', T')\,\frac{e^{ikr - i\omega t}}{r}. \tag{3.39}$$

Here, k is the complex wavenumber, ω is the angular frequency and r is the radial distance from the source. We assume $ikr \gg 1$, that implies that the wave propagates in the far-field regime where the radius r is large compared to the acoustic wavelength. In this region, the wave fronts are approximately planar, the amplitude decays smoothly and the oscillatory behavior becomes well defined. As the perturbations are assumed to be harmonic in time and space, the time and spatial derivatives $\frac{\partial}{\partial t}$ and $\frac{\partial}{\partial x}$ are replaced by —$i\omega$ and ik, respectively. Furthermore, pressure perturbations can be replaced by density perturbations using Equations 3.25 and 3.24, while the liquid volume fraction is expressed in terms of the gas volume fraction as ϕ_f=1 − ϕ_g. Under these simplifications, the continuity, momentum, thermal and density perturbation equations for the gas and liquid phases can be written as follows:

$$-i\omega\left[\rho'_g\phi_g + \rho_g\phi'_g\right] + ik\left(\rho_g\phi'_g U_g + \rho'_g\phi_g U_g + \rho_g\phi_g u'_g\right) = 0 \tag{3.40}$$

$$\begin{aligned} &-i\omega\left[\rho'_g\phi_g U_g + \rho_g\phi'_g U_g + \rho_g\phi_g u'_g\right] + ik\left[2\rho_g\phi_g U_g u'_g + \rho'_g\phi_g U_f^2 + \rho_f U_g^2\phi'_g\right] \\ &+ ik\phi_g(c_{Tg}^2\rho'_g + \frac{\rho_g c_{pg}}{\beta_g T_g}\frac{\gamma - 1}{\gamma}T'_g) - \frac{12\mu_f}{d_b^2}\Psi\left[(U_f - U_g)\phi'_g + (u'_f - u'_g)\phi_g\right] = 0 \end{aligned} \tag{3.41}$$

$$
\begin{aligned}
&C_{pg}\Big[-i\omega\big(\rho'_g\phi_g T_g+\rho_g\phi'_g T_g+\rho_g\phi_g T'_g\big)+\\
&ik\big(\rho'_g\phi_g T_g U_g+\rho_g\phi'_g T_g U_g+\rho_g\phi_g T'_g U_g+\rho_g\phi_g T_g u'_g\big)\Big]-\\
&\beta_g\phi_g T_g\Big(-i\omega\Big(c^2_{Tg}\rho'_g+\frac{\rho_g c_{pg}}{\beta_g T_g}\frac{\gamma-1}{\gamma}T'_g\Big)+ikU_g\Big(c^2_{Tg}\rho'_g+\frac{\rho_g c_{pg}}{\beta_g T_g}\frac{\gamma-1}{\gamma}T'_g\Big)\Big)-\\
&\frac{12\kappa_f}{d_b^2}\left[(T_f-T_g)\phi'_g+(T'_f-T'_g)\phi_g\right]=0
\end{aligned}
\tag{3.42}
$$

$$
-i\omega\left[\rho'_f(1-\phi_g)+\rho_f\phi'_g\right]+ik\left(\rho'_f(1-\phi_g)U_f-\rho_f\phi'_g U_f+\rho_f(1-\phi_g)u'_f\right)=0 \tag{3.43}
$$

$$
\begin{aligned}
&-i\omega\big[\rho'_f(1-\phi_g)U_f-\rho_f\phi'_g U_f+\rho_f(1-\phi_g)u'_f\big]\\
&+ik\big[2\rho_f(1-\phi_g)U_f u'_f+\rho'_f(1-\phi_g)U_f^2-\rho_f U_f^2\phi'_g\big]\\
&+ik(1-\phi_g)c^2_{Tf}\rho'_f+\frac{12\mu_f}{d_b^2}\Psi\left[(U_f-U_g)\phi'_g+(u'_f-u'_g)\phi_g\right]=0
\end{aligned}
\tag{3.44}
$$

$$
\begin{aligned}
&C_{pf}\Big[-i\omega\left(\rho'_f(1-\phi_g)T_f-\rho_f\phi'_g T_f+\rho_f(1-\phi_g)T'_f\right)+\\
&ik\left(\rho'_f(1-\phi_g)T_f U_f-\rho_f\phi'_g T_f U_f+\rho_f(1-\phi_g)T'_f U_f+\rho_f(1-\phi_g)T_f u'_f\right)\Big]\\
&-\beta_f(1-\phi_g)T_g\Big(-i\omega(c^2_{Tf}\rho'_f)+ikU_g(c^2_{Tf}\rho'_f)\Big)-\frac{12\kappa_f}{d_b^2}\left[(T_f-T_g)\phi'_g+(T'_f-T'_g)\phi_g\right]=0
\end{aligned}
\tag{3.45}
$$

$$
\begin{aligned}
&-c^2_{Tf}\rho'_f+\left(c^2_{Tg}-\frac{\rho_f D^2}{12\rho_g}\left[\omega^2+i\omega 2\beta_T\right]\right)\rho'_g\\
&+\frac{\gamma-1}{\gamma}\frac{C_{pg}}{T_g\beta_g}\left(\rho_g-\frac{\rho_f D^2}{12c^2_{Tg}}\left[\omega^2+i\omega 2\beta_T\right]\right)T'_g=0
\end{aligned}
\tag{3.46}
$$

3.3 Suspended bubbly case

For the suspended case, it is assumed that the mean flow velocity is zero of both phases are equal, therefore, under these assumptions, the perturbations equations reduces to:

$$
-i\omega\left[\rho'_g\phi_g+\rho_g\phi'_g\right]+ik\left(\rho_g\phi_g u'_g\right)=0 \tag{3.47}
$$

$$-i\omega\left[\rho_g\phi_g u'_g\right]+ik\phi_g(c^2_{Tg}\rho'_g+\frac{\rho_g c_{pg}}{\beta_g T_g}\frac{\gamma-1}{\gamma}T'_g)-\frac{12\mu_f}{d_b^2}\Psi\left[(u'_f-u'_g)\phi_g\right]=0 \tag{3.48}$$

$$\begin{aligned}C_{pg}\Big[-i\omega\big(\rho'_g\phi_g T_g+\rho_g\phi'_g T_g+\rho_g\phi_g T'_g\big)+ik\big(\rho_g\phi_g T_g u'_g\big)\Big]-\\ \beta_g\phi_g T_g\Big(-i\omega\Big(c^2_{Tg}\rho'_g+\frac{\rho_g c_{pg}}{\beta_g T_g}\frac{\gamma-1}{\gamma}T'_g\Big)\Big)-\\ \frac{12\kappa_g}{d_b^2}\left[(T_f-T_g)\phi'_g+(T'_f-T'_g)\phi_g\right]=0\end{aligned} \tag{3.49}$$

$$-i\omega\left[\rho'_f(1-\phi_g)-\rho_f\phi'_g\right]+ik\left(\rho_f(1-\phi_g)u'_f\right)=0 \tag{3.50}$$

$$-i\omega\left[\rho_f(1-\phi_g)u'_f\right]+ik(1-\phi_g)c^2_{Tf}\rho'_f+\frac{12\mu_f}{d_b^2}\Psi\left[(u'_f-u'_g)\phi_g\right]=0 \tag{3.51}$$

$$\begin{aligned}C_{pf}\Big[-i\omega\left(\rho'_f(1-\phi_g)T_f-\rho_f\phi'_g T_f+\rho_f(1-\phi_g)T'_f\right)+ik\left(+\rho_f(1-\phi_g)T_f u'_f\right)\Big]\\ -\beta_f(1-\phi_g)T_f\Big(-i\omega(c^2_{Tf}\rho'_f)\Big)+\frac{12\kappa_f}{d_b^2}\left[(T_f-T_g)\phi'_g+(T'_f-T'_g)\phi_g\right]=0\end{aligned} \tag{3.52}$$

$$\begin{aligned}-c^2_{Tf}\rho'_f+\left(c^2_{Tg}-\frac{\rho_f D^2}{12\rho_g}\left[\omega^2+i\omega 2\beta_T\right]\right)\rho'_g\\ +\frac{\gamma-1}{\gamma}\frac{C_{pg}}{T_g\beta_g}\left(\rho_g-\frac{\rho_f D^2}{12c^2_{Tg}}\left[\omega^2+i\omega 2\beta_T\right]\right)T'_g=0\end{aligned} \tag{3.53}$$

It is to note that direct numerical solution are presented here for the suspended case.

3.3.1 Effect of Volume of Fraction

The attenuation coefficient increases markedly with the gas content in the mixture. As ϕ_g rises, interphase interactions intensify, enhancing energy dissipation and thus the reduction effect. The maximum attenuation occurs near the bubble resonance, at $\frac{\omega}{\omega_0}\approx 1$, where the oscillations of the bubbles are most efficient in absorbing acoustic energy. The resonance

frequency ω_0 depends on the bubble diameter and the thermodynamic properties of the gas and liquid phases, expressed as:

$$\omega_0 = \sqrt{\frac{12\rho_g C_{Tg}^2 - \frac{4\sigma}{d_b}}{\rho_f d_b^2}} \tag{3.54}$$

Here, σ denotes the surface tension at the bubble interface.

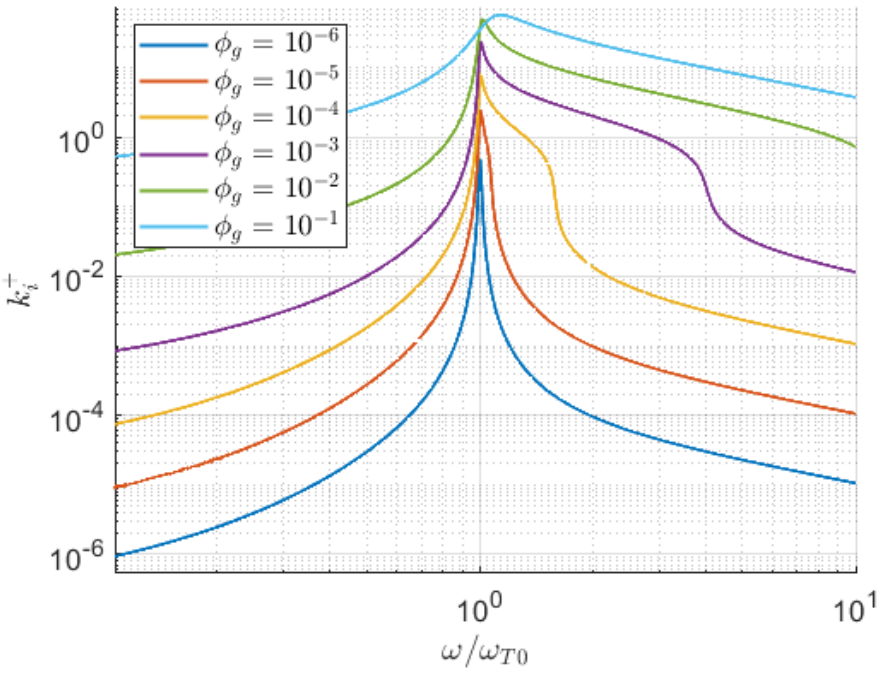

Figure 3.3 Reduction factor k_i^+ as a function of the dimensionless frequency for various gas volume of fraction ϕ_g. Here $d_b = 0.001m$.

3.3.2 Application of Suspended Bubbly Case to Jet Noise Reduction

In the present analysis, the background flow is assumed to originate from a turbulent jet discharging into a quiescent ambient medium, where the jet itself is the sole source of momentum. In the absence of external forces, the momentum flux across the jet cross-section is conserved downstream of the nozzle. For the suspended-particle configuration considered here, it is further assumed that the water–air curtain is located sufficiently far from the jet such that it remains unaffected by the ambient flow induced by the jet. Furthermore, the

acoustic wave generated by the jet source is considered to propagate from the surrounding air into the water–air mixture without significant reflection or distortion at the interface, enabling continuous transmission of the disturbance across the curtain boundary, without accounting for changes in the transmission medium from air to water.

3.3.3 Estimation of Sound Level Reduction for a Jet using Bubble Flow

Following the procedure presented in Equations 2.113-2.117, Figure 3.4 presents the normalized sound level reduction as a function of the gas volume fraction, ϕ_g, for different dimensionless bubble diameters. The results show that, for a fixed bubble size, the decibel reduction increases monotonically with increasing ϕ_g, indicating that stronger multiphase interactions enhance the overall attenuation. Among the cases studied, bubbles with $d_b/D_j \approx 0.04$ yield the highest sound reduction. This trend is consistent with the resonance diameter predicted by Equations 3.54 which for the present flow conditions is approximately 0.0381. These results confirm that an optimal bubble size exists that maximizes the noise attenuation for a given excitation frequency and jet condition.

3.3.4 Dependency on the Strouhal Number for the Suspended Bubbly Case

With

$$\frac{d_p}{D_j} = 3.8 \cdot 10^{-2}, \quad R_j = 10^5, \quad M_j = 1, \tag{3.55}$$

Figure 3.5 shows the normalized noise reduction as a function of the Strouhal number, St, for the parameters presented above. The results reveal a strong dependence of the attenuation on the excitation frequency. For all gas volume fractions, the sound reduction increases with St up to an optimal value where the maximum attenuation occurs. This behavior corresponds to the resonance condition between the excitation frequency and the natural frequency of the bubbles. Beyond this point, at higher Strouhal numbers, the attenuation decreases as the system moves away from resonance and the bubbles no longer respond effectively to the rapid acoustic oscillations. Increasing ϕ_g enhances the overall attenuation level and broadens the resonance peak, indicating stronger multiphase coupling and energy

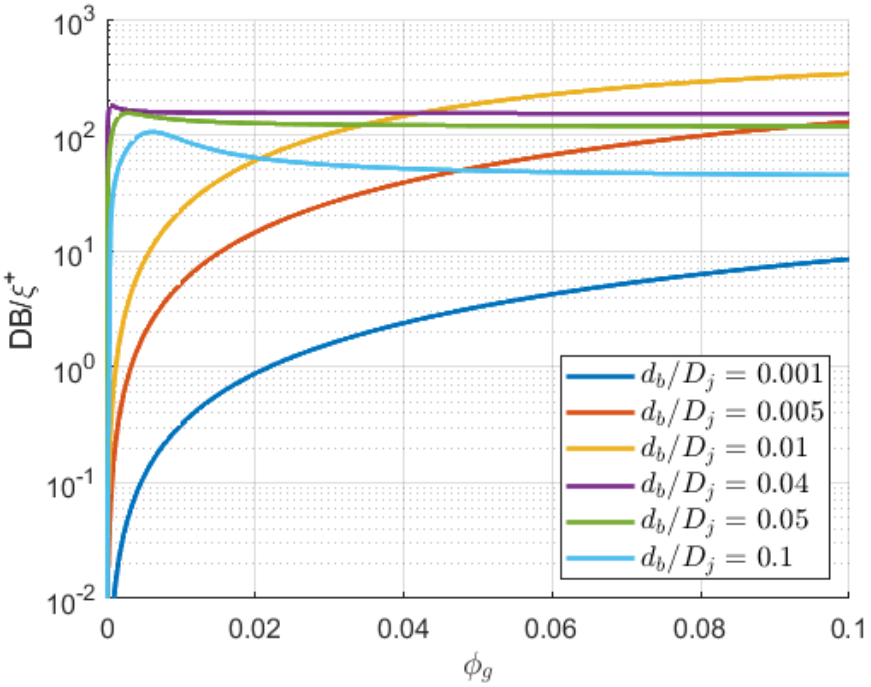

Figure 3.4 Normalized noise reduction as a function of the gas volume of fraction ϕ_g, where M_j =1, Reynolds number $R_j = 10^5$, and St=0.5 for the suspended bubbly case.

dissipation at higher gas volume fractions.

3.4 Comparison of Suspended Equations for Bubbly Flow with Experimental Results

Silberman [42] experimentally investigated the sound velocity and attenuation coefficients in air–water mixtures using a standing wave tube. Bubble sizes in the mixtures were controlled between about 0.08 and 0.26 in diameter for bubbles concentrations ranged from 0.003 to 1%. Figure 5 of Silberman's work, presented the experimental attenuation in db/cm.

To enable direct comparison between the numerical predictions and experimental data, the reduction factor obtained from the present suspended-bubbly formulation is converted into dimensional quantities. The dimensional complex wavenumber k is recovered as

$$k_i = k_i^+ \frac{\omega}{C_{Tf}}, \tag{3.56}$$

where C_{Tf} is the sound speed in the liquid and ω is the angular frequency of the acoustic

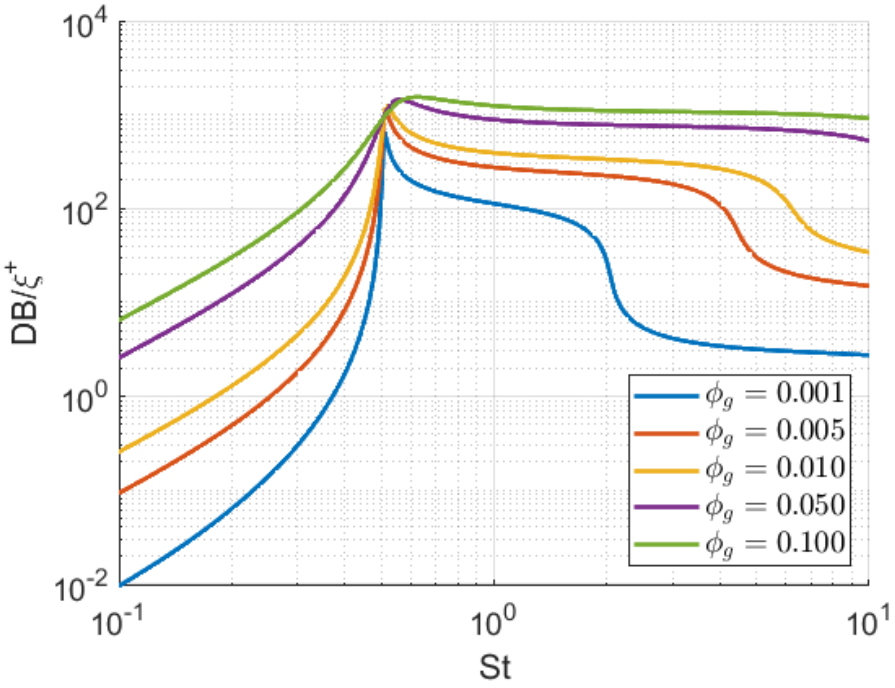

Figure 3.5 Dependency of the noise reduction on the Strouhal number for various ϕ_g, where M_j =1, Reynolds number $R_j = 10^5$, and $d_p = 0.038$m.

disturbance.The corresponding attenuation level in decibels per meter is obtained through

$$\frac{\mathrm{dB}}{\mathrm{m}} = 8.685\ k_i^+\ \frac{\omega}{C_{Tf}}, \tag{3.57}$$

where the constant $8.685 = 20 \log_{10} e$ converts the exponential decay into decibel units. For comparison with experimental data, results were expressed in dB/cm by dividing Equation 3.57 by 100. The frequency in Hz is obtained as $f = \frac{\omega}{2\pi}$.

The comparison in Figure 3.6 shows that the analytical model accurately captures both the magnitude and the frequency-dependent behavior of sound attenuation in the bubbly mixture. The attenuation increases with frequency, reaching a pronounced maximum near the resonance frequency of the bubbles, after which it decays.

3.5 Dispersed Bubbly Case

This section addresses the solution of the linearized perturbation equations for a flow in which the continuous phase exhibits a defined mean velocity. The analysis focuses on assess-

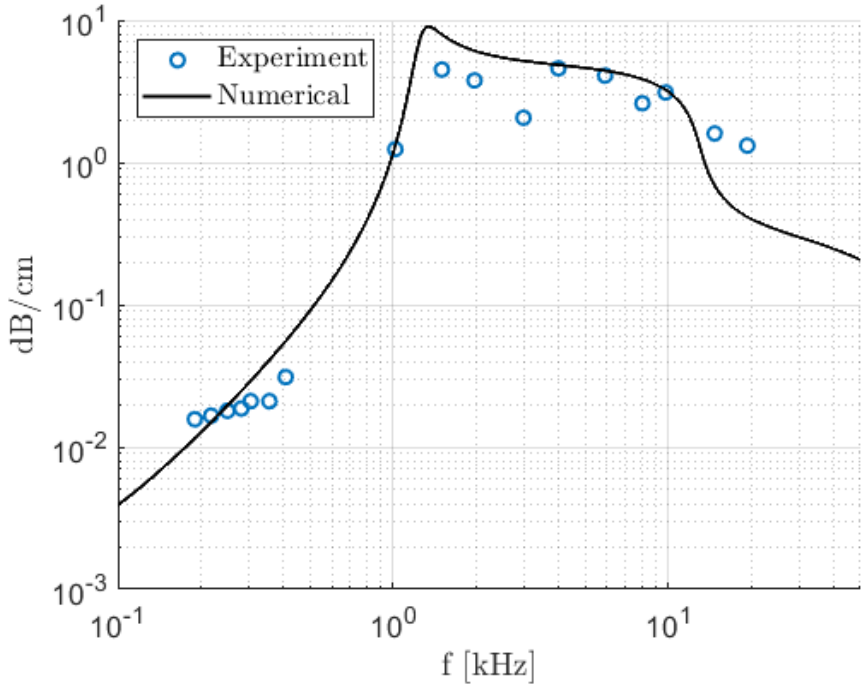

Figure 3.6 Comparison for the attenuation per centimeter between the numerical results and Silberman's Figure 5. Here, ϕ_g =0.01, d_b=0.528 cm.

ing the impact of mean flow and interphase slip on the acoustic attenuation mechanisms, contrasting these results with those obtained for the suspended configuration. The findings serve to clarify how convective transport and velocity coupling govern the attenuation behavior of air–bubble mixtures in water.

In the present analysis, the velocity of the water curtain at the boundary is taken as approximately 1 m/s. This value serves as an input for solving the perturbation equations under a prescribed liquid-phase motion. It should be noted, however, that in the actual physical configuration, the velocity of the water–air bubble mixture depends on the system geometry and on body forces such as gravity and buoyancy.

3.5.1 Mean Flow Equations for Bubbly Flow

This section focuses on determining the mean-flow components of the perturbation equations. These components are derived from the steady, non-perturbed, and thermally equilibrated form of the governing equations presented in Equations 3.30–3.36, under the assump-

tions of constant fluid-phase density and a pressure relationship given by the Laplace–Young equation. The resulting formulation reduces to a system of coupled ordinary differential equations in the radial coordinate, expressed as follows:

$$\frac{\partial(\rho_g \phi_g U_g)}{\partial r} + \frac{2\rho_g \phi_g U_g}{r} = 0, \tag{3.58}$$

$$\left[\frac{\partial(\rho_g \phi_g U_g U_g)}{\partial r} + \frac{2(\rho_g \phi_g U_g U_g)}{r}\right] + \phi_g \frac{\partial P_g}{\partial r} - \phi_g \frac{12\mu_f}{d_b^2}\Psi\,(U_g - U_p) = 0, \tag{3.59}$$

$$\frac{\partial(\phi_f U_f)}{\partial r} + \frac{2U_f \phi_f}{r} = 0, \tag{3.60}$$

$$\left[\frac{\partial(U_f U_f \phi_f)}{\partial r} + \frac{2(U_f U_f \phi_f)}{r}\right] + \frac{\phi_f}{\rho_f}\frac{\partial P_f}{\partial r} + (1-\phi_g)\frac{12\mu_f}{d_b^2}\Psi\,(U_g - U_p) = 0. \tag{3.61}$$

$$p_g - p_f = \frac{4\sigma}{r_b} \tag{3.62}$$

The boundary conditions at ($\xi = 0$) are: $U_f = 1\,\frac{m}{s}$, $U_g = 0\,\frac{m}{s}$, $\phi_g = 0.01$. These conditions represent a configuration in which the liquid phase has a prescribed velocity, and bubbles are released into the fluid.

Figure 3.7 presents the solution of the mean-flow equations for the liquid–bubbles mixture. As shown in Figure 3.7a, the mean velocity of the liquid phase (u_f) remains nearly constant along the radial coordinate, while the gas phase (u_g) exhibits only a slight deviation from it. This behavior is expected because of the low inertia of the air bubbles, which respond rapidly to the motion of the surrounding liquid, leading to negligible slip between phases as the flow moves forward in the radial coordinate.

Figure 3.7b displays the corresponding mean volume fractions. At the boundary,ϕ_g=0.01,

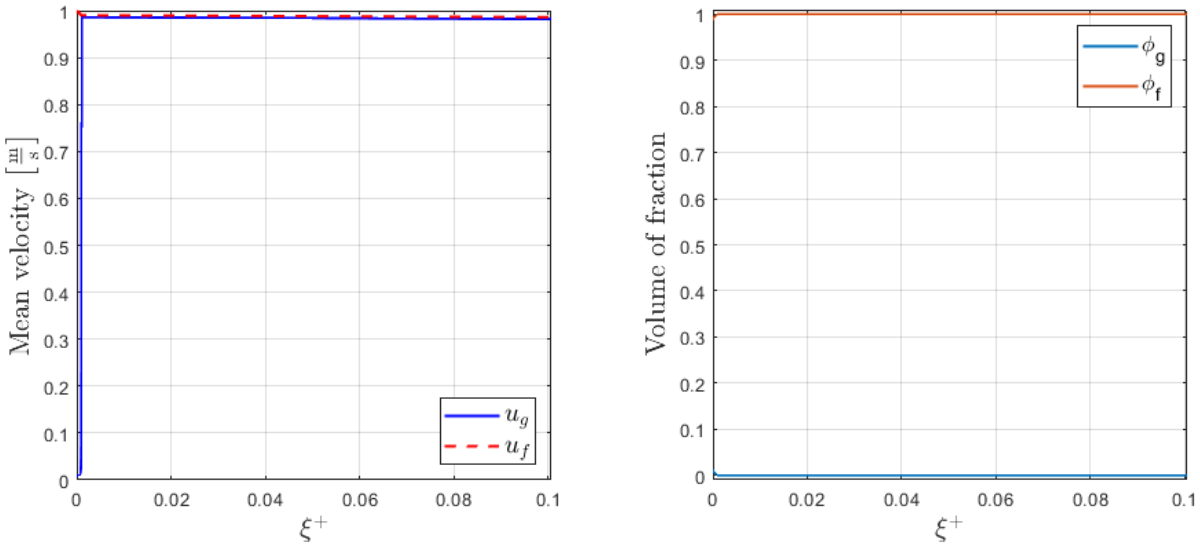

(a) Mean velocity

(b) Mean volume fraction

Figure 3.7 Numerical solution of the mean flow system: (a) Mean flow velocities and (b) Mean volume fraction.

while the liquid fraction satisfies the relation $\phi_f = 1 - \phi_g$. As the flow evolves radially, ϕ_g gradually decreases to approximately 0.005, indicating a mild redistribution of bubbles within the liquid phase.

3.5.2 Effect of Interphase Relative Motion on Acoustic Wave Attenuation for Bubbly Flow

The influence of the slip velocity on k_i^+ is examined at two radial positions. The first location corresponds to the location in which the air bubbles are injected in the liquid flow and the relative velocity between the bubbles and liquid phase is largest. The second location corresponds to a downstream position where both phases have reached dynamic equilibrium. These two locations are selected to assess how interphase velocity slip influences the attenuation behavior, in comparison with the suspended case at the same volume fraction.

As shown in Figure 3.8, introducing slip between the bubbles and liquid phase reduces the attenuation coefficient k_i^+ for sub-resonant frequencies ($\omega/\omega_0 < 1$), indicating weaker energy dissipation in this regime. This behavior could be attribute to the velocity difference between the phases that partially decouples their motion, decreasing the effective drag and thermal

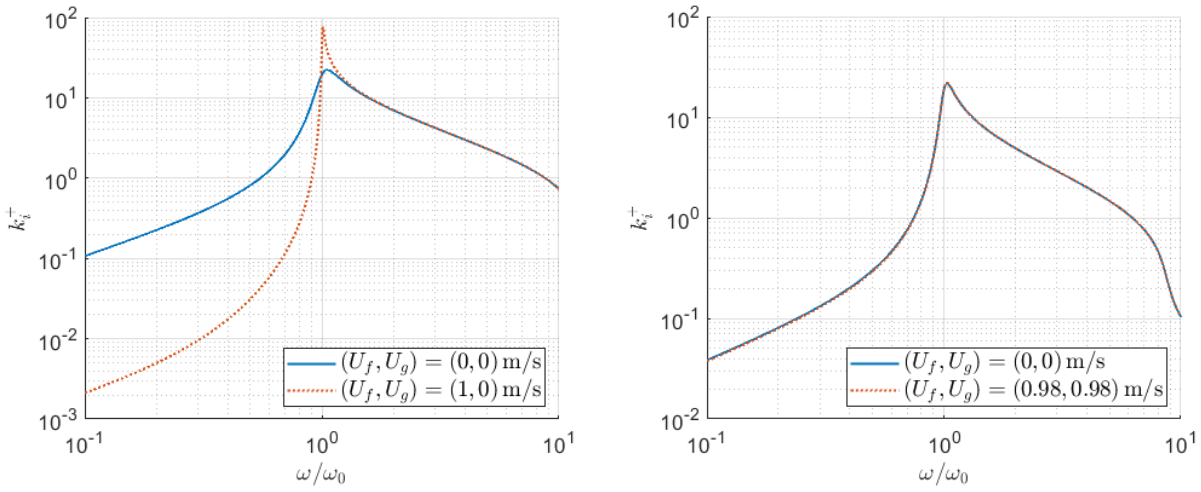

Figure 3.8 Effect of Ω on k_i^+ with phase motion for bubbly flow. a)with phase slip and b)without phase slip. Here, $d_b = 0.005m$.

coupling responsible for damping. At the resonance frequency ($\omega/\omega_0 \approx 1$), the presence of slip between the phases increases k_i^+ because it alters the dynamic response of the bubbles to the acoustic pressure fluctuations. The relative motion introduces a phase lag between the gas and liquid oscillations, which modifies the efficiency of the energy exchange between phases and enhances the pressure velocity hysteresis within the bubble, and, as a result a larger portion of the acoustic energy is dissipated during each oscillation cycle, leading to a more pronounced attenuation peak compared to the no-slip condition.

For the dispersed case the dependency of the noise reduction on the Strouhal Number follows the same trend as the suspended case, however, as can be seen in the Figure 2.30, at low Strouhal numbers ($St < 0.5$), the case with mean flow exhibits a noticeable reduction in attenuation compared to the suspended condition. This behavior results from the convective transport of the acoustic perturbations, which weakens the effective coupling between the gas and liquid phases. Near the resonant region, the presence of mean flow amplifies the resonance peak, indicating that relative motion enhances the dynamic response of the bubbles to acoustic excitation at the resonance frequency. At higher frequencies there is no difference between the both cases.

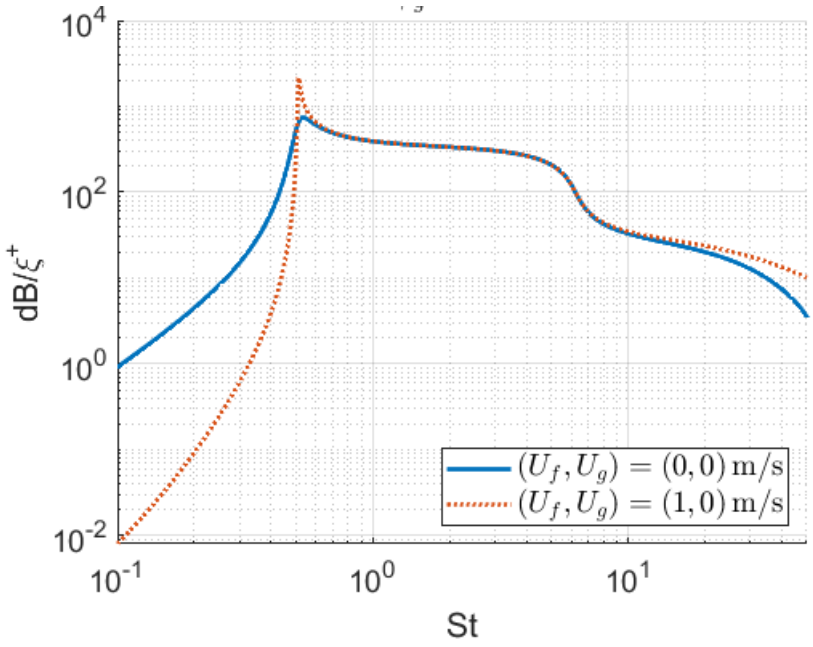

Figure 3.9 Dependency of the noise reduction on the Strouhal number with relative motion between the phases.

These effects highlight the importance of convective coupling in predicting the acoustic behavior of bubbly mixtures under more realistic flow conditions.

3.5.3 Solution of the Perturbation Equations for Bubbly Flow as a Function of the Mean Flow Results

Here the perturbation equations are solved for k_i^+ as a function of ξ using the radial mean flow obtained in Section 3.5.1. Then, following Equation 2.117 with $M_j = 1$ and St $= 0.5$, the effect of the bubble diameter on the normalized noise reduction DB/ξ^+ is evaluated. The results presented in Figure 2.31 reveal the existence of an optimal bubble diameter of about 0.04 of the jet diameter.

Figure 3.10 presents the normalized noise reduction (dB/ξ^+) as a function of the normalized radial distance for different bubble diameter ratios d_b/D_j. The results indicate that the attenuation per unit distance remains nearly constant throughout the mixture. This behavior arises because the solution depends on the mean-flow field, in which the gas-phase volume fraction varies sharply only near the boundary and remains almost uniform across the rest of the domain, as shown in Figure 3.7b. Since the acoustic attenuation is primarily

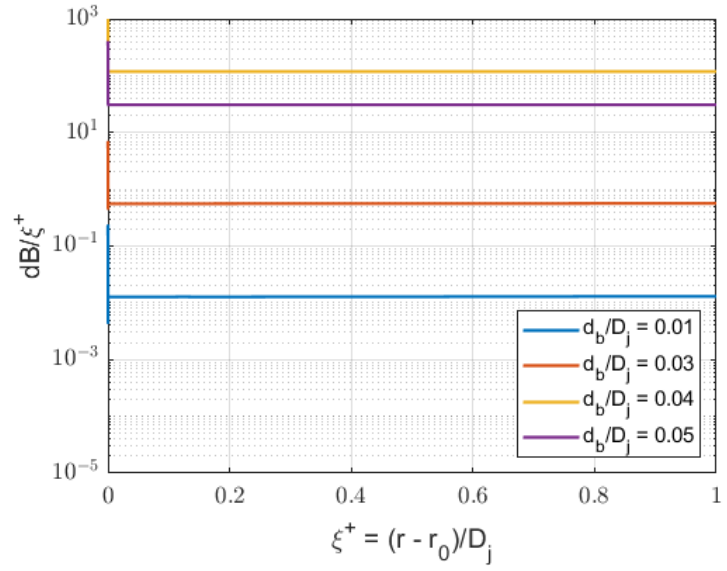

(a)

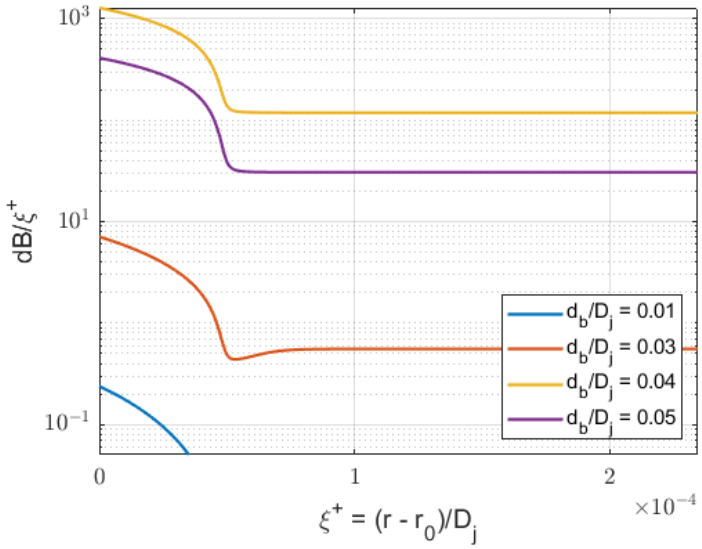

(b)

Figure 3.10 Effect of droplet diameter on the normalized noise reduction. DB/ξ^+ as a function of the mean floe solution. a) complete domain b) Close-up view of the region near the boundary.

governed by the gas (bubbles) volume fraction, its near-uniform distribution leads to an approximately constant attenuation rate. A close-up view of the region near the boundary, Figure 3.10b, reveals a localized peak in attenuation, corresponding to the rapid variation of the mean-flow quantities where the gas volume fraction is highest. Beyond this narrow

region, the attenuation stabilizes as the mean-flow variables reach equilibrium. These results confirm that the spatial variation of acoustic attenuation is closely linked to the behavior of the mean-flow parameters, particularly the local gas-phase volume fraction.

A comparison with respect the suspended case is not included here because, as the mean-flow solution shows, see Figure 3.7a, the velocity of the bubbles rapidly approaches that of the surrounding liquid, resulting in negligible slip throughout the domain. Consequently, the noise reduction for the present configuration is nearly identical to that of the suspended case, as can be observed in Figure 3.9, where both curves overlap when the slip velocity approaches zero.

4 Conclusion and future work

This study investigated the potential of an air–water multiphase curtain surrounding an aircraft engine as a passive technique for jet noise reduction. Two distinct configurations were analyzed: (i) a gaseous medium (air) containing liquid water droplets, and (ii) a liquid medium (water) containing air bubbles. For each configuration, two flow regimes were examined: (a) a suspended case, where both phases exhibits negligible mean velocity, and (b) a dispersed case, in which the ambient velocity is significant enough to induce a velocity in the mixture.

The results reveal that four parameters predominantly govern the acoustic attenuation in such multiphase mixtures: the particulate phase diameter, the volume fraction, the slip velocity between phases, and the Strouhal number characterizing the acoustic excitation. The analysis demonstrates that optimizing these parameters enables effective manipulation of the coupling between the acoustic wave and the particulate phase dynamics, thereby enhancing the attenuation performance.

The main conclusions for both configurations are summarized below:

4.1 Particle Suspended Case

We conducted both numerical and an analytical (asymptotic) solutions. The analytical solution agreed with the numerical solution at volume of fraction ratios close to 0.1. This helped us validate the numerical solution. Furthermore, numerical results for the suspended case showed good agreement with both available experimental data and CFD simulations, not only in magnitude but also in the trends, reinforcing the validity of the present formulation and numerical methodology.

The results reveal that four parameters predominantly govern the acoustic attenuation in such multiphase mixtures: the particulate size, the volume fraction, the slip velocity between phases, and the Strouhal number characterizing the acoustic excitation. Optimizing these parameters enables effective manipulation of the coupling between the acoustic wave and the particulate dynamics, thereby enhancing the attenuation performance.

The numerical solution was then used to conduct parametric studies, which showed that:

1. The acoustic attenuation increases with the particles volume of fraction. The more water droplets, the more it absorbs the acoustic energy, this indicate that a higher concentration of droplets enhances momentum and thermal coupling between phases.

2. An optimal droplet-to-jet diameter ratio, dp/Dj$\approx 0.0001 - 0.0004$ maximizes attenuation corresponding to a peak in noise reduction at a Strouhal number of $St = 0.5$. Droplets smaller than this range act as tracers with negligible damping, while larger droplets possess excessive inertia, reducing their acoustic response.

3. Noise reduction rises with the Strouhal number St but gradually saturates as St increases, indicating a limit to frequency-driven enhancement of attenuation.

4.2 Particle Dispersed case

1. Interphase slip shifts the attenuation peak to higher non dimensional frequencies and lowers its magnitude relative to the suspended case for the same volume of fraction ratio.

2. the presence of relative motion increases the noise reduction with respect to the suspended case for the same value of volume of fraction as a function of the Strouhal Number.

3. When both phases move at low similar velocities, the attenuation effect is similar to that of the suspended case for the same volume of fraction ratio,confirming that interphase slip modify the reduction mechanisms.

4. Most attenuation occurs within one jet diameter from the mixture front $\xi^+ \leq 1$. Beyond this point, the attenuation rate stabilizes to an approximately constant value. This behavior is attributed to the higher particle volume fraction near the injection boundary. Consequently, a curtain thickness on the order of one jet nozzle diameter is sufficient to capture most of the attenuation effects.

5. The optimum droplet size for the flow parameters define for the dispersed case is about 0.0004 of the jet nozzle diameter.

4.3 Bubbly Suspended Case

Numerical solutions were obtained for the acoustic attenuation in a water medium containing air bubbles. The results were validated against the experimental measurements reported by Silberman [42], showing a good agreement across the frequency range studied. This comparison confirms the accuracy of the present formulation in capturing the attenuation characteristics of bubbly liquids. The validated model was subsequently employed to perform a parametric study, which revealed that:

1. Acoustic attenuation increases with the gas volume fraction. A higher concentration of bubbles enhances the exchange of momentum and thermal energy between the phases. The dominant attenuation mechanism is governed by the resonance of the bubbles, which strongly amplifies the energy transfer between the acoustic field and the mixture.

2. An optimal bubble-to-jet diameter ratio of approximately $d_b/D_j = 0.038$ maximizes attenuation corresponding to a peak in noise reduction at a Strouhal number of $St = 0.5$. This ratio corresponds to the resonance condition, where the natural frequency of the bubbles matches the acoustic excitation frequency.

3. The sound attenuation increases with the Strouhal number up to an optimal value, beyond which it decreases as the system departs from resonance. Increasing the gas volume fraction not only elevates the overall attenuation level but also broadens the resonance peak.

4.4 Bubbly Dispersed Case

1. introducing slip between the bubbles and liquid phase reduces the attenuation for subresonant frequencies. However, At the resonance frequency, the attenuation increase.

2. When both phases move at low similar velocities, the attenuation effect is similar to that of the suspended case for the same gas volume of fraction,confirming that interphase slip modify the reduction mechanisms.

3. When interphase slip is present, the dependence of noise reduction on the Strouhal number follows the same overall trend as in the suspended case. However, at low Strouhal numbers, attenuation is noticeably reduced compared to the no-slip condition. Near the resonant region, the presence of mean flow amplifies the resonance peak, while at higher frequencies, attenuation exhibits a slight secondary increase.

4. TThe optimal droplet size for the flow parameters defined in the dispersed case is approximately 0.04 of the jet nozzle diameter. Furthermore, if the gas volume fraction remains uniform across the mixture, the noise level remains nearly unchanged, indicating that the dominant governing parameter in noise reduction is the volume fraction.

4.5 Future Work

While the results of this work demonstrated the feasibility of this passive mitigation concept, several extensions are required to achieve a complete understanding of the coupled aeroacoustic–multiphase phenomena.

Future work will focus on performing Large Eddy Simulations (LES) using OpenFOAM to directly resolve the jet flow field, its radiated acoustic field, and their interaction with the surrounding air–water curtain. The LES framework will allow investigation of the spatial distribution of attenuation, phase interference effects, and broadband noise reduction in realistic geometries representative of jet exhausts.

Complementary experimental measurements are also planned to validate the numerical and analytical predictions. The experiments will employ an instrumented jet facility with a controlled air–water curtain system, enabling direct observation of the far-field sound pressure levels under varying droplet and bubble distributions. Measurements will quantify

the dependence of noise attenuation on particle size, concentration, and curtain thickness.

Together, these computational and experimental efforts will extend the current understanding from idealized one-dimensional propagation models to fully coupled three-dimensional, unsteady jet–curtain interactions. The ultimate objective is to define optimized multiphase configurations capable of achieving broadband jet-noise reduction suitable for practical implementation in aerospace and propulsion systems.

REFERENCES

[1] Lee, J., et al., "Military Aviation and the Environment: Historical Trends and Comparison to Civil Aviation," *J. Aircraft*, 2005. https://doi.org/10.2514/1.6888.

[2] Raef, T., Khalil, M. K., and Elzahaby, A., "Enhancement of Propulsion Performance through Jet Noise Reduction Technologies: A Review," *Conference Paper*, 2014.

[3] Brown, G. L., and Roshko, A., "On Density Effects and Large Structures in Turbulent Mixing Layers," *J. Fluid Mech.*, Vol. 64, No. 4, 1974, pp. 775–816. https://doi.org/10.1017/S002211207400190X.

[4] Tam, C. K. W., "New Noise Component of Supersonic Jets: Laboratory Jets to High-Performance Aircraft," *AIAA J.*, Vol. 63, No. 9, 2025, pp. 3752–3762. https://doi.org/10.2514/1.J064769.

[5] Norum, T. D., "Reductions in multi-component jet noise by water injection," *Tenth AIAA/CEAS Aeroacoustics Conference*, Manchester, United Kingdom, 2004. https://doi.org/10.2514/6.2004-2976, aIAA Paper 2004-2976.

[6] Salehian, S., and Mankbadi, R. R., "Simulations of rocket launch noise suppression with water injection from impingement pad," *Int. J. Aeroacoustics*, Vol. 19, No. 3–5, 2020, pp. 207–239. https://doi.org/10.1177/1475472X20930653.

[7] Mahanta, P. K., Vajpayee, S., and Sadek, M. M., "Suspended water droplets as a means of noise reduction," *Appl. Acoust.*, Vol. 19, No. 2, 1986, pp. 77–90.

[8] Basner, M., Clark, C., Hansell, A., Hileman, J. I., Janssen, S., Shepherd, K., and Sparrow, V., "Aviation Noise Impacts: State of the Science," *Noise Health*, Vol. 19, No. 87, 2017, pp. 41–50. https://doi.org/10.4103/nah.NAH_104_16.

[9] Lighthill, M. J., "On sound generated aerodynamically. I. General theory," *Proc. R. Soc. Lond. A*, Vol. 211, No. 1107, 1952, pp. 564–587. https://doi.org/10.1098/rspa.1952.0060.

[10] Williams, J. E. F., "The noise from turbulence convected at high speed," *Philos. Trans. R. Soc. Lond. A*, Vol. 255, No. 1061, 1963, pp. 469–503. https://doi.org/10.1098/rsta.1963.0010.

[11] Crow, S. C., and Champagne, F. H., "Orderly structure in jet turbulence," *J. Fluid Mech.*, Vol. 48, No. 3, 1971, pp. 547–591. https://doi.org/10.1017/S0022112071002259.

[12] Yule, A. J., "Large Scale Structure in the Mixing Layer of a Round Jet," *J. Fluid Mech.*, Vol. 89, No. 3, 1978, pp. 413–432. https://doi.org/10.1017/S0022112078002670.

[13] Papamoschou, D., and Roshko, A., "The Compressible Turbulent Shear Layer: An Experimental Study," *J. Fluid Mech.*, Vol. 197, 1988, pp. 453–477. https://doi.org/10.1017/S0022112088003325.

[14] Elliott, G. S., and Samimy, M., "Compressibility Effects in Free Shear Layers," *Phys. Fluids*, Vol. 2, No. 7, 1990, pp. 1231–1240. https://doi.org/10.1063/1.857816.

[15] Samimy, M., and Elliott, G. S., "Effects of Compressibility on the Characteristics of Free Shear Layers," *AIAA J.*, Vol. 28, No. 3, 1990, pp. 439–445. https://doi.org/10.2514/3.10412.

[16] Clemens, N. T., and Mungal, M. G., "Large-Scale Structure and Entrainment in the Supersonic Mixing Layer," *J. Fluid Mech.*, Vol. 284, 1995, pp. 171–216. https://doi.org/10.1017/S0022112095000310.

[17] Thurow, B., Samimy, M., and Lempert, W., "Compressibility Effects on Turbulence Structures of Axisymmetric Mixing Layers," *Phys. Fluids*, Vol. 15, No. 6, 2003, pp. 1755–1765. https://doi.org/10.1063/1.1570829.

[18] Tam, C. K. W., Viswanathan, K., Ahuja, K. K., and Panda, J., "The sources of jet noise: experimental evidence," *J. Fluid Mech.*, Vol. 615, 2008, pp. 253–292. https://doi.org/10.1017/S0022112008003704.

[19] Mankbadi, R., and Liu, J. T. C., "Sound Generated Aerodynamically Revisited: Large-Scale Structures in a Turbulent Jet as a Source of Sound," *Philos. Trans. R. Soc. Lond. A*, Vol. 311, No. 1516, 1984, pp. 183–217. https://doi.org/10.1098/rsta.1984.0080, URL http://www.jstor.org/stable/37454.

[20] Powell, A., "The Noise of Choked Jets," *J. Acoust. Soc. Am.*, Vol. 25, 1953, pp. 385–389. https://doi.org/10.1121/1.1907052.

[21] Martlew, D. L., "Noise Associated with Shock Waves in Supersonic Jets," *AGARD Conference Proceedings 42*, AGARD, 1969, pp. 7–1–7–10.

[22] Harper-Bourne, M., and Fisher, M. J., "The Noise from Shock Waves in Supersonic Jets," *Proceedings of the AGARD Conference on Noise Mechanisms*, AGARD, 1973, pp. 11–1–11–13.

[23] Engblom, W. A., Khavaran, A., and Bridges, J., "Numerical Prediction of Chevron Nozzle Noise Reduction using WIND-MGBK Methodology," *10th AIAA/CEAS Aeroacoustics Conference*, Manchester, United Kingdom, 2004. https://doi.org/10.2514/6.2004-2979.

[24] Kurbjun, M. C., "Limited Investigation of Noise Suppression by Injection of Water into Exhaust of Afterburning Jet Engine," Tech. Rep. NACA RM L57L05, National Advisory Committee for Aeronautics (NACA), Langley Aeronautical Laboratory, Langley Field, VA, Feb. 1958. Research Memorandum, February 20, 1958.

[25] Zoppellari, E., and Juvé, D., "Reduction of Jet Noise by Water Injection," *3rd AIAA/CEAS Aeroacoustics Conference*, Atlanta, GA, USA, 1997. AIAA Paper 97-1622.

[26] Henderson, B., "Fifty years of fluidic injection for jet noise reduction," *Int. J. Aeroacoustics*, Vol. 9, No. 1, 2010, pp. 91–122. https://doi.org/10.1260/1475-472X.9.1-2.91.

[27] Mankbadi, R. R., "Dynamics and Control of Coherent Structures in Turbulent Jets," *Appl. Mech. Rev.*, Vol. 45, No. 6, 1992, pp. 219–248. https://doi.org/10.1115/1.3119761.

[28] Mankbadi, M. R., and Balachandar, S., "Multiphase effects on spherical Rayleigh–Taylor interfacial instability," *Phys. Fluids*, Vol. 26, 2014, p. 023301. https://doi.org/10.1063/1.4863447.

[29] Dobbins, R. A., and Temkin, S., "Propagation of sound in a gas-particle mixture and acoustic combustion instability," *AIAA J.*, Vol. 5, No. 11, 1967, pp. 2182–2186.

[30] Cole, J. E., and Dobbins, R. A., "Measurements of the attenuation of sound by a warm air fog," *J. Atmos. Sci.*, Vol. 28, 1971, pp. 202–209.

[31] Kandula, M., "Dispersion of sound in dilute suspensions with nonlinear particle relaxation," *J. Acoust. Soc. Am.*, Vol. 127, No. 3, 2010, pp. EL115–EL120. https://doi.org/10.1121/1.3299172.

[32] Kandula, M., "Sound propagation in saturated gas-vapor-droplet suspensions with droplet evaporation and nonlinear relaxation," *J. Acoust. Soc. Am.*, Vol. 131, 2012, pp. EL434–EL440. https://doi.org/10.1121/1.4710835.

[33] Herrero, I., Picó, R., Sánchez, V., García, L. M., et al., "Experimental study of sound attenuation by layers of water droplets," *EuroNoise 2015*, Maastricht, Netherlands, 2015.

[34] Crowe, C. T., Schwarzkopf, J. D., Sommerfeld, M., and Tsuji, Y., *Multiphase Flows with Droplets and Particles*, 2nd ed., CRC Press, 2012.

[35] Schiller, L., and Naumann, Z., "A drag coefficient correlation," *VDI Z.*, Vol. 77, 1935, pp. 318–320.

[36] Sommerfeld, M., "Numerical methods for dispersed multiphase flows," *Particles in*

Flows, Springer International Publishing, Cham, 2017, pp. 326–396. https://doi.org/10.1007/978-3-319-60282-0_6.

[37] Sullivan-Silva, K. B., "Underwater Acoustic Scattering from Spherical Particulates and Bubbles," Tech. Rep. NUSC Technical Report 6772, Naval Underwater Systems Center, Newport, Rhode Island / New London, Connecticut, Nov. 1989. Approved for public release; distribution unlimited.

[38] Bohne, T., Grießmann, T., and Rolfes, R., "Modeling the noise mitigation of a bubble curtain," *J. Acoust. Soc. Am.*, Vol. 146, 2019, pp. 2212–2223. https://doi.org/10.1121/1.5126698.

[39] Cole, J. E., and Dobbins, R. A., "Propagation of Sound Through Atmospheric Fog." *Journal of the Atmospheric Sciences.*, Vol. 27, 1970, pp. 426–437. https://doi.org/10.1175/1520-0469(1970)027⟨0426:POSTAF⟩2.0.CO;2.

[40] Temkin, S., *Suspension Acoustics: An Introduction to the Physics of Suspensions*, Cambridge University Press, 2005.

[41] Kazarina, M. V., "A Volume-Force Synthetic Disturbance Approach for High-Fidelity Modeling of Unsteady Fluid-Structure Interactions," Phd.dissertation, Embry-Riddle Aeronautical University, Daytona Beach, Florida, 2019.

[42] Silberman, E., "Sound velocity and attenuation in bubbly mixtures measured in standing wave tubes," *J. Acoust. Soc. Am.*, Vol. 29, 1957, pp. 925–933. https://doi.org/10.1121/1.1909095.